On the Influence of the Through-Thickness Strain Gradients for Characterization of Formability and Fracture of Sheet Metal Alloys

By

Dong-Won Kenneth Cheong

A thesis

presented to the University Of Waterloo

in fulfillment of the

thesis requirement for the degree of

Master of Applied Science

in

Mechanical and Mechatronics Engineering

Waterloo, Ontario, Canada, 2019

Author's Declaration

I hereby declare that I am the sole author of this thesis. This is a true copy of the thesis, including any required final revisions, as accepted by my examiners.

I understand that my thesis may be made electronically available to the public.

Abstract

The main focus of this thesis is to investigate the effect of through-thickness strain gradient on sheet metal formability. Current technology for formability analysis has relied upon deformation modes of in-plane stretching in which localized necking and unstable strain localization become the dominant failure mode. The formability of sheet metal is often explained with a forming limit diagram (FLD) that the onset of necking indicates the upper end of the formable range. However, it is practically known in the industry that a material can often be formed beyond the conventional forming limits under out-of-plane deformation. The through-thickness strain gradient generated by out-of-plane deformation suppresses the onset of necking and thus improves formability. In this thesis, novel out-of-plane formability tests were designed and performed to investigate the correlation between the severity of bend and material formability. Three deformation modes considered in the research: a pure bending under plane strain, equi-biaxial stretching with severe bending, and a combination of stretching and bending.

These formability tests have been specially designed to employ Digital Image Correlation (DIC) to obtain full-field strain measurements until fracture. The advent of DIC has revolutionized the field of experimental mechanics and allows for a better understanding and quantification of fracture strains compared to indirectly inferring them from inverse finite-element simulations based upon a measured displacement to the failure of the test sample.

Various automotive sheet metal alloys are considered in this thesis. However, the focus materials of interest were advanced high strength steels such as DP980, and an aluminum alloy, AA5182, since they have distinct mechanical properties in aspects of strength, ductility, and hardening behavior.

In the field of formability, the VDA238-100 bend test introduced in 2010 has rapidly gained acceptance since it has reliable and intuitive test parameters for bendability analysis. In contrast to the most of traditional formability tests in which in-plane stretching is the dominant failure mode, the VDA bend is

designed to investigate material response under the pure bending condition in which the most severe through-thickness strain gradient is expected. The result is reported in terms of bend angle which is a direct and straightforward representative of bendability. However, the relatively simple setup of VDA bend test provides a fundamental limitation as the test data is restricted to the load and punch displacement only. Therefore, a novel bend test apparatus based on VDA 238-100 specification was developed at UW as a part of this thesis to introduce best practices of bendability analysis with the addition of DIC. A wide range of metals such as AHSS, aluminum alloys, and magnesium were considered in this research to investigate plane strain bending behavior. The results indicated that the presence of through-thickness strain gradient effectively suppresses necking, thus a remarkable improvement in formability was observed.

The concept of imposing through-thickness strain gradients was also applied to the equi-biaxial stretching condition. Based on Nakazima tests that standardized in ISO12004-2 (2008), scaled-down hemispherical punches were manufactured with the intention of increasing the bend severity by reducing the bend radius. The influence of through-thickness strain gradient on equi-biaxial fracture limit was analyzed with the experimental data and DIC measurement. It was reported that there is a strong positive correlation between the bend severity and material formability. Moreover, it was observed that the mitigation of necking significantly affects the strain development and with the high bend severity, proportional loading conditions were maintained until fracture.

It was reported from the Nakazima test and VDA bend test that there is a significant disagreement between the material responses under in-plane stretching and out-of-plane bending. To provide a bridge between these stress-states, a stretch-bend toolset was designed to investigate the combined effect of stretching and bending. A time-dependent methodology was employed to detect the limit strains based on an acceleration of the local strain rate in the necking area. The ratio between stretching and bending was controlled by adjusting the punch radius to investigate the correlation between the limit strain and the bend severity. The positive influence of the through-thickness strain gradient on forming limit was

reported. The result was observed to be within the range between the VDA bend test and Nakazima test as this test is intended to investigate the combined effect of bending and stretching.

The characterization tests developed in this thesis were developed to obtain linear strain paths until fracture with an emphasis upon plane strain tension which is the critical strain path for sheet metals. The proportional loading condition and linearization of strain paths were observed from the equi-biaxial application which resulted in a remarkable improvement in the fracture limit compared to more traditional tests that involved necking which changes the strain path and is difficult to resolve using DIC for fracture characterization. These fracture limit results provided an insight into the "upper bound" for formability as a positive influence of through-thickness strain gradient was commonly observed. The stretch-bend tests verified that the forming range can be expanded from a traditional FLC to the out-of-plane fracture limit depending on how much bending was involved in the process.

During the research, the Nakazima test was performed to provide a conservative forming limit under in-plane stretching. Moreover, the hole expansion test which corresponds to uniaxial loading was employed to complete the draw side of the fracture limit curve. Based on the data collected from in-plane and out-of-plane deformation tests, a new forming limit diagram with the out-of-plane fracture limit curve was introduced to describe material formability in consideration of the effect of bending.

Acknowledgements

First, I would like to express my deepest gratitude to my supervisor, Prof. Clifford Butcher, for giving me a great opportunity to work on this research. Without your instruction, the completion of this study could not have been possible. Thank you for your patience, encouragement, and sharing your enthusiasm with me. I have learned a lot under your supervision.

I would also like to express my very great appreciation to Prof. Worswick for giving me the opportunity to share my research with a great team of researchers. Thank you sincerely for providing valuable research resources and feedback during my thesis.

I would also like to thank Dr. Armin Abedini, Sante DiCecco, Jacqueline Noder, and Kaab Omer for all your help and instructions throughout the research. Valuable discussions with you all were always the key of my research breakthroughs.

I also like to gratefully appreciate technical help from Eckhard Budziarek, Andy Barber, Neil Griffett, Jeff Wemp, and Tom Gawel.

Finally, my expression of appreciation also goes to the support of our sponsors: Honda R&D Americas Inc. and the Steel Marketing Development Institute (SMDI). Especially, I like to thank Jim Dykeman from Honda R&D for sharing his insight on AHSS and the need to characterize sheet materials in tight radius bending that became central to my thesis.

Table of Contents

List of Figures

List of Tables

List of Abbreviations

AHSS	Advanced High Strength Steel
CGA	Circle Grid Analysis
CSR	Concave Side Rule
DIC	Digital Image Correlation
DP	Dual Phase (Steel)
FLC	Forming Limit Curve
FLD	Forming Limit Diagram
FLSD	Forming Limit Stress Diagram
HER	Hole Expansion Ratio
HS	Hot Stamping (or Hot Stamped)
HSLA	High Strength Low Alloy
ISO	International Organization of Standardization
LDH	Limiting Dome Height
MMC	Modified Mohr-Coulomb
PEPS	Polar Effective Plastic Strain
PLC	Portevin-Le Chatelier
RD	Rolling Direction
TD	Transverse Direction
UHSS	Ultra High Strength Steel
VDA	German Association of the Automotive Industry (Verband der Automobilindustrie)
VSGL	Virtual Strain Gauge Length

1.0 Introduction

Material formability is a key metric for the consideration and adoption of new materials in the automotive industry. Materials with good formability provide a wide range of options for process design and can minimize the number of physical die tryouts. Steels and aluminum alloys have always been the preferred materials for automotive structural components due to their combination of strength, density, and formability. The first commercialized vehicle was designed by Karl Benz in 1885 with wood panels and steel tubes while the modern vehicle architecture in 2018 is built upon advanced and ultra-high strength steels and aluminum alloys for improved safety in a crash event.

With the rapid development of forging techniques in the early 20th centuries such as power-hammering and stamping, the all-steel body became the new trend of automotive design due to its ease of manufacturing and durability. The first completely steel vehicle was introduced by Dodge in 1916 and the architecture has remained steel-focused with continual improvements in steel alloy development from low strength mild steels to high-strength low-alloy (HSLA) steels, and 1st generation advanced high strength steel (AHSS). Generally, an increase in the strength of a steel alloy corresponds to a decrease in ductility as shown in the classic “banana” diagram for automotive steels shown in Figure 1. Note that ductility refers to the percent elongation measured from tensile tests.

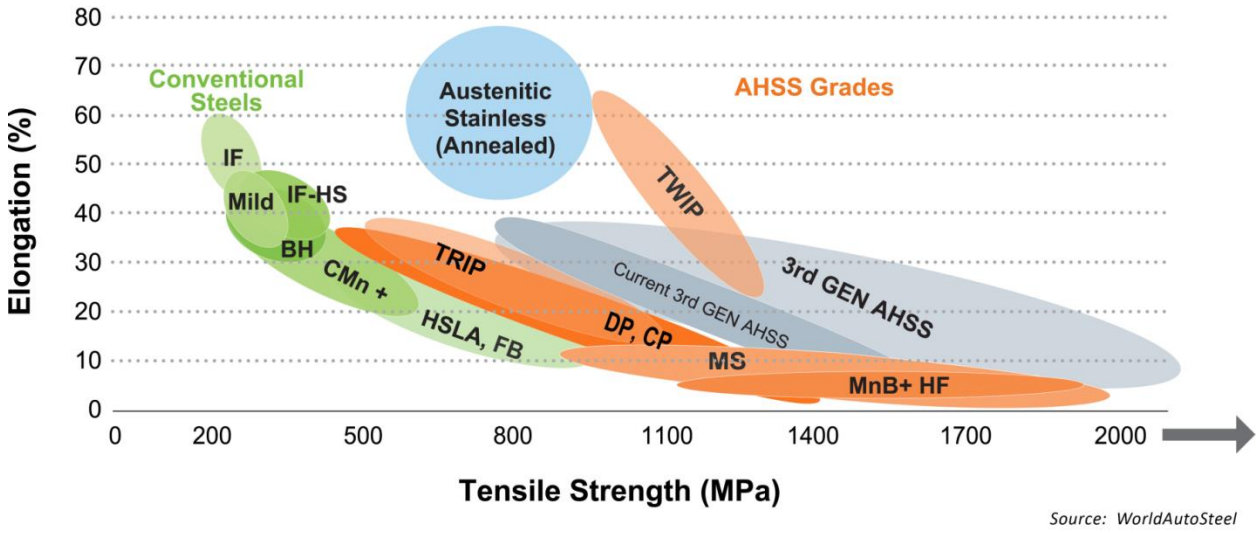

Figure 1 Comparison chart between tensile strength and global formability of materials, often called "banana diagram."

Concerns regarding global climate change and North American dependency on foreign oil and gas have accelerated the lightweighting of vehicles since the Corporate Average Fuel Economy (CAFÉ) emission standards of 2009. Advanced and ultra high strength steels and aluminum alloys have been very competitive candidates for vehicle lightweighting and crashworthiness. With these next-generation alloys the industry has focused upon lightweighting by the consolidation of components using advanced forming operations and through down-gauging to reduce thickness by using higher strength alloys. Material substitution, such as replacing steels with high strength aluminum alloys can also provide significant potential for lightweighting. However, the complex multi-phase microstructures of these advanced alloys result in a sensitivity to fracture in different stress-states that has led to challenges in the virtual design of forming operations and prediction of crash response. In some respects, advances in alloy design have out-paced the ability to characterize the mechanical properties of the alloys to support computer-aided engineering (CAE) simulations to design components using next-generation materials. Material models for formability and fracture based upon traditional test parameters such as a forming limit diagram and tensile test data have struggled to provide accurate predictions in the simulations leading to additional process “quality loops” to modify the tooling, component geometry and perform additional die try-outs. In particular, the characterization of the formability and fracture behavior of advanced automotive

materials in stress states from uniaxial tension to biaxial stretching is required. Emphasis is on the performance in bending-dominated loading conditions which can be representatives of local folding and buckling during a crash situation.

1.1 Global Formability and Forming Limit Diagram

The ductility of sheet materials, often called global formability, has been traditionally classified using a forming limit diagram (FLD) or forming limit curve (FLC) since their introduction by Keeler and Backofen (1963) and Goodwin (1968). This global formability is referred to the ability to resist localized necking and involves with a large scale forming operations such as stretch forming of the sheet. The forming limit diagram relates the critical values of major and minor strain under in-plane stretching conditions. These critical values correspond to the onset of a local or acute neck that is a strain instability. The onset of the necking process is defined as a "diffuse neck" while an acute neck corresponds to a marked change in the surface geometry prior to fracture, see Figure 2. The definition of an acute neck is somewhat broad and in the early work of Keeler, a local neck would correspond to feeling a surface discontinuity when running one's fingernail across the part.

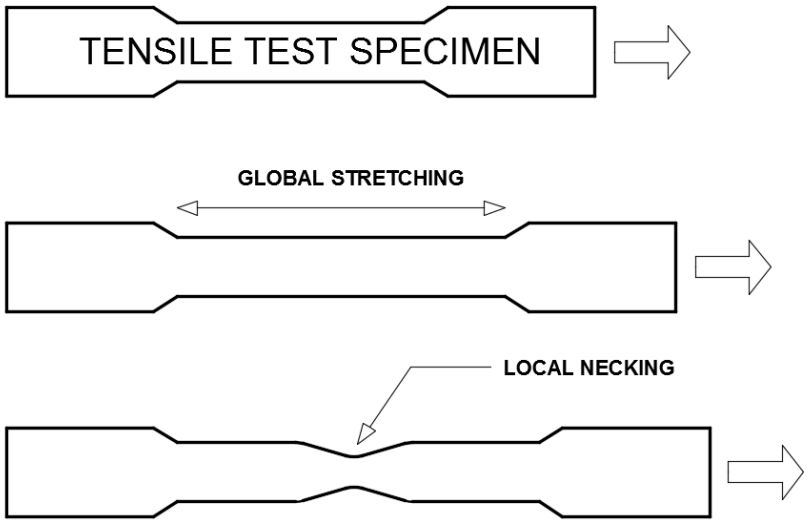

Figure 2 Illustration of global stretching (middle) and necking with local deformation (bottom). Significant reduction in the deforming area is observed due to the local thinning.

Machining defects, local variations in composition and material imperfections such as voids or a non-uniform thickness can initiate the necking process. The onset of local necking in a component generally requires the part to be scrapped as its surface quality is flawed in the case of outer body panels that will be painted or due to the structural integrity being compromised in a structural part. In 1885, Considére described the fundamental concepts of diffuse necking based on strain hardening where the onset of a diffuse neck corresponds to reaching the peak force or ultimate tensile stress (UTS). Later, the study of Hill from 1952 provides a necking model which predicts acute necking based upon the zero-extension band angle in uniaxial-type stretching. However, this model is only valid on the draw side of the FLC and does not account for the effect of diffuse necking. These insights were further investigated by other researchers and a well-known localized necking prediction model was proposed based on studies of Marciniak and Kuczyński (1967), Marciniak *et al*. (1973) and Hutchinson and Neale (1977), often referred to as the M-K model. The MK model can predict the forming limit strains based upon an assumed thickness imperfection in the material that develops into a local neck during deformation. There is a vast amount of literature employing the MK framework to predict in-plane formability with notable applications by Barlat (1987), Zhao *et al.* (1996), Kuroda and Tvergaard (2000), Wu *et al.* (2003), Aretz (2007), and Chu *et al.* (2014). Despite its widespread use, MK models first require knowledge of the experimental forming limit diagram to calibrate the imperfection parameters to then apply the MK model for other loading conditions.

The conventional method to construct an FLD involves with the use of Limiting Dome Height (LDH) test, often called the Nakazima test (Nakazima *et al*., 1968), that use a hemispherical punch. Another well-known method is the Marciniak test (Marciniak and Kuczynski, 1967) that utilizes a cylindrical punch with a flat top along with a carrier blank or "washer" with a central hole that is used to stretch the test piece. The experimental setups for the Nakazima and Marciniak tests are illustrated in Figure 3.

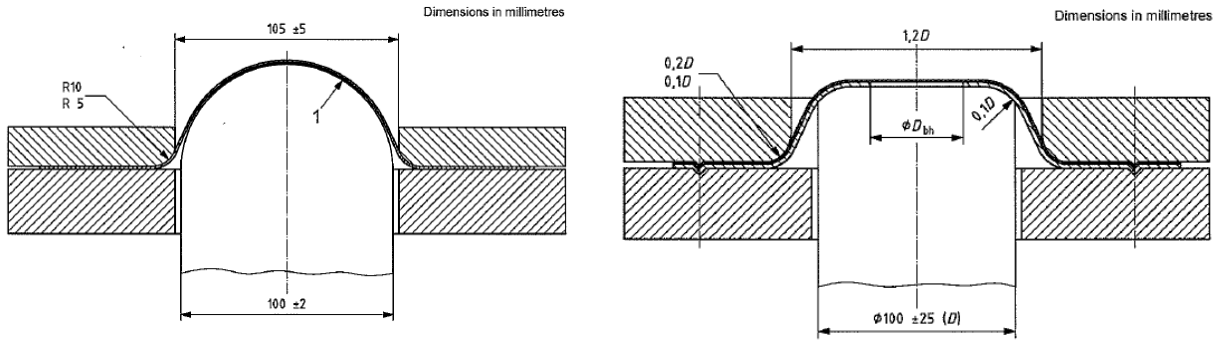

Figure 3 Difference between Nakazima (left) and Marciniak (right) test equipment. Figures are taken from ISO 12004-2 (2008).

The concept of using dome tests to determine formability was already introduced by Erichsen and Olsen (1920) in the 1920s but fell out of favor due to the combination of stretching and bending with the small punch radius of 10 mm. To isolate in-plane stretching conditions, larger punches were advocated with a 100 mm diameter punch proposed by Nakazima (1968) that has obtained worldwide acceptance and standardization in ISO12004-2 (2008). Even though the Marciniak test provides an ideal in-plane stretching condition without the effect of contact pressure or surface friction, the complexity of controlling the failure location using the carrier blanks is problematic. The carrier blank dimensions, central hole size and thickness often require changing for each material system. Nakazima suggested an alternative solution for such problems by employing a hemispherical punch of 100 mm diameter. The nature of hemispherical shape effectively prevents the edge crack around the punch nose, and more importantly, the failure is likely to happen in the apex of the dome since the specimen is gradually engaged starting from the center. Moreover, the increase in stability makes it possible to perform the test without a carrier blank. As a result, the convenience of this test standard obtained a rapid acceptance in the field of formability and it is still considered as a fundamental formability test for material characterization.

Three fundamental testing conditions to construct FLDs are uniaxial tension, plane strain tension, and equi-biaxial tension. Figure 4 is a brief visualization of those three representative strain conditions. Under these conditions, ideal strain distributions for an isotropic material would be:

Uniaxial Stretching $\rightarrow \quad \varepsilon_1 = -\varepsilon_2 - \varepsilon_3 = -2\varepsilon_2$

Plane Strain Stretching $\rightarrow \quad \varepsilon_1 = -\varepsilon_3 , \quad \varepsilon_2 = 0$

Equi-biaxial Stretching $\rightarrow \quad \varepsilon_1 = \varepsilon_2 , \quad \varepsilon_1 + \varepsilon_2 = -\varepsilon_3$

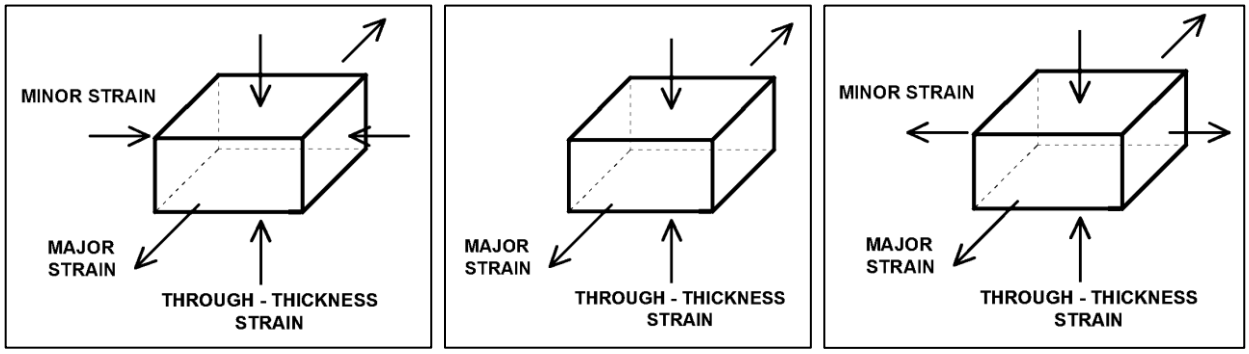

Figure 4 Illustrations of strain elements of uniaxial (left), plane strain (middle), and biaxial (right) stretching. Generally, the plane strain has the most conservative formability due to the lack of minor strain component.

The strain path is a history of strain development during deformation, often expressed in the major versus minor strain space, and it is a very important feature to describe the deformation process. Each strain-state corresponds to the stress-state and the stress can be determined indirectly from the strain measurements by assuming a yield function and hardening law for the material. Based on the strain-state, each path has a unique slope corresponds to stretching condition. For example, a plane strain tension condition can be expressed as a vertical path along the major strain axis since the minor strain remains zero. Similarly, a uniaxial stretching path for an isotropic material corresponds to a linear path with a slope of -2 while the biaxial stretching strain path has a slope of 1, see Figure 5. Even though these three strain conditions are the most common and fundamental test conditions to generate FLD, strain paths with any other strain ratio can be obtained by changing the width of the test coupons. Industrially-relevant FLDs require a minimum of 5 different strain paths according to the ISO12004-2 standard.

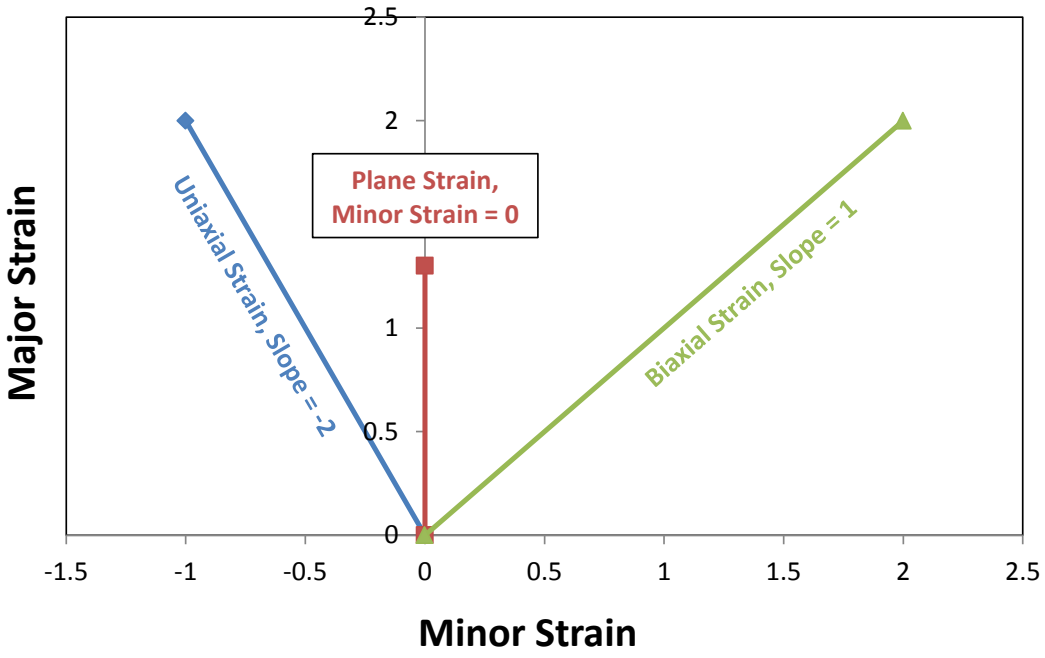

Figure 5 Illustration of ideal linear strain paths until fracture corresponding to uniaxial (blue), plane strain (red), and biaxial (green) stretch conditions

The construction of an FLC relies upon proportional loadings which correspond to linear strain paths. Even though most of the actual operations experience non-linear loading, the linear strain path is still critical in material characterization perspective since it provides a unique mapping between the material performance and strain state. The influence of non-linear strain paths on formability will be discussed in Section 1.2.

As shown in Figure 6, the strain path is terminated at the onset of fracture which creates a fracture forming limit curve (FFLD), or simply the fracture limit. Unlike these fracture limits, which can be identified by the physical separation of the specimen, the forming limit is determined by the onset of acute necking which can be hard to define objectively.

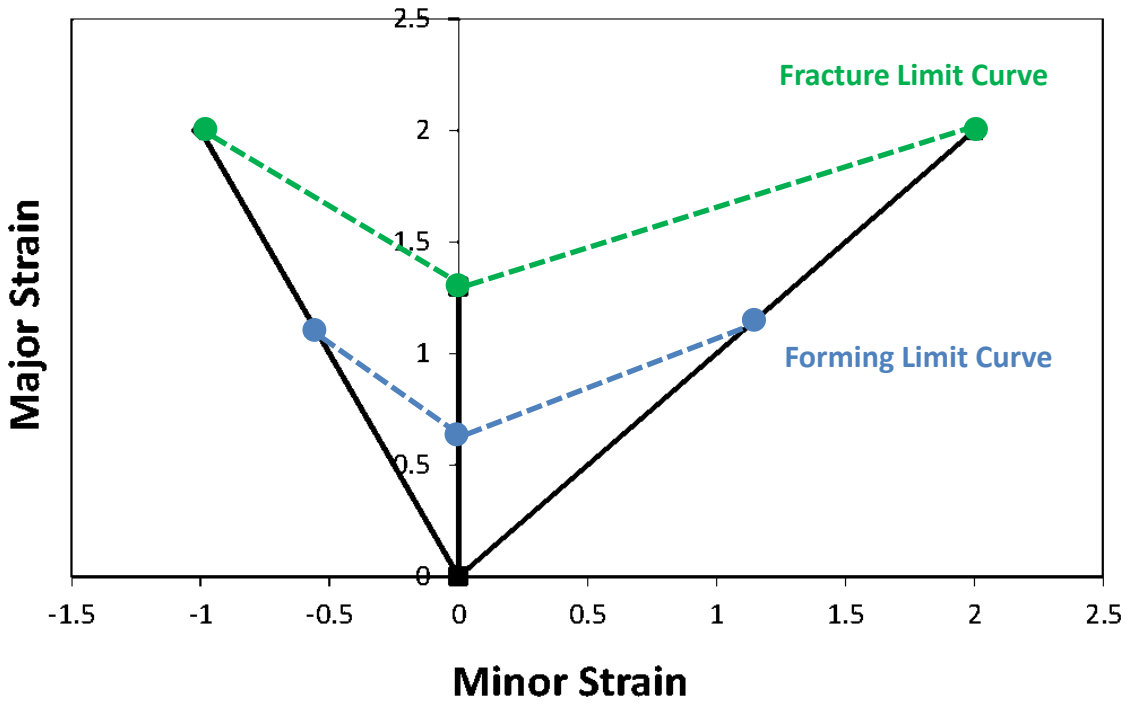

Figure 6 Schematic of forming limit curve (FLC) and fracture forming limit curve (FFLC). The connection of fracture locations becomes a fracture limit curve (green dashed line), and the connection of the onset of necking becomes forming a limit curve (blue dashed line). These curves typically form V-shape due to limited formability under plane strain condition.

The traditional method of experimental limit strain determination has been the circle grid analysis (CGA) by Keeler (1968). This technique employs tiny circles etched onto the surface of the specimen and the strains can be estimated based on the change of the circle in the area of interest. This method has limited resolution depending on the circle size and spacing. Only a final strain measurement can be achieved and no history of deformation is available thus the effects of the non-linear path are lost. It is also challenging and often subjective to determine the limit strains which are estimated from circles near the crack. Therefore, the result of CGA tended to vary between analysts and have a large variation in FLCs.

Major progress in the field of limit strain was made by ISO 12004-2 (2008) which led to repeatable practice between labs and improved repeatability and accuracy in the limit strain determination. The development of stereo DIC has revolutionized FLC determination since the full-field of strains can be measured to high resolution throughout the deformation process. Various aspects of deformation were then able to be investigated such as non-linear strain paths and strain rate at the necking location. With

DIC, the field has started to develop new methodologies for limit strain determination. In 2011, Volk and Hora introduced a time-dependent algorithm which investigates a rapid acceleration of strain rate caused by strain localization. This method is more physical than the parabolic-fitting of the strain distribution by ISO 12004-2 (2008). Similar approaches can also be found from studies of Merklein *et al*. (2010) and Hotz *et al*. (2013). Also, DiCecco *et al*. (2016) and Min *et al*. (2017) have suggested a method to detect the local thinning based on the change in curvature of the deforming surface.

1.2 Effect of Nonlinear Strain Path

In the actual operation and testing, the strain path often becomes non-linear if the stress-state changes during the deformation. For example, Nakazima tests using a hemispherical punch usually experience non-linear strain path as the specimen wraps around the punch in initial contact and experiences a combination of biaxial bending and stretching, see Figure 7. Depending on the test design, many other shapes of non-linearity could occur.

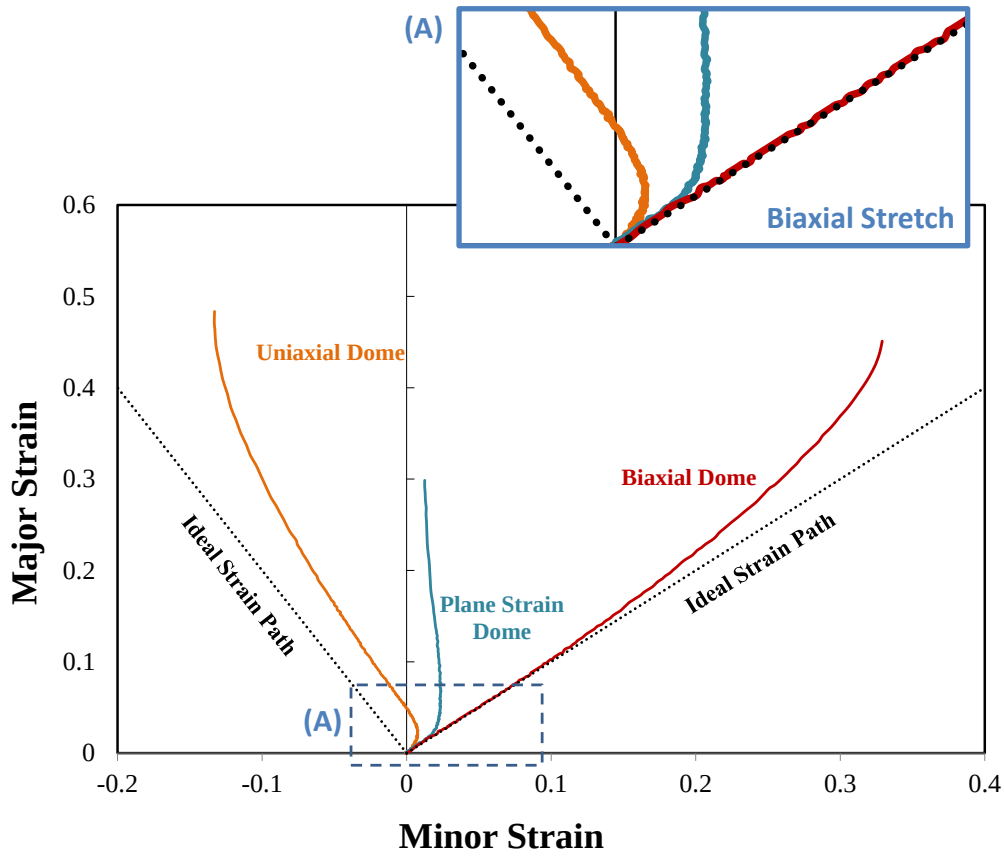

Figure 7 Representative strain path of DP980 sample for FLD using Nakazima punch until fracture. Biaxial stretching is observed from all three paths in an early stage due to the hemispherical shape of the punch. Increase in major strain becomes dominant at the end due to the localized deformation.

The deviation from a linear strain path and constant stress state can have a significant influence on the construction of FLC. In 1993, Graf and Hosford studied the effect of the change in strain path by applying pre-straining to AA6111-T4 material. Different levels of pre-straining were applied in uniaxial and biaxial strain directions and then samples were tested to construct FLCs. As shown in Figure 8 and Figure 9, the result clearly indicated that the effect of non-linear strain path should not be neglected.

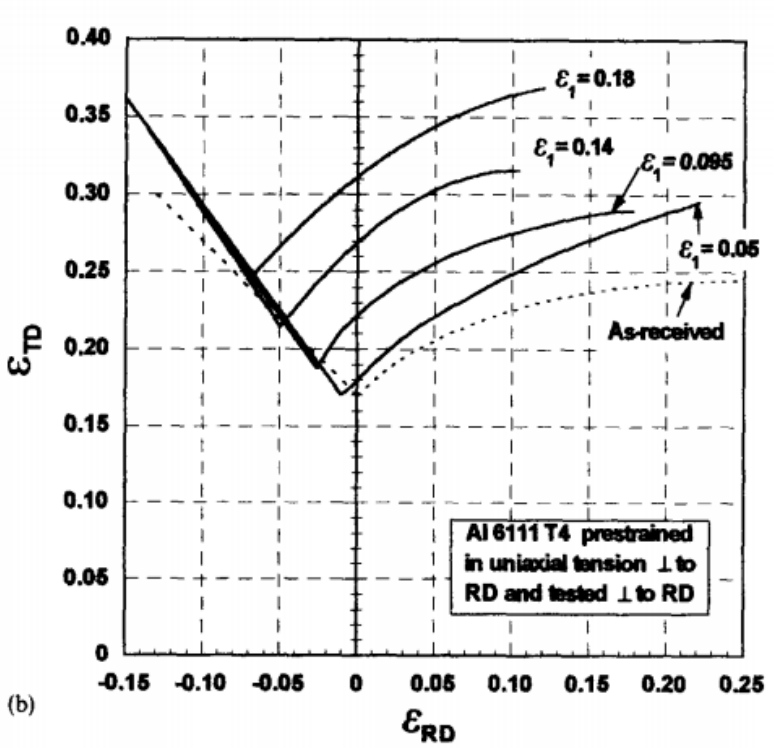

Figure 8 FLCs from pre-strained specimens in uniaxial tension reported by Graf and Hosford (1993)

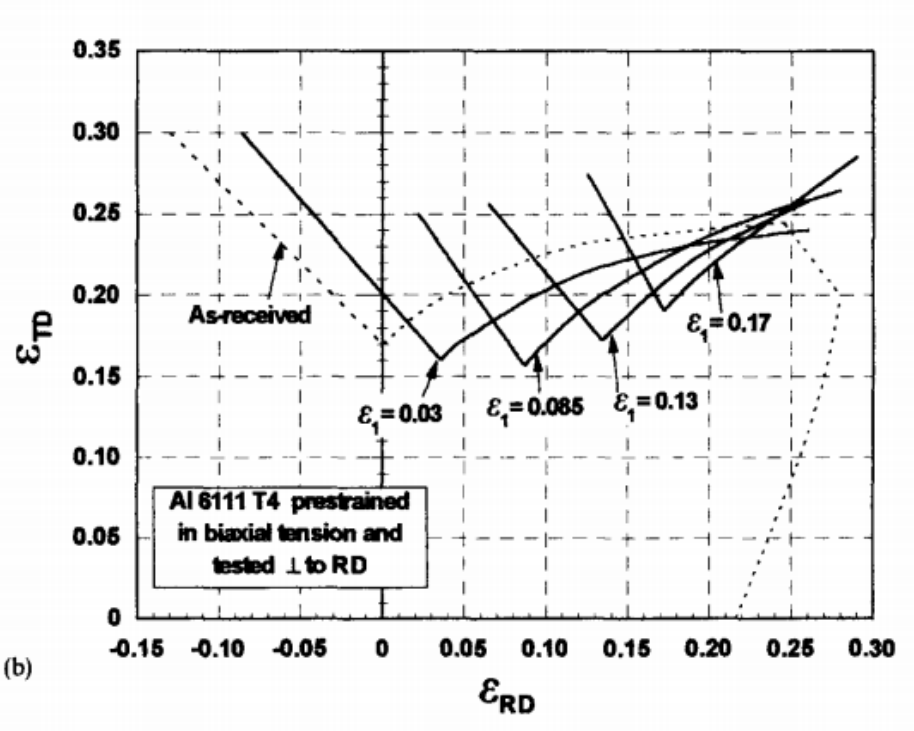

Figure 9 FLCs from pre-strained specimens in biaxial tension reported by Graf and Hosford (1993)

Moreover, non-linearity in the strain path can also occur at the end of the deformation. As diffuse necking starts, a rapid acceleration could occur in major strain development. As shown in Figure 7, in the latter stage of the process, the increase in major strain overwhelms the increase in minor strain due to the localized deformation from necking. As a result, the strain paths diverge from their ideal paths and tend to point upward similar to the plane strain state which has the most limited formability.

It is well-known that the nonlinear strain paths have a significant impact on the limit strains. Muschenborn and Sonne (1975) investigated the nonlinear strain path behavior using work-equivalent plastic strain to better account for non-linear strain path effects. Forming limit stress diagram (FLSD), which are theoretically independent of the strain path for isotropically hardening materials was introduced by Kleemola and Pelkkikangas (1977), and Arrieux *et al*. (1982) based on Muschenborn's approach. Various following researches are published such as Zhao *et al*. (1996), Haddad *et al*. (2000), Stoughton (2000), and Stoughton and Zhu (2004) who have all reported the insensitivity of FLSD to the shape of strain path. This approach successfully eliminates the strain path dependency as shown in Figure 10 that strain paths from various level of pre-straining in strain-based FLD (left) coincide with each other in stress-based FLD (right).

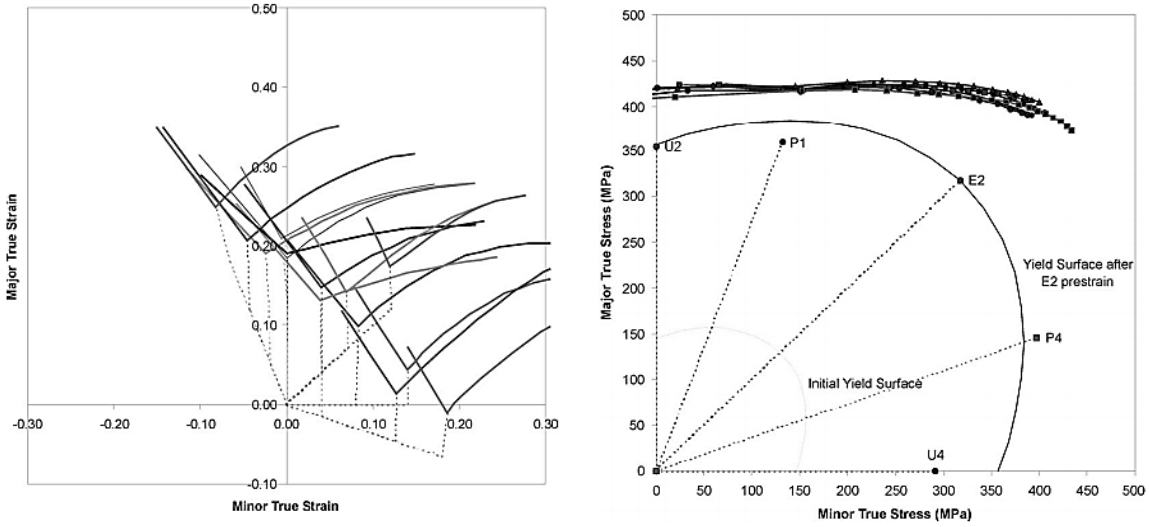

Figure 10 Comparison between strain-based (left) and stress-based (right) FLD reported by Stoughton and Zhu (2004)

However, this technique did not draw much attention from industry due to the complexity and the ambiguity of using the concept of stress when strain is more intuitive representative of deformation that can be directly measured on a part using circle-grid analysis or DIC. Stress-based representations also require the analyst to assume a yield function and hardening law which is non-trivial and restricts the data to the assumed constitutive framework and its calibration parameters. Strain-based FLCs have the advantage of being experimentally measured without requiring such assumptions. The study of Stoughton and Yoon (2011, 2012) extended the idea of stress-based FLD and introduced the concept of polar effective plastic strain (PEPS). The core idea of the study was to combine the advantages from both stress and strain metrics to develop a diagram that looks familiar like the well-known FLC but is constructed in terms of the equivalent strain that is more intuitive than the stress-based FLC. A similar approach to merging the advantages from stress- and strain-based FLD can also be found from the study of Min *et al*. (2016) who proposed a method to compensate the effect of nonlinear strain path, curvature, and through-thickness stress in Nakazima dome tests. A series of corrections were developed to account for nonlinear strain path effects and tool contact pressure for an FLD obtained using Nakazima tests so that it approximates the Marciniak FLD that is under perfect in-plane stretching.

1.3 Curvature and Out-of-Plane Deformation

Many researchers have stated that the traditional material characterization metrics based on FLD may not apply to certain failure modes found in practical forming operations. The FLC is only valid for in-plane necking-induced failure under approximately proportional loading conditions. Non-linear strain paths and out-of-plane deformation are excluded. It is well-known within the field of sheet metal forming that the superposition of stretching with out-of-plane deformation due to bending can delay strain localization. In 1974, Ghosh and Hecker observed that the bending on deformation has a positive influence on formability of a metal sheet. This phenomenon also agrees with more recent studies of Tharrett and Stoughton (2003), Yoshida *et al.* (2005), Morales-Palma *et al.* (2013), and Min *et al.* (2016) who have all reported that a through-thickness strain gradient, which is generated by out-of-plane deformation, can significantly alter

the necking behavior. An analytical prediction of stretch-bend behavior from the study of Yoshida *et al.* (2005) is shown in Figure 11. It is clearly illustrated that there is a strong correlation expected between the limit surface strain and bending curvature under various hardening coefficients, *n*. Moreover, differences between dome tests with various severities of the bend are illustrated in Figure 12 from the study of Min *et al.* (2016).

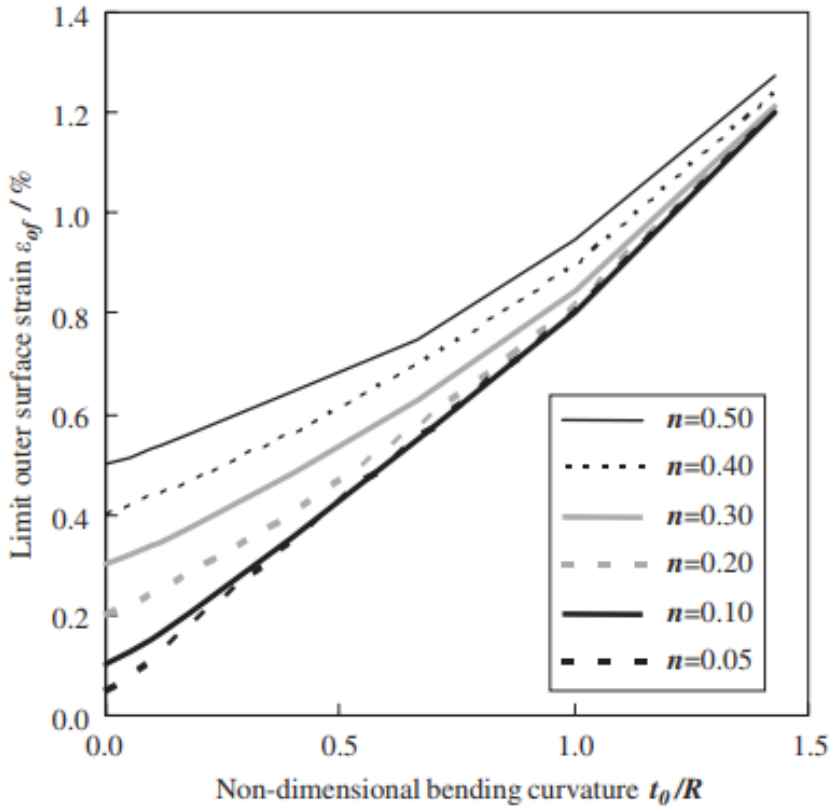

Figure 11 Analytical prediction of the relationship between bending curvatures and limit outer surface strain under stretch-bending from the study of Yoshida *et al.* (2005)

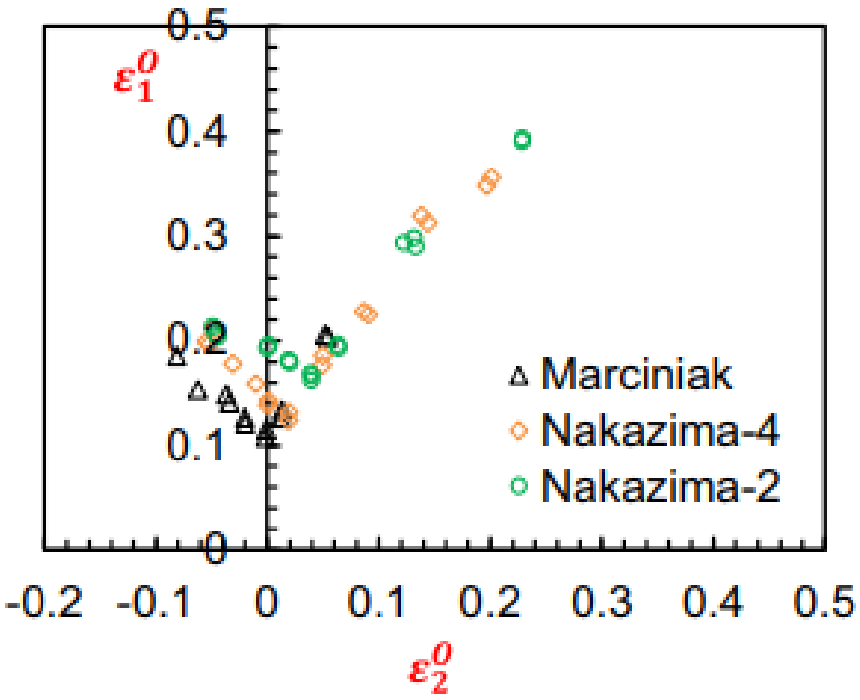

Figure 12 FLCs from various dome punches reported by Min *et al.* (2016). Marciniak and Nakazima-4 employed a 4" (101.6 mm) punch diameter whereas Nakazima-2 used a 2" (50.8) mm punch diameter.

Moreover, most practical sheet metal forming operations involve out-of-plane deformation and bending as the material is stretched over a punch and pressed into a die. Ideal in-plane stretching of the sheet occurs in some regions of the part such as in side-walls during drawing operations but there is also bending and un-bending over draw-beads and tool surfaces. In vehicle crash events of structural components, out-of-plane bending and compression are the dominant deformation modes.

The use of strain-based FLCs to design forming operations is still the most common technique used in industry. The FLC is applied to out-of-plane regions of the component and whether necking will occur is based upon the experience of the analyst. There is a clear need to improve the virtual prototyping and simulation capabilities to differentiate between failure due to in-plane stretching and due to bending or a combination of stretching and bending. Notable studies on the influence of bending on tensile instability have since been performed by Hecker and Ghosh (1974), El-Domiaty *et al.* (1996), Leu (1997), Tharret and Stoughton (2003), Kitting *et al.* (2011), and Centeno *et al.* (2014) who investigated the mechanism of bending, which is often referred as a representative of out-of-plane deformation.

One of the key features to describe the bending behavior is the severity of the bend. It is often numerically quantified by the ratio between the sheet thickness and the bend radius, *t/R*. During pure bending, the convex side of the bend (outer surface) experiences tension and the concave side experiences compression as shown in Figure 15. Due to this non-uniform status through the thickness, a strain gradient is generated with a neutral layer where neither tension nor compression is observed. Generally, more severe bending provides a stronger strain gradient. In sheet metal forming the bending mode is one of plane strain since the width of the sheet is generally much larger than the sheet thickness. The width strain remains approximately zero.

It is very important to understand that the strain gradient has a critical impact on stain instability. Even though the outmost layer reaches the critical strain limit from FLD, the inner layers that are in moderate tension or compression provide stability and serve to mitigate necking. In 2003, the empirical concave side rule (CSR) was proposed by Tharrett and Stoughton which stated that strain instability occurs only when all of the material layers in the sheet have exceeded the forming limit strain. As a result, in forming operations with in-plane tension and out-of-plane bending, the initiation of necking is delayed until the innermost layer has reached the limit strain, see Figure 14. As noticed by Min *et al*. in 2016, the fact that corrections are required even for a moderately small bending severity in standard Nakazima tests clearly demonstrates the importance of a strain-gradient on delaying necking. In pure bending, the bottom layers of the material are always in compression such that necking is suppressed and fracture will occur on the outer layer where the tensile stress is highest.

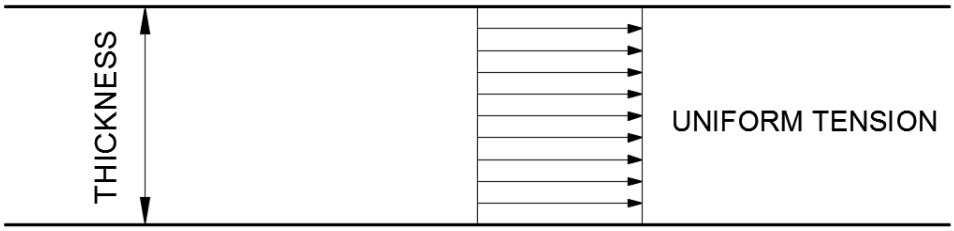

Figure 13 Illustration of an in-plane stretching process that the tensile stress is uniform through the thickness of the sheet. The tensile direction is the major strain direction.

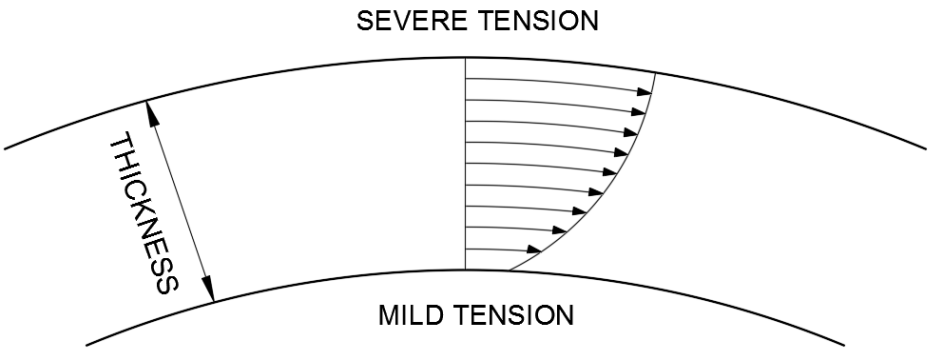

Figure 14 Illustration of an out-of-plane stretching with superimposed in-plane stretching often observed in stretch-bending operation. Outer surface experiences severe tension and inner surface experiences relatively mild tension. If the innermost layer exceeds the forming limit of the material, the neck may happen.

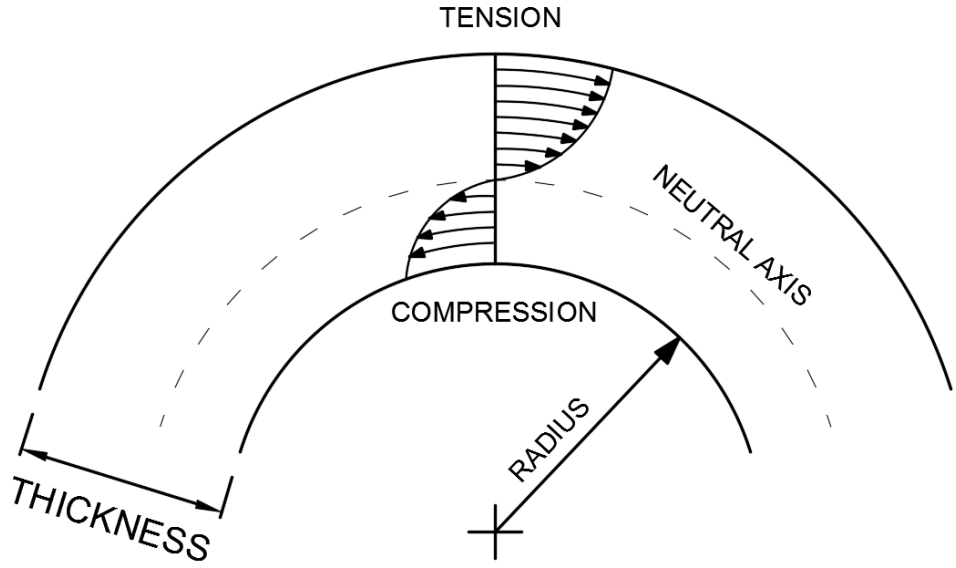

Figure 15 Illustration of an out-of-plane stretching with severe strain gradient. Layers outside of the neutral axis experience tensile loading and inner layers experience compression. Due to the difference between the tensile and the compressive response of the material, the neutral axis is often not in the center of the sample.

1.4 Local Formability and Fracture Characterization

As described in Section 1.1, global formability can be described as a uniform distribution of the strain throughout the gauge length. However, this uniformly strained condition becomes unstable with the onset of localization. With the presence of localized necking, the deformation is concentrated into a smaller region and the local formability becomes critical. In contrast to global formability, the local formability is an important feature to describe the post-necking stage of material deformation such as fracture resistance. Many fracture limit tests like hole expansion for measuring stretch flange-ability and tight radius bend tests are also local formability tests that a specific region of the material is subjected to localized deformation based upon the tooling geometry such as forming a desired radius based upon a lockbead or drawbead. The application of local formability can be found in many existing forming operations such as hemming, tube bending, flanging, and local buckling and folding of structural components in a crash event.

It is very important to understand that having good global formability does not translate into having a good fracture resistance or crash performance. The study of Walp (2007) has reported a positive correlation between the fracture limit and bendability using AHSS and UHSS. In 2009, Dykeman *et al.* have investigated the local formability and edge-stretchability of various level of DP steels using hole expansion and bending tests. Moreover, correlations between the fracture limit and hole expansion test were reported by Link (2008) and Link and Chen (2013). In addition, Hance (2016) has investigated the local and global formability of AHSS with a tensile strength of 980 MPa in various aspects. In spite of valuable findings from these studies, all these studies have reported that there is no strong correlation between the local and global formability. The recent recognition of the difference between the global and local formability has provided new insights in the industry and material suppliers started to provide local formability test data such as the VDA 238-100 bend angle to supplement the mechanical property data.

In the field of vehicle crashworthiness, the material fracture behavior in the presence of severe through-thickness strain gradients is a critical factor since components often experience multiple folds as shown in Figure 17 and Figure 18. Since the structure can absorb the impact energy until it is completely ruptured, an accurate estimation of the fracture strain is required. During the crash test of B-pillar and axial crush specimens, test subjects mostly failed by local folding around the impact which also emphasizes the importance of local formability (Figure 16 to Figure 18).

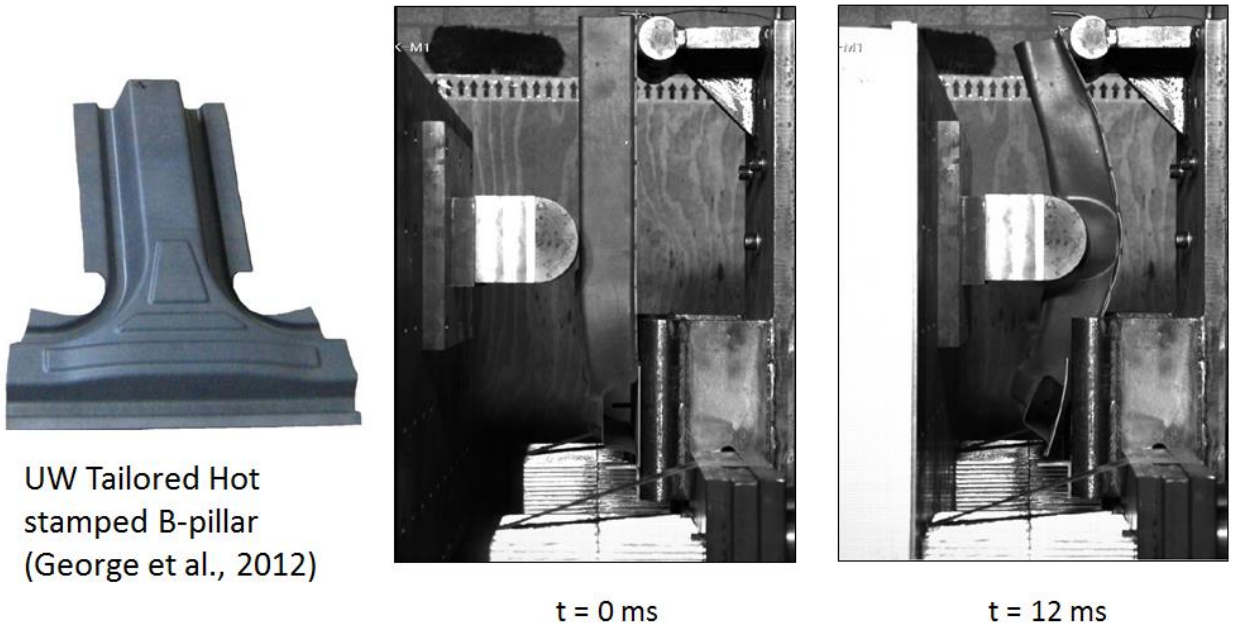

Figure 16 Test setup of lab-scaled B-pillar side impact test by George *et al.* (2012)

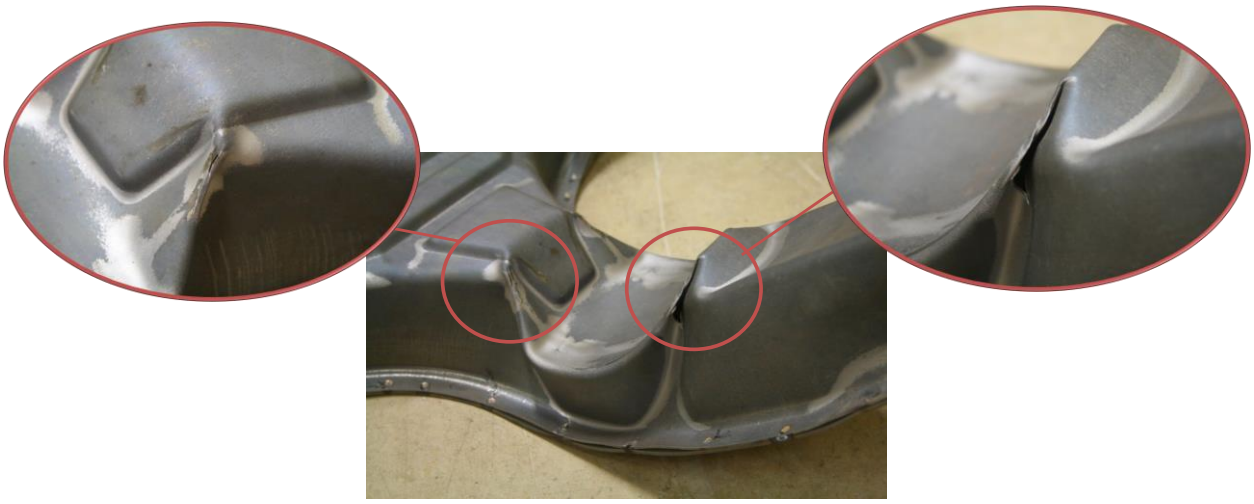

Figure 17 Failed specimen from side impact test (Figure 16). Cracks were observed at the edge of the impact zone where severe local folding exists.

Figure 18 Picture of a lab-scale axial crush specimen (DP980) after the impact test. The component failed in sharp folding

Although through-thickness strain gradients are undesirable for FLD determination, they can be exploited for fracture characterization. The development of stress-state dependent fracture models such as the Modified Mohr-Coulomb (MMC) (Bai and Wierzbicki, 2010) or GISSMO model (Effelsberg *et al*. 2012) were based upon fracture occurring under proportional loading. To obtain the fracture strains to calibrate these models, the characterization tests must avoid the onset of a tensile instability that changes the strain path and stress state. Current methods for fracture characterization employ tensile-based coupons such as notched tensile tests that the stress state is very non-linear due to localization. Inverse-finite element models are then employed to determine the failure strains as done by Dunand and Mohr (2010). Alternatively, by intentionally imposing a severe through-thickness strain gradient it may be possible to

suppress the onset of necking so that cracking occurs on the surface under a proportional strain path and the failure strain can be measured using DIC.

1.5 VDA 238-100 Tight Radius Bend Test

As demonstrated in Figure 16 to Figure 18 from the impact tests, the local regions near the impact zone in the B-pillar and within the folds of the axial crush test can be approximated as severe tight radius bending in-plane strain. Given that the ductility of metals is always the lowest in plane strain the accurate identification of the fracture strain is critical for material selection for energy-absorbing components. In 2010, the German VDA238-100 specification was introduced for tight radius three-point bending (or v-bending) of sheet metals and has since received rapid and widespread acceptance with automotive suppliers and material producers to characterize local formability. The general setup of the test is shown in Figure 19. A very sharp punch tip radius (0.2 or 0.4 mm) with a minimal roller spacing provides a tight radius bending condition under plane strain. The simplicity, consistency and detailed specifications on the tooling and test parameters are the strength of the VDA guideline that has led to its widespread acceptance.

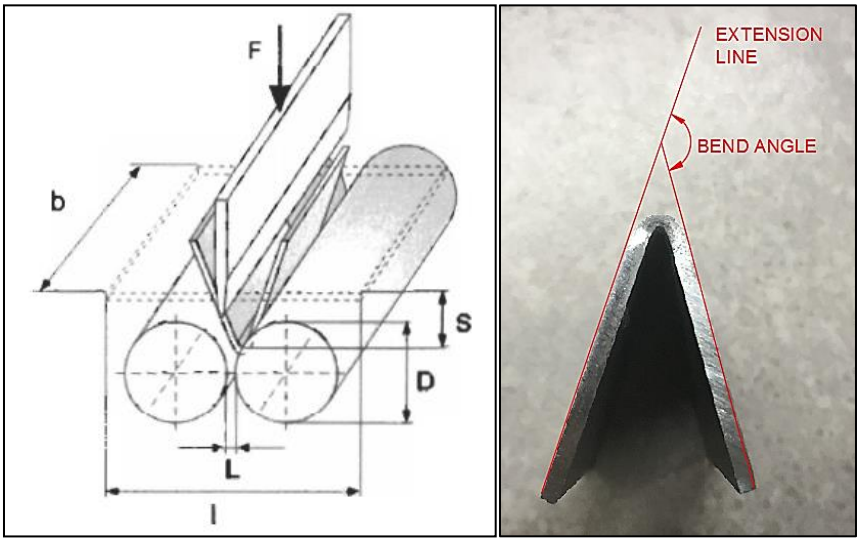

Figure 19 Illustration of general setup of VDA 238-100 tight radius bend test (left) and the definition of the bend angle (right).

However, the test fixture and tooling in this standard is not amenable to direct strain measurement, and the operator cannot terminate the test at the onset of crack initiation as the outer bend surface is not visible. Consequently, the onset of fracture is identified using a load threshold and the bend angle has to be estimated from an analytical formula based on the punch displacement and tooling geometry. More importantly, materials with the same bend angle can have distinct stress- and strain-states depending on the bend radius and sheet thickness. Therefore, the angle measurement is not directly transferable and must be interpreted relative to the bending condition unlike a strain measurement. Larour *et al*. (2012, 2013) investigated the VDA bend test methodology and reported potential experimental errors embedded in the test design. A comparison with the traditional bend angle calculation from ISO 7438 (2005) was also reported in this study and the analysis indicated that the mathematical correlation provided by VDA 238-100 tends to have better accuracy. However, it is important to note that the VDA correlation is a customized formula specifically prepared for VDA test setup whereas the ISO correlation can be applied to any type of three-point bending. Moreover, Neuhaus and Borsutzki (2013) applied an optical method to record the bend angle during the process, but the fundamental limitations of characterizing the test in terms of bend angle still exist.

1.6 Current Work

Current material characterization techniques are still heavily relying on traditional metrics of formability such as the total elongation (ductility) and the in-plane forming limit strains. However, these metrics are primary measures of global formability and may not be sufficient to describe current generation materials that can have high local ductility and fracture resistance in a vehicle crash despite having a relatively low forming limit. Traditional formability metrics would indicate these materials would perform poorly although they may be superior in a crash application. Therefore, the main theme of the research presented in this thesis was to evaluate the influence of through-thickness strain gradient on formability and fracture behavior. The primary focus was on local formability associated with fracture characterization under proportional strain paths. An experimental investigation to develop and evaluate the characterization tests

was performed. The range of interest covered the proportional loading conditions from the uniaxial tension to equi-biaxial stretching and other strain conditions within the range.

A novel test apparatus for an inverted VDA test was developed in the University of Waterloo to incorporate DIC strain measurement during the bend test. The first objective of this research involved the construction of a test procedure and analysis, validation and verification of the test design, and fracture characterization using the VDA bend test. The VDA bend test is designed to provide a pure bending condition which is a representative out-of-plane deformation. The deformation is under plane strain state that the lowest formability of the sheet can be observed. A wide range of automotive metals was tested using the apparatus to investigate the plane strain fracture limit and the forming behavior with the presence of significant through-thickness strain gradient.

The second objective of the thesis was involved with applying the through-thickness strain gradient on equi-biaxial stretching condition. A modified punched dome test was developed based on the conventional Nakazima test but employing miniature hemispherical punches to introduce severe through-thickness strain gradient to deforming area. With the similar analytical approach from the VDA bend test, the strong through-thickness strain gradient was expected to suppress the onset of necking, thus the fracture behavior can be accurately characterized.

Since in-plane stretching and out-of-plane bending were separately studied using the miniature dome test and the VDA bend test, this research required a connection between these two representative stress-states. Therefore, a stretch-bending test tool was developed to investigate the inter-relationship between necking and fracture by varying the ratio of stretching and bending. In contrast to the other two tests in which complete suppression of necking was desired, the necking in stretch-bending would still exist and it was one of the major research interests. The effect of curvature on forming limit strain would be emphasized in this section instead of fracture characterization.

Lastly, collected data from out-of-plane forming tests were organized and rearranged to construct an out-of-plane fracture limit curve which indicates the conditional forming range of sheet metal with the presence of through-thickness strain gradients. Moreover, the traditional Nakazima test and the hole expansion test were also performed to complete the formability analysis under the effect of bend severity.

2.0 Material Selection

A variety of automotive sheet metal alloys have been considered in this research for evaluation of the formability tests. However, the focus materials of interest are two DP980 steels and an aluminum alloy, AA5182, since they provide a stark contrast in strength, ductility, and hardening behavior. Aluminum AA5182 is not a structural alloy like DP980 and is used for closure applications such as door inner panels. Additional alloys of interest include DP600, a lower strength advanced high strength steel and HS1500, an ultra-high strength hot-stamped steel with an ultimate tensile strength of 1500 MPa. The DP600 and DP980 have a dual-phase microstructure consisting of ferrite and martensite whereas HS1500 is hot-stamped Boron steel, USIBOR® 1500-AS, that has been quenched to a fully martensitic condition.

Two DP980 steels with different thicknesses were selected to provide a clear identification of the effect of bend severity. The first DP980, with the thickness of 1.2 mm, has a chemistry of C-Mn-Si and showed a fine and uniform microstructure. Another DP980 with the thickness of 1.6 mm has a chemistry of C-Mn-Cr-Mo-Nb with zinc coating and has a relatively finer and equiaxed microstructure that provides markedly high yield strength relative to earlier DP980 variants, see Figure 20.

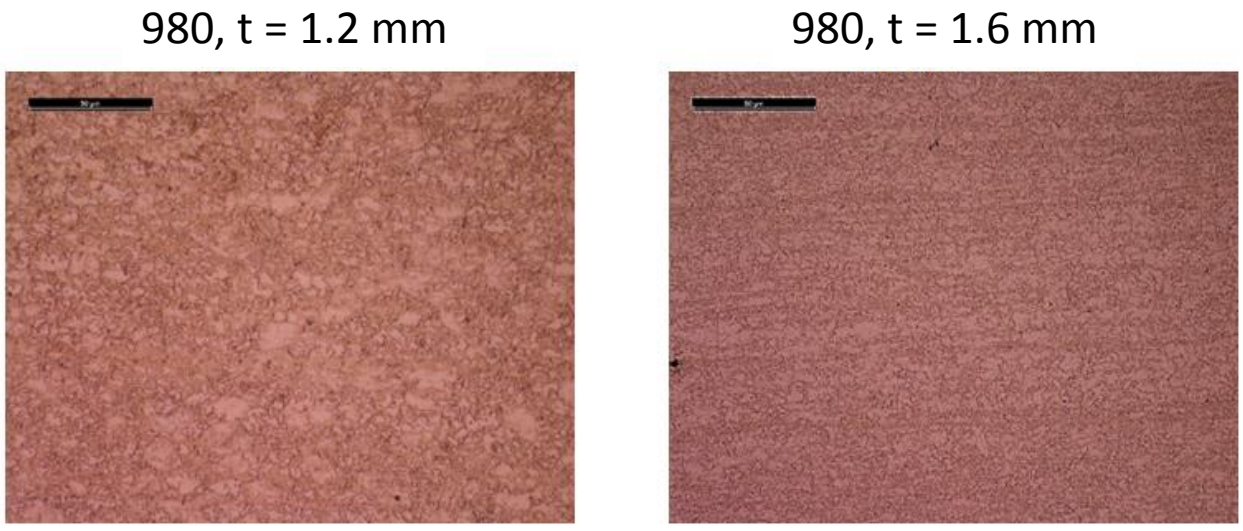

Figure 20 Microstructure of two DP980 materials obtained from different suppliers

Moreover, the AlSi coating on the HS1500 was removed in the gauge region of all test specimens prior to testing. The AlSi coating cracks at low strains which interferes with the DIC strain measurement and also creates uncertainty as to whether the coating or substrate is cracking.

In this study, most of the tests were performed with the principal straining direction aligned in the limiting direction with the lowest total elongation unless specified. The limiting direction for the steel was the transverse direction and the limiting direction for the aluminum alloy was the rolling direction. Detailed information about the test materials can be found in Table 1 and Figure 21. This material information was obtained from other projects at UW and different extensometer gauge lengths were used. Detailed material information can also be found from Kortenaar (2016), Zhumagulov *et al.* (2018), and Pathak (2018). The elongation data is provided for context but should not be used to compare between the materials due to gauge length differences. In addition to these main materials of interest, several materials such as ZEK100, DP and Boron steels in various conditions, and other aluminum alloys were also included in the analysis of the v-bend test to ensure a representative set of automotive materials were considered.

Table 1 Physical properties of main materials in this study. Note that the gauge length is not identical

Material	**DP600 (t=1.8 mm)**	**DP980 (t=1.2 mm)**	**DP980 (t=1.6 mm)**	**HS1500 (t=1.6 mm)**	**AA5182 (t=1.5 mm)**
Extensometer gauge length [mm]	25	50	50	12.5	50
Uniform Elongation	14.5%	7.6 %	6.2%	4.6%	20.1
Total Elongation	25.4%	13.5 %	12%	11%	25.7
Tensile Strength [MPa]	645	1067	998	1571	303
Yield Strength [MPa]	403	787	943	1096	146
Strength Coefficient, K [MPa]	1007	1392	1233	2187	N/A
Hardening Exponent, n	0.154	0.074	0.053	0.084	N/A

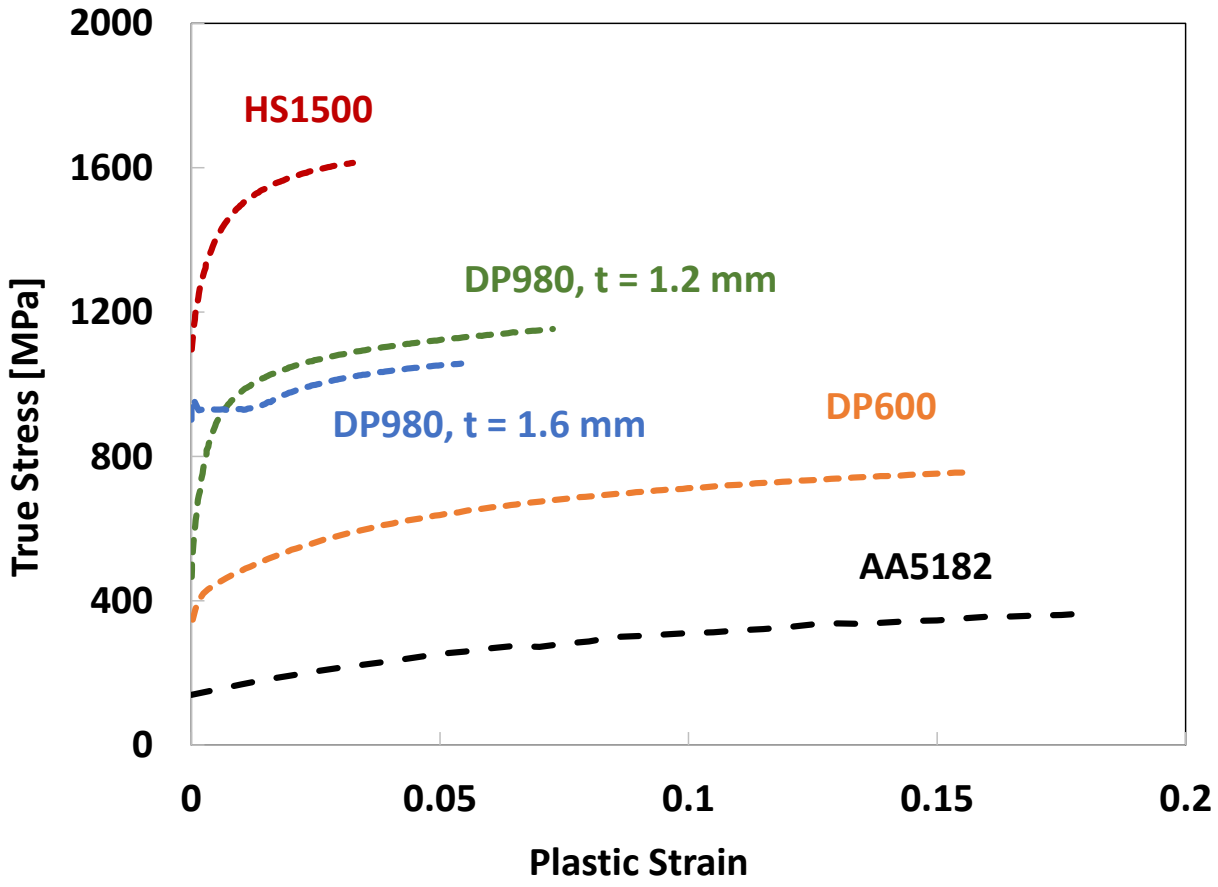

Figure 21 Equivalent stress response until the onset of necking for three advanced high strength steels and conventional aluminum alloy

The hardening behavior of DP980 with the thickness of 1.2 mm and AA5182 was investigated. The Hollomon's model also called "power law" was used for DP980. The hardening behavior of AA5182 was described by Jacqueline Noder at UW using a generalized Voce fit based on tensile and shear tests. It is important to note that the hardening exponent, *n*, is not constant for AA5182. The expressions of hardening models are as following, see also Figure 22.

$$\bar{\sigma}_{DP980} = K \cdot \varepsilon_p^{\,n} \qquad \bar{\sigma}_{AA5182} = a + (b + c \cdot \varepsilon_p) \cdot (1 - \exp(-d \cdot \varepsilon_p)) \tag{1}$$

where

K	*n*	*a*	*b*	*c*	*d*
1392	0.074	135.566	232.827	102.126	13.765

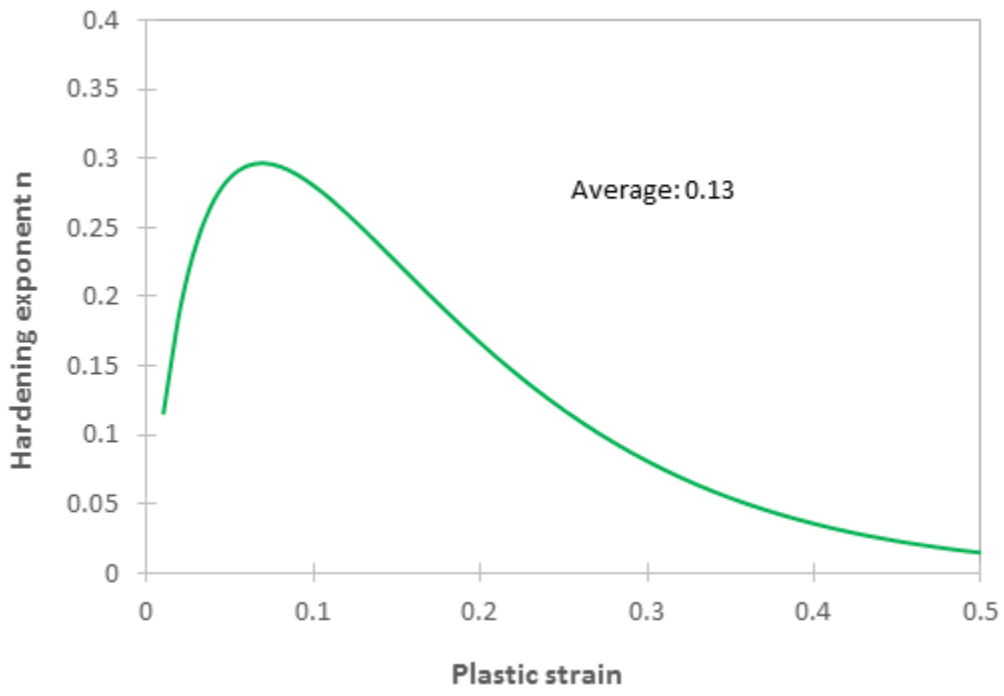

Figure 22 Evolving hardening exponent of AA5182 with deformation. The average hardening exponent until the onset of necking at a strain of 0.18 was 0.13. Tensile data provided by Jacqueline Noder (reference – private communication, 2019)

3.0 Equipment

In this chapter the general experimental setups will be described which are commonly used for various formability tests in the thesis. Relevant standards will be presented if applicable. Since this thesis involves the development of three different test fixtures, the detailed information regarding each formability test such as sample preparation, customized tool geometries, testing procedure, post-processing, and analysis techniques can be found in the relevant chapters.

3.1 Digital Image Correlation (DIC) Strain Measurement

As briefly mentioned earlier, the development of DIC has revolutionized the practice of forming limit characterization. The deformation history can be recorded with strain measurements obtained over the entire area of interest (AOI). All test setups used in the thesis employed stereoscopic DIC to capture deformation in 3D.

Strain measurement using DIC can be very sensitive to the settings used by analysts especially for test specimens that the deformation localizes into a small band prior to fracture. Aside from the image resolution which is fixed based upon the choice of lenses and test set-up, software settings such as the subset size, step size, and strain filter are selected by the analyst. In the present study, Vic-3D 7 DIC software from Correlated Solutions Inc. was used with a subset size ranging from 29 to 25, a step size of 5 and a filter size of 2 to 5 to obtain an approximate virtual strain gauge length (VSGL) of 0.5 mm. The VSGL combines the image resolution (mm/pixel), strain filter size (pixels) and the step size into an effective gauge length over which the strains are averaged. To evaluate the influence of the VSGL on the reported experimental failure strains, a parametric study was performed on the VDA bend test, the stretch bend test, and the miniature dome test using the DP980 with a various VSGL varying from 0.1 mm to 1.5 mm. The results are presented in Section 4.3.1, Section 5.1.1, and Section 6.2 for each test setup. The

VSGL provides a reasonable metric to ensure that consistent DIC settings are selected for various characterization tests in this study.

To assist the DIC to trace the surface deformation optically, all samples were painted with white primer, and black speckles were sprayed over the dried primer surface. These speckles were desired to be randomly patterned to obtain local uniqueness so DIC can easily track the local deformation especially during 3D analysis, see Figure 23. All painted specimens were tested within the same day to avoid potential confusion surrounding fracture identification due to the paint prematurely cracking prior to fracture of the test specimen. Materials with coatings such as hot stamped steels require the coating to be removed prior to speckling as coating failure will affect the DIC analysis as they decohere during deformation.

Figure 23 Randomized speckle patterns to help DIC for tracking of local deformation for a Nakazima dome test specimen. The optimal size of the speckle may vary depending on the test setup

3.2 MTS Formability Press

The Nakazima test station in the High-Pressure Lab at UW employs a hydraulic MTS formability press as shown in Figure 24 and Figure 25. Control of the dome test binder for clamping was done using an MTS 407 controller. A second 407 controller is installed to control the punch displacement independently. A custom LabView program is used to control the press. The punch force and displacement from the 407 controllers are synchronized with the DIC images through a DAQ. For detailed specification of the station, see Table 2.

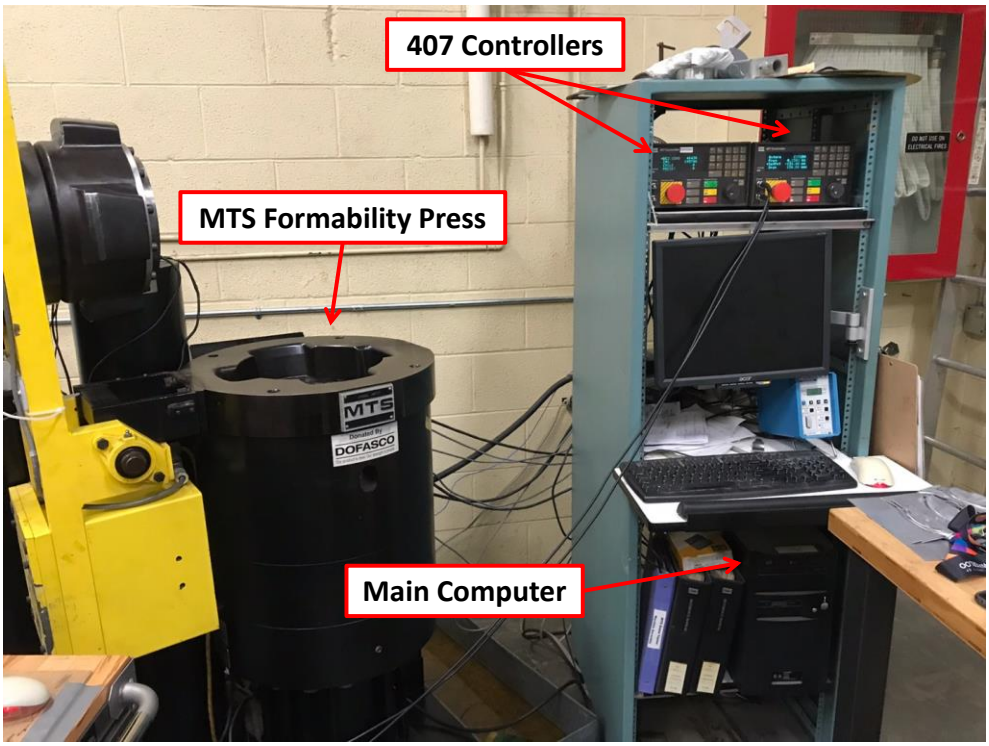

Figure 24 General layout of the MTS dome test station. The test procedure is controlled by the main computer

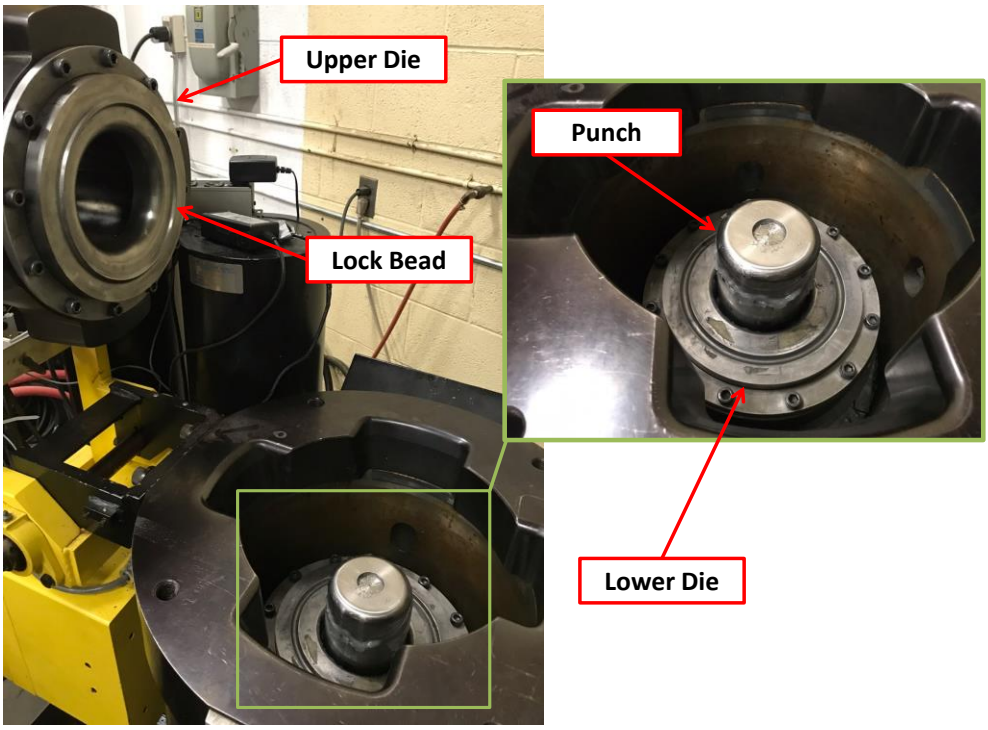

Figure 25 Inside of the MTS formability press with a cylindrical punch. The dies and punches are changeable. The die and the punch are controlled independently

Table 2 Specification of MTS formability press. All factors remain constant throughout the study except the type of punch. The hemispherical punch is for the LDH test, and the conical punch is for the hole expansion test. The stretch-bend test employed the wedge-shaped punch

Punch Type	Hemispherical, Conical, Wedge
Punch Diameter	101.60 mm
Die Opening Diameter	117.60 mm
Upper Die Diameter	117.60 mm
Lower Die Diameter	112.27 mm
Maximum Binding Force	640 kN
Lock Bead Diameter	177 mm
Lock Bead Depth	4.78 mm
Nominal Punch Speed	0.25 mm/s

The test procedure of Nakazima test can be briefly summarized as 1) Lubrication, 2) Specimen loading, 3) Binding, 4) Forming, 5) Termination, and 6) Specimen removal. These steps can also be applied to other tests such as the stretch-bend test and the hole expansion test with minor adjustment.

Three layers of Teflon sheet with Vaseline were placed on top of the punch as lubrication. A small and circular Teflon sheet can be applied additionally at the punch apex to help promote necking at the dome apex. Excessive surface friction due to poor lubrication may cause an off-centered crack, see Figure 26.

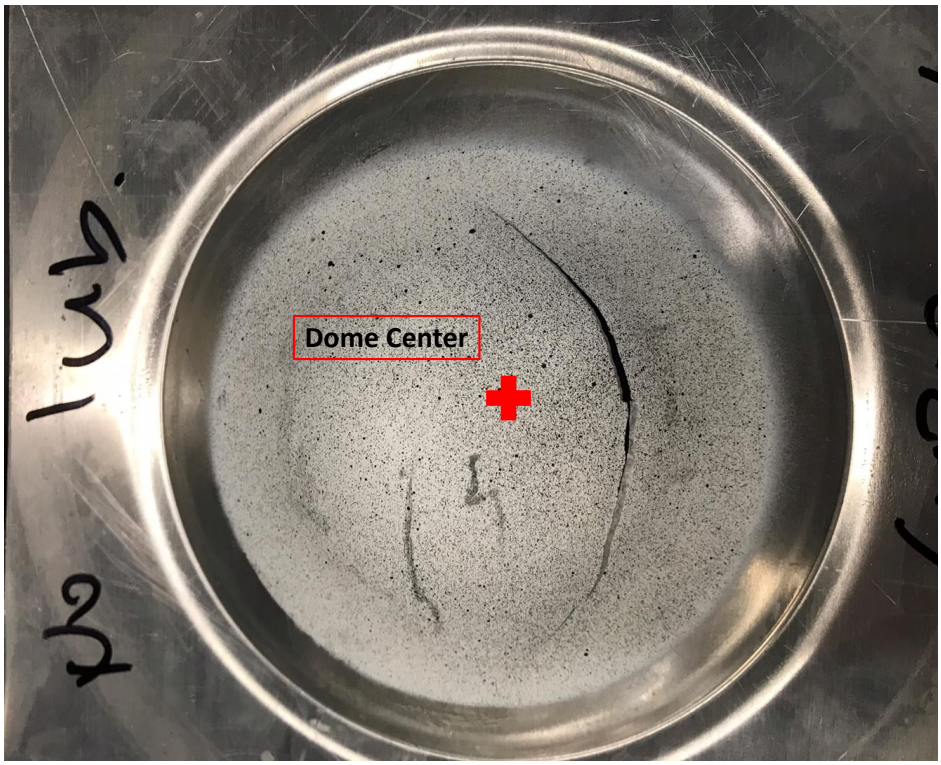

Figure 26 Equi-biaxial dome test specimen without proper lubrication. Off-centered crack often generates a rapid major strain development in a radial direction providing stress state similar to plane strain condition

Once the specimen was properly inserted, the bottom die clamped the specimen with a force of 640 kN. A circular lock bead was employed in this study to prevent any draw-in of the material. Die sets without a lockbead can also be used provided there is sufficient clamping force to mitigate material draw-in and obtain a fully clamped condition. After the closure of the die and the clamping load was reached, the punch was activated at a constant velocity of 0.25 mm/s. The DIC strain measurement system was activated manually and then the LabView program was activated to perform the test.

The test specimen geometry follows from the ISO 12004-2 standard that the specimen width is varied to alter the strain path. Each dogbone specimen has a straight section of 25 mm followed by a transitional radius of 20 mm. Specimen widths of 25.4 mm (1”) and 76.2 mm (3”) provide approximate strain paths

of uniaxial and plane strain tension, respectively. All dogbone-type test specimens were fabricated using EDM wire cutting or CNC machining to ensure a smooth edge condition to avoid fracture initiating at the edges. Since the equi-biaxial stretch condition is independent of sample orientation and the edge condition, a simple 203.2 mm by 203.2 mm (8”) square blank was sheared from the sheet, see Figure 27. Detailed sample geometries can be found in Figure 28.

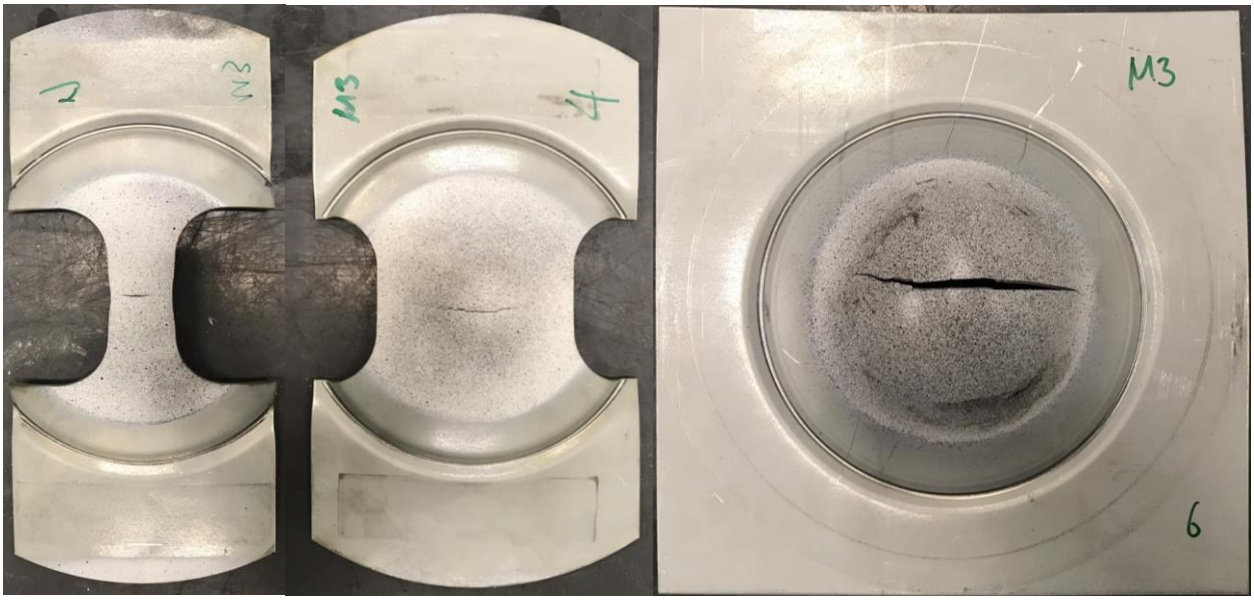

Figure 27 Fractured Nakazima test specimens of DP980 steel under uniaxial tension (left), plane strain tension (middle), and equi-biaxial tension (right)

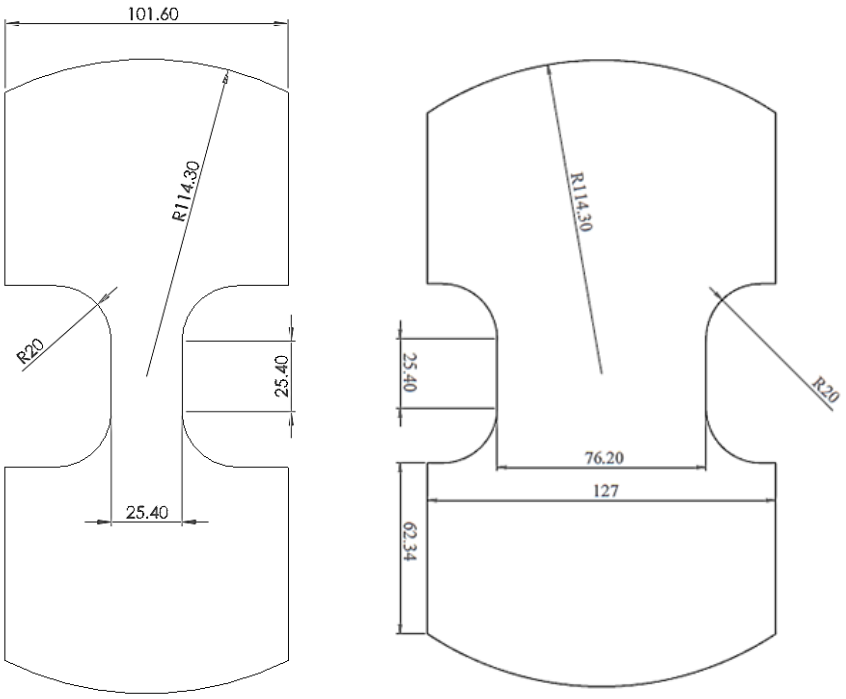

Figure 28 "dog-bone" shaped specimen from ISO 12004:2008 standard for Nakazima test: 1” width specimen (left) and 3” width specimen (right)

3.3 Development of Inverted VDA Bend Test Apparatus

The relatively simple setup of VDA238-100 bend test is only capable of providing limited data: punch load and displacement. The bend angle can be estimated by analytical formulas but highly theoretical. To address these limitations in the VDA test standard, a novel test frame was developed to enable *in-situ* strain measurement using digital image correlation (DIC).

The basic concept in designing a VDA compatible bend test with stereographic DIC is to invert the test so that the punch remains stationary and the rollers move downwards to perform the bending. The advantage of this re-configuration is two-fold: (1) DIC cameras can be easily positioned to view the outer bend and (2) the stationary punch ensures that the viewing area of the DIC does not move out of the plane so that DIC strain resolution is not compromised. To permit an enhanced viewing area for the DIC, the rollers were chamfered at 65˚ which leaves a sufficient arc length of the rollers to perform an 180˚ bend with

typical blank sizes before the chamfered section is reached, see Figure 29. Due to the sharp tip radius of the punches of 0.2 or 0.4 mm, they are often referred to as a knife.

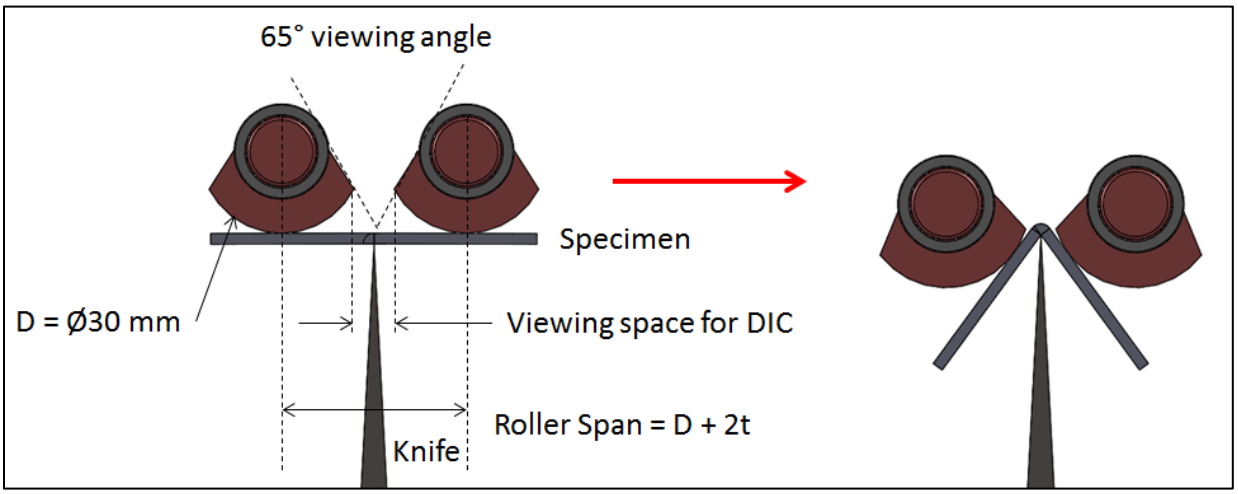

Figure 29 The concept for the tight radius three-point bending process with DIC strain measurement (Cheong *et al.* 2017)

Figure 30 and Figure 31 are cross-section views of the model perpendicular to the punch knife. The components that each roller attached can shift horizontally so the roller spacing can be adjusted based on sheet thickness in accordance with the VDA 238-100. Plastic spacers were 3D printed for each sheet thickness to enable consistent and accurate adjustment of the gap, see Figure 32. The roller components are then firmly locked with multiple bolts to prevent a change in the gap during the process. The influence of the roller spacing on the load response is shown in Figure 33. The load response was noticeably shifted downward by the larger gap. The VDA bend angle is identified based upon the peak load so a change in the gap can influence the result.

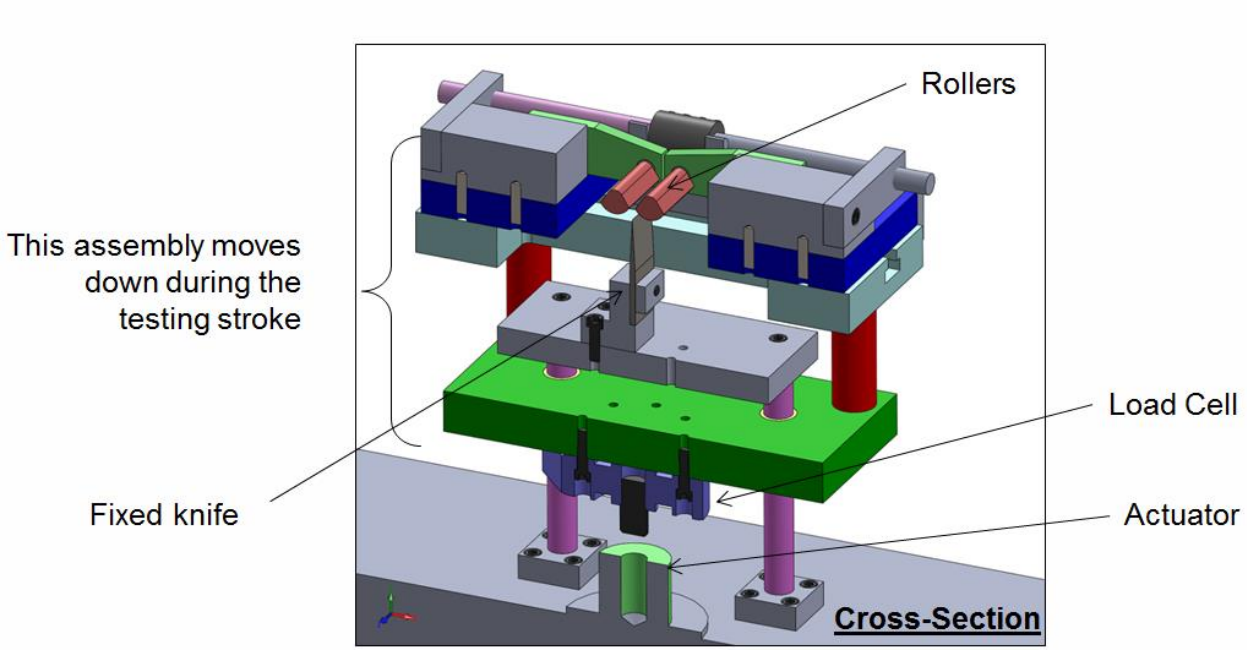

Figure 30 Cross-sectional view of the inverted v-bend device with DIC developed at the University of Waterloo

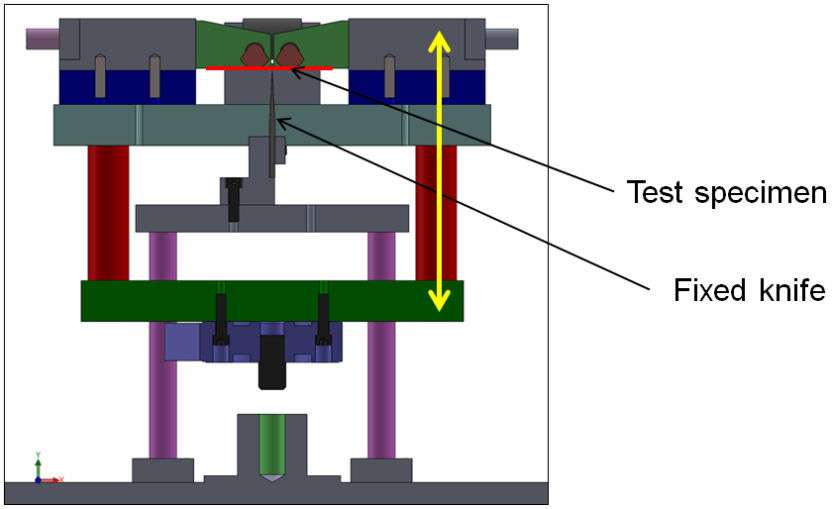

Figure 31 Forming stroke direction and the sample location during the process. The purple supports are stationary and the red supports move down during the stroke

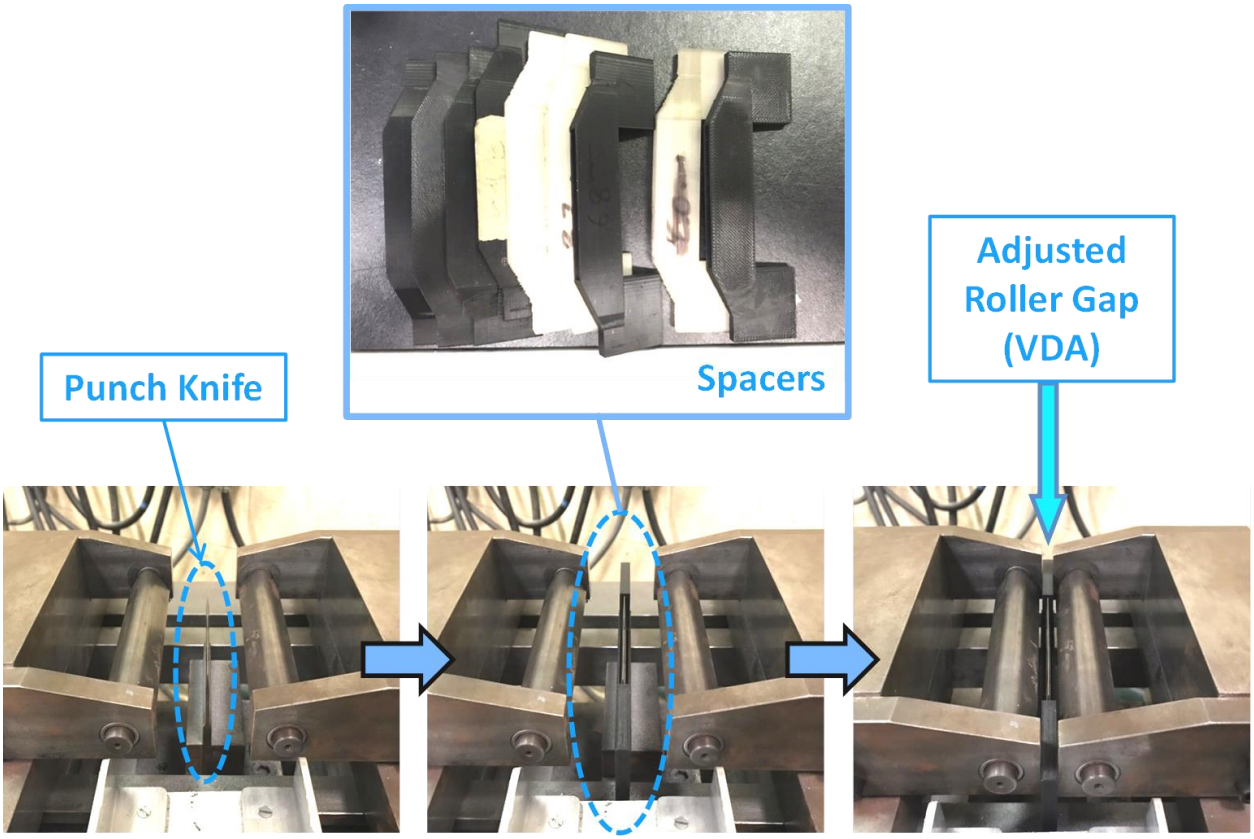

Figure 32 Adjustment of roller gap based on VDA 238-100 criterion using custom-made 3D printed spacers

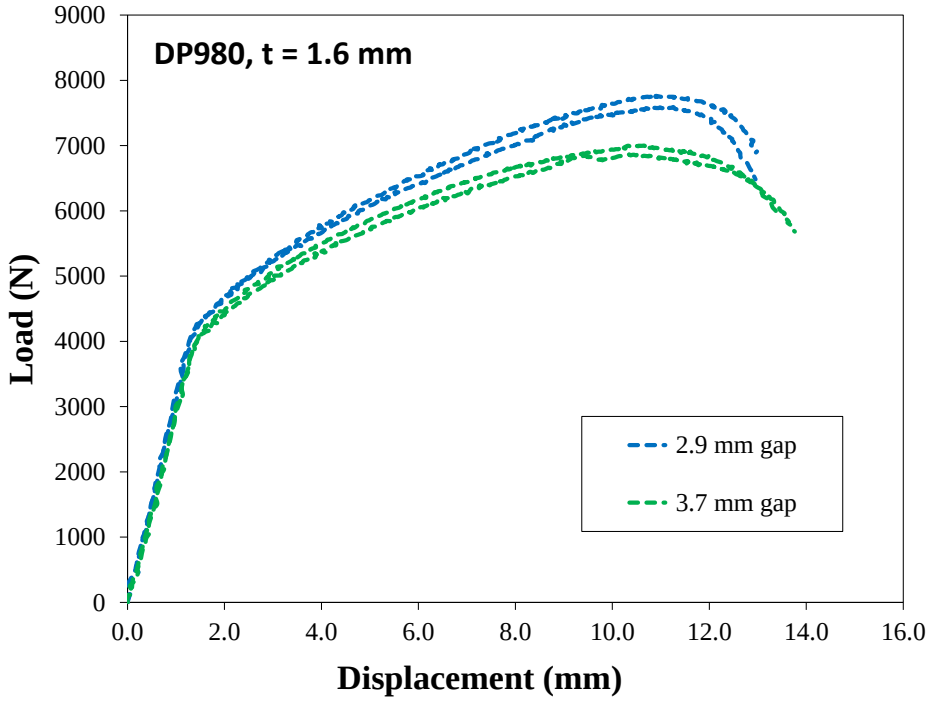

Figure 33 Influence of the gap on the load-displacement response in VDA bend test

Two DIC cameras using lenses with 17 mm focal length were installed on the v-bend test fixture that provided a resolution of 0.02 mm/pixel. The VDA 238-100 criterion states the sample width must be at least 20 times the thickness to promote plane strain bending. The test velocity of the rollers was 20 mm/min as prescribed by the VDA specification. The initiation and termination of punch stroke were controlled by an MTS 407 controller. The punch tip radius is either 0.2 mm or 0.4 mm depending on the thickness and material properties. The as-fabricated tip radii of punches used in this study were 0.21 mm and 0.43 mm. To avoid the potential for premature edge cracking in uniaxial tension during the test, all v-bend specimens were fabricated using either CNC or EDM for smooth edge condition.

The acquisition rate of the DIC cameras during the tests was set at 8-10 frames per second. In the v-bend tests, it was observed that crack propagation occurs relatively slowly since cracks form at the upper surface in tension and their growth is slowed by the compressive stress state through the thickness. Consequently, the VDA tests using DIC are not as sensitive to the DIC frame rate as in stretch-based tests such as Nakazima dome tests that rapid localization and fracture can occur in some materials.

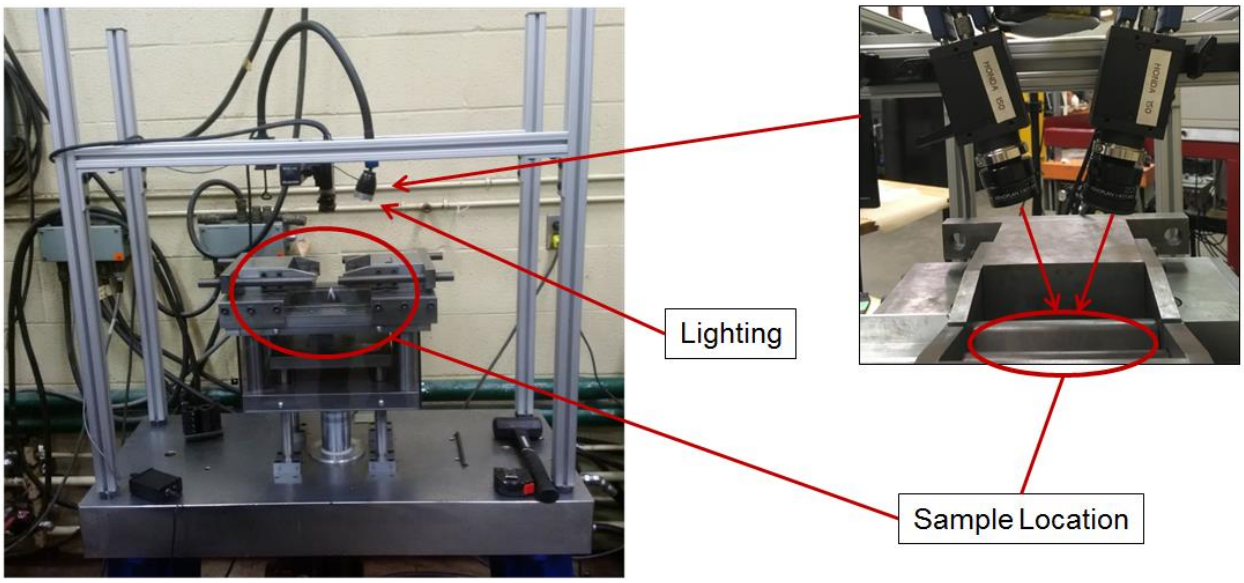

Figure 34 The inverted VDA238-100 bend test apparatus. Stereographical cameras and lighting are installed above the device

The VDA 238-100 specification provides a mathematical correlation between punch displacement and bend angle. The analytical expression of the bend angle, α, can be calculated based on the roller radius, R, sample thickness, a, punch displacement, S, and roller gap, L, see Figure 35. The sample orientation was determined based on the direction of the major strain. If the major strain direction is parallel to the rolling direction, as shown in Figure 35, the test was stated as "rolling direction (RD)" test.

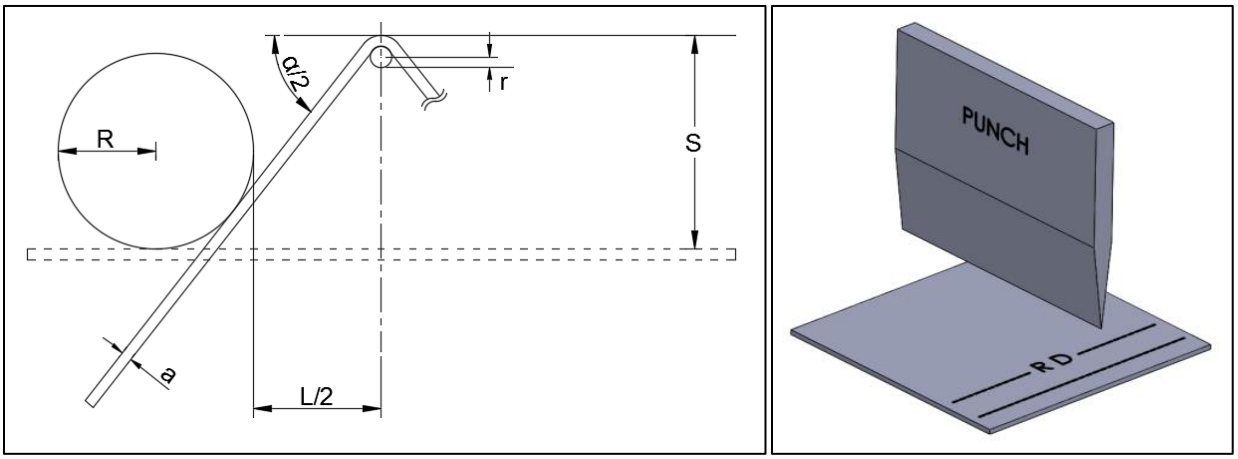

Figure 35 Schematic of the VDA bend test (left) and an example of rolling direction test orientation (right)

In addition to the VDA standardized punch tips, a punch with a 1.0 mm tip radius was also considered in this thesis to assess the influence of bending severity, see Figure 36. The termination criteria in the VDA 238-100 test is recommended to be after a decrease of 30 N or 60 N from the peak load as shown in Figure 37.

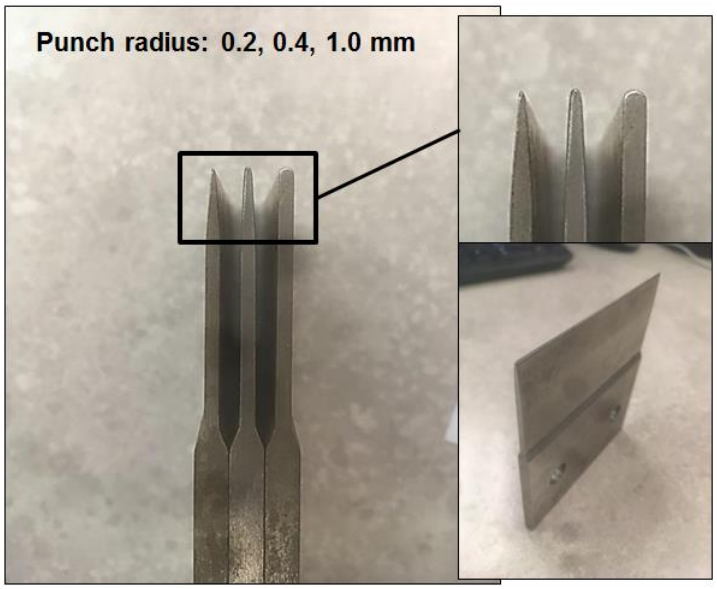

Figure 36 Punch, or knife, of the VDA bend test. The largest punch with the tip radius of 1.0 mm is an off-standard customized punch

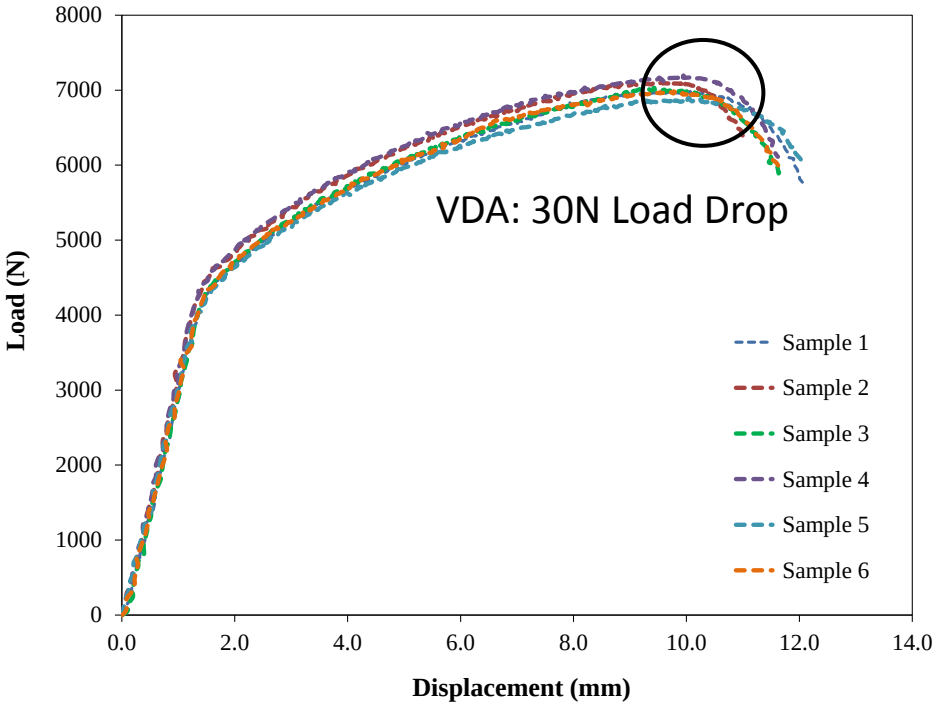

Figure 37 Load curve obtained from the VDA bend test using DP980 specimens. The material failure is dependent on the load drop from the peak load

The bend angle in the VDA test can be measured manually after the test but will be influenced by springback when the load is removed. The VDA specification instead recommends the use of the bend angle correlation to calculate the bend angle based upon the test geometry and punch displacement. The expression for the VDA bend angle is:

$$\alpha^{VDA}(R,a,L,S) = 2\left(-\tan^{-1}\left(\frac{1}{z}\sqrt{y^2-(z+x)^2}-(y-S)\right)\cdot\frac{180^\circ}{\pi}\right) \tag{2}$$

where

$$x = R + \frac{L}{2} \qquad y = R + a \qquad g = x^2 + (y-S)^2 \qquad z = \frac{-\sqrt{h^2 - 4g\cdot i} - h}{2g}$$

$$h = -2y^2\cdot x + 2x^3 + 2(y-S)^2\cdot x$$

$$i = y^4 - 2x^2y^2 - y^2\cdot(y-S)^2 + x^2\cdot(y-S)^2 + x^4$$

It is important to note that the above equation does not account for the punch tip radius in the bend angle calculation. Due to the inclusion of the larger 1.0 mm punch tip radius in this study, it was decided to also consider the bend angle correlation from ISO 7438 (2005) that explicitly accounts for the punch tip radius, *r*. An alternative form of the ISO bend correlation has been given by Larour *et al*. (2012) and is:

$$\alpha^{ISO}(R,a,L,S,r) = 2\left(\sin^{-1}\left(\frac{y+r}{\sqrt{(S-(y+r))^2+x^2}}\right)+\tan^{-1}\left(\frac{S-(y+r)}{x}\right)\right)\frac{180^\circ}{\pi} \tag{3}$$

4.0 VDA Bend Test Analysis

The addition of an optical measurement system on the VDA bend test at UW has enabled significant improvements in fracture characterization in severe 3-point bending. With the DIC analysis, the quality and quantity of information obtained from the test were markedly improved. However, the guideline from the VDA238-100 specification only considers conventional parameters based on punch load and displacement. Therefore, as a part of this thesis, the "best practices" and test methodology were developed to provide a guideline for analysis of VDA bend test result with optical DIC measurement. It is important to emphasize that the initial design and fabrication of the v-bend test frame was completed during the summer of 2016 prior to starting of thesis work in fall. The initial design and set-up of the frame was part of the lead-in activity for this thesis. All of the analysis and test procedures were developed as part of the thesis.

4.1 Post-processing and Data Extraction

Once the VDA bend test was performed, as introduced in Section 3.3, two types of raw data can be obtained: 1) analog data from the MTS 407 controller and 2) stereoscopic images from cameras using the VicSnap software. The analog data file contains various traditional parameters such as acquisition timing, load and punch displacement that can be used for theoretical bend angle calculation. DIC images require additional post-processing using the Vic-3D 7 3D software for surface analysis. See Section 3.1 for the DIC setting used for the analysis.

The initial DIC image and principal strain contours of the DP980 in the v-bend test prior to fracture are shown in Figure 38. The entire width of the specimen was captured within the area of interest (AOI). The stereo cameras viewed the outer surface of the bend that is in tension and the 3D image of the AOI is presented in Figure 39. What is remarkable is the high degree of uniformity in the deformation field across the width of the specimen. Each line slice in Figure 38 (top) consists of 200 points that creates a

strain distribution across the bend. Approximated length of line slices can be estimated with viewing space which is dependent on sample thickness; a 2 mm thick sample has a viewing space of roughly 8 mm, see Figure 29. The major strain distribution across the bend was extracted from five locations, as shown in Figure 38. Each location, or line slice, provided a nearly identical strain distribution as shown in Figure 40.

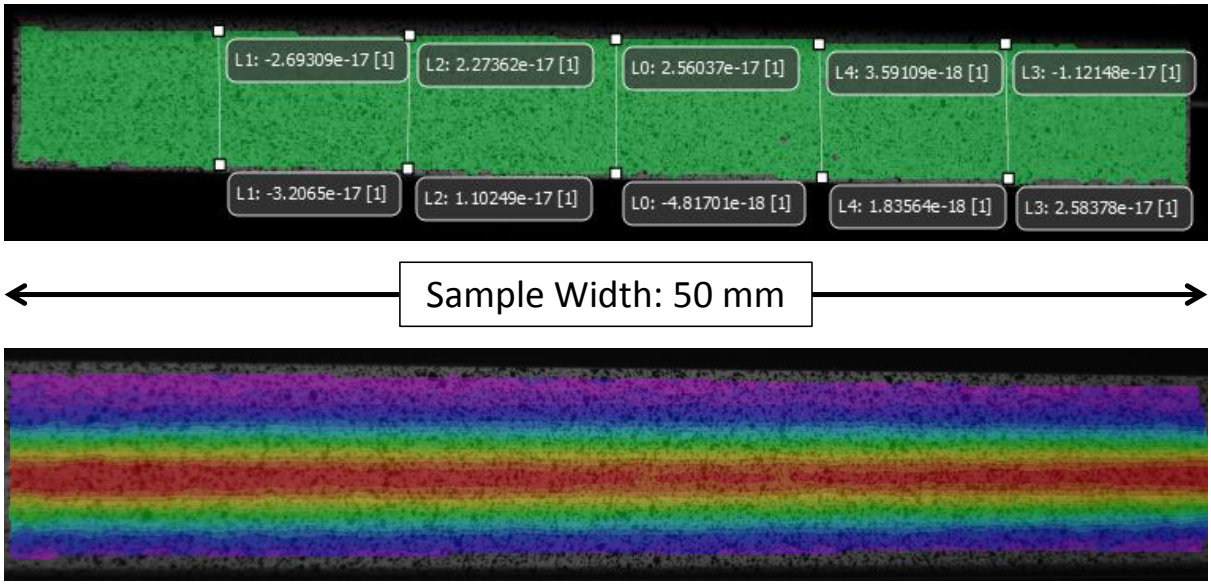

Figure 38 Initial (top) and deformed AOI (botton) of a DP980 specimen at the VDA load threshold. The width of the AOI is approximately 50 mm and the initial arc length (vertical lines) is 8 mm

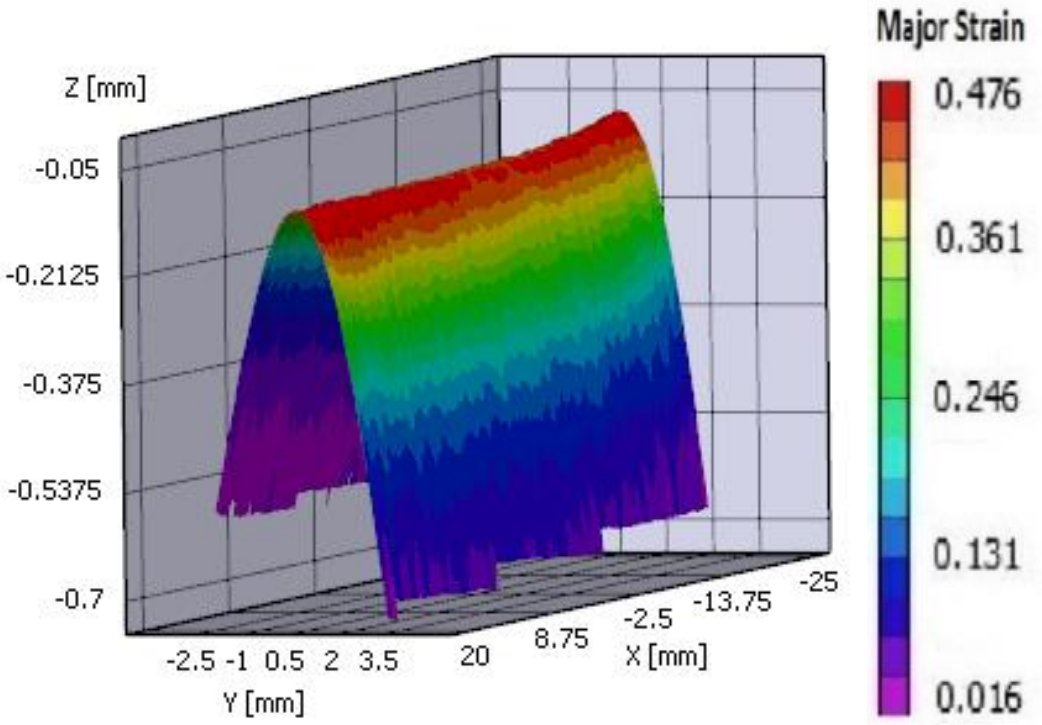

Figure 39 3D contour plot of the major strain distribution in the DP980 at the VDA load threshold

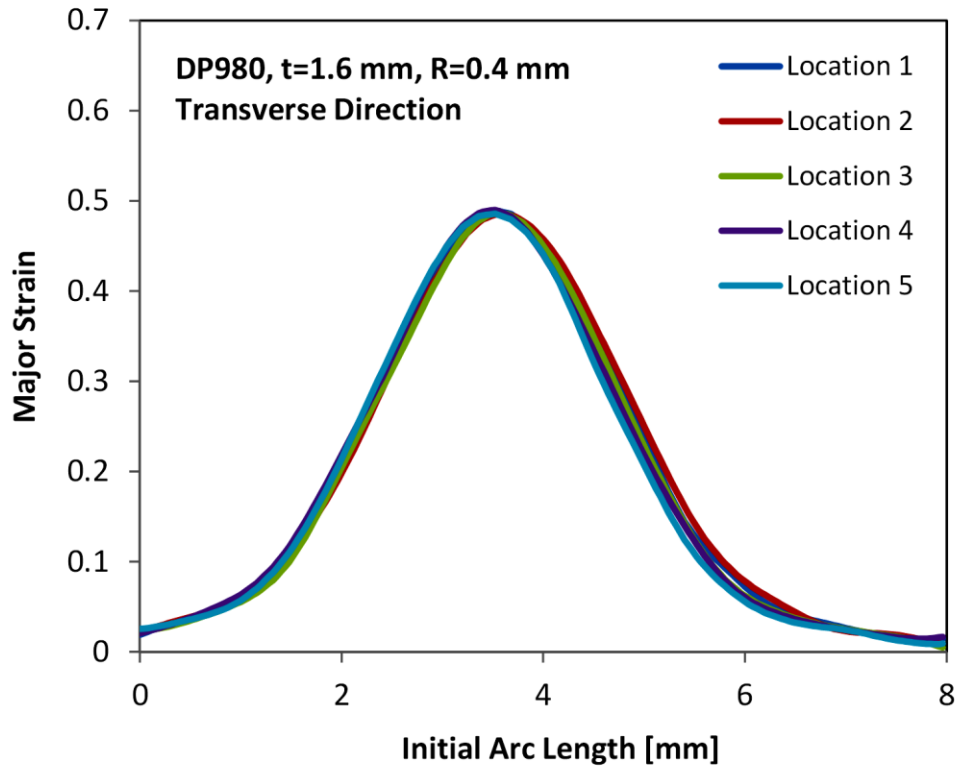

Figure 40 Major Strain distribution of DP980 from the five locations shown in Figure 38 (top)

Each data point usually contains locations (*x*, *y*, *z*), displacement (*u*, *v*, *w*), and strain measurement (major and minor), if needed, other information is also available such as curvature and strain rate. Each line slice consists of 200 data points that can be adjusted depending on the width of DIC viewing space. Moreover, the current study employs 5 line slices per image for analytical robustness and often 300~400 images are collected per each test. Therefore, the time history of line slices has an enormous number of data points which is almost impossible to be analyzed manually. To determine the fracture strain, a custom Matlab script was developed as part of this thesis to identify the locations of the peak strain of each of the five line slices. The script identifies the VDA load drop threshold from analog data and then locates the peak strain positions for each of the five line slices. The time histories of these five reference points are then averaged to provide a better estimation of the representative strain measurement. This method was based upon the techniques used in the ISO 12004-2 standard (2008) for determining the limit strains. A brief flowchart of the test for a single specimen is shown in Figure 41.

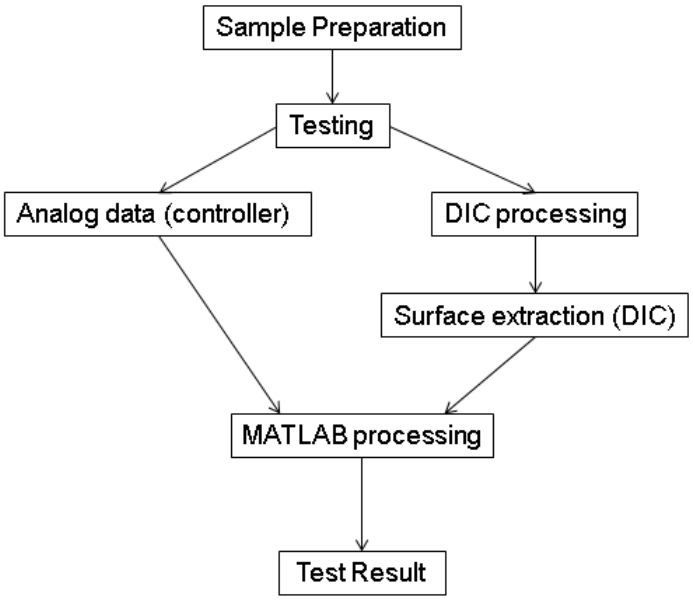

Figure 41 Process flowchart of VDA bend test. If more than one sample is tested, the entire step has to be repeated for each specimen

4.2 Evaluation of VDA238-100 Bend Test

The current VDA criteria such as load drop threshold and theoretical bend angle calculation were considered to be sufficient for traditional objectives of the test such as a comparison between other VDA bend test results. However, with the addition of the optical measuring system, the inverted VDA test frame was capable of providing information in more preferable form which is directly comparable with other formability tests. Even though this test setup was expected to clarify the analytical ambiguity by employing direct surface measurement, the verification and examination of the test robustness were mandatory. Therefore in this section, the traditional VDA guidelines were evaluated and compared with DIC optical measurements.

4.2.1 Fracture Identification

One of the main controversies in the field of fracture is how best to detect the onset of a crack. In the case of traditional stretch-dominant tests, this onset becomes obvious as abrupt propagation of the crack occurs due to unstable deformation within the neck. On the other hand, the strong through-thickness strain gradient from bending suppresses the onset of necking. As a result, the propagation of a crack becomes gradual and relatively slow. Determining the crack initiation moment that corresponds to a loss of structural integrity that is appropriate to define the fracture limit can be ambiguous and subjective. The VDA 238-100 criterion suggests terminating the test based upon a drop from the peak load of 30 N or 60 N depending on the material and sample thickness. This approach is reasonable from a theoretical perspective since if necking is suppressed by the severe bending, a load drop would be expected to coincide with the onset of material failure. Since the purpose of the conventional VDA 238-100 bend test is to rank material performance based upon the bend angle, using the peak load provides a consistent reference point for comparison. However, it is important to understand that this load threshold may not always correspond to the onset of crack initiation and that the load may decrease for large bend angles (135 degrees or higher) as the material loses contact with the rollers.

Since the new test setup heavily involves optical surface measurement, the current criterion based on the load threshold might not be sufficient. More local evidence of failure would be preferred such as defection of the surface. Therefore, a visual approach was performed and the result is introduced in this section to investigate the relationship between the traditional load threshold method and the onset of the actual fracture.

4.2.2 Visual Approach to Identify Crack

With the addition of DIC, the tests do not have to be terminated at the VDA load threshold since the data can be retrieved from the recorded test history. Therefore, samples were deformed until macroscopic cracks occur, as shown in Figure 42. The DIC images were then visually inspected to investigate the actual condition of the surface during the deformation. Under out-of-plane deformation, the presence of the strong strain gradient prevents the formation of necking. As a result, multiple cracks occur sporadically across the bend and then coalesce into macro-size cracks.

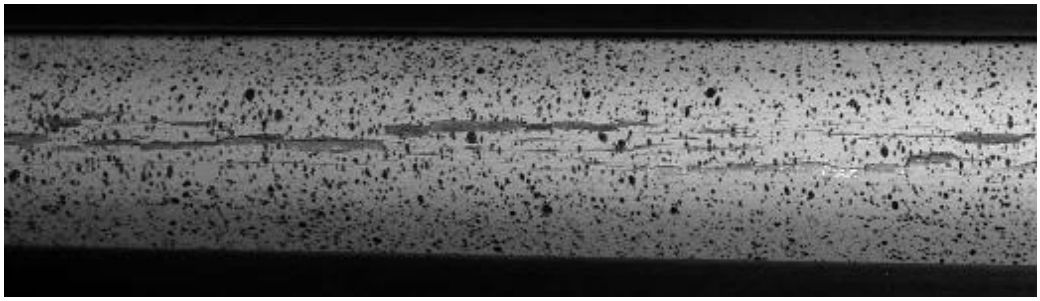

Figure 42 Deformed VDA bend test specimen (top view) with macro-size cracks across the width

A comparison of the load-displacement for the DP600 and DP980 is presented in Figure 43. Both materials experienced a clear and rapid load drop that the VDA load threshold point can be clearly identified. However at the VDA load threshold, the DP600 did not show any visible cracks on the surface whereas the DP980 experienced some surface cracking (see Figure 44 and Figure 45).

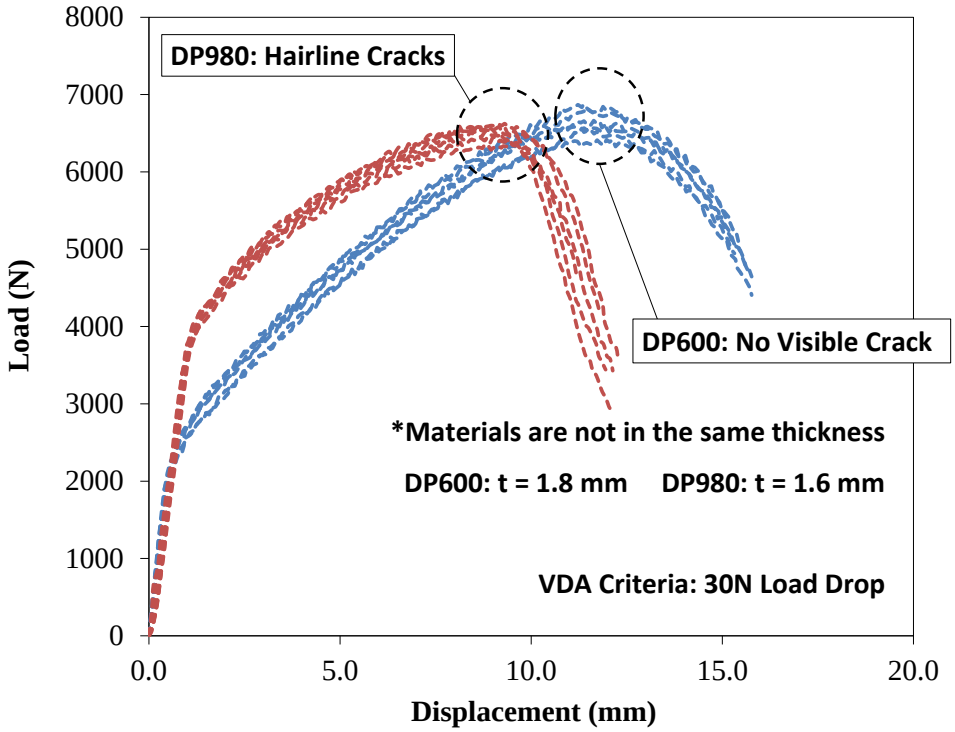

Figure 43 VDA load threshold point of DP600 and DP980 samples

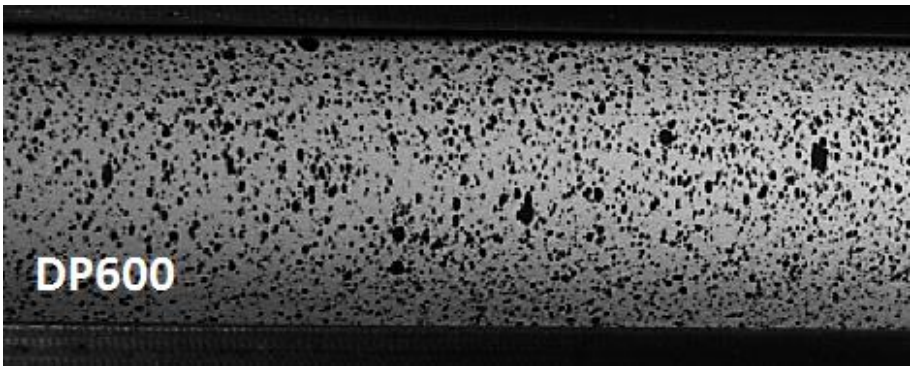

Figure 44 Deformed DP600 specimen at VDA load threshold. No visible crack was observed on the tensile surface

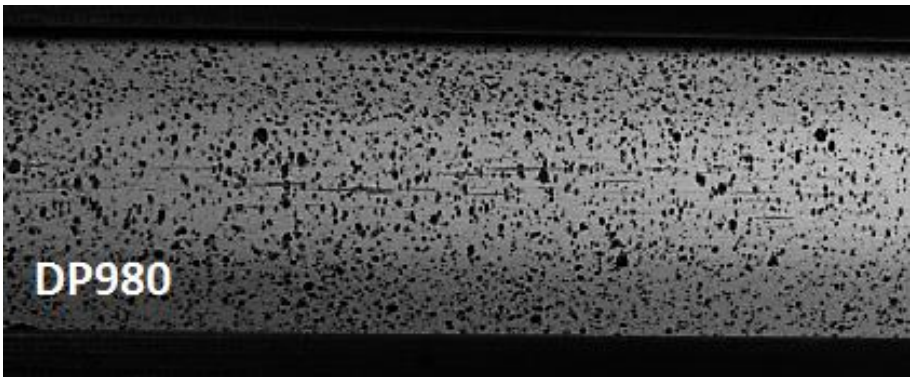

Figure 45 Deformed DP980 specimen at VDA load threshold. Multiple hairline cracks were observed on the tensile surface. These cracks are not due to paint failure and these same cracks continued to open up as part of the fracture process.

To investigate the definition of fracture, a visual inspection was performed throughout the process using the acquired DIC images. Visual crack detection can be subjective so upper and lower bound thresholds were established instead of choosing a unique moment. The lower bound was defined as the first initiation of a crack longer than 20 pixels, which corresponds to 0.4 mm from the setup resolution (Figure 46). This somewhat arbitrary value was selected as a reference to distinguish between the breakdown of the painted speckle pattern and the actual material cracking. The upper bound limit was more subjective and corresponds to seeing a fracture surface emerge as in Figure 46 when hairline crack begins to open. Note that the complete rupture of the specimen will occur past the upper bound and will be related to the crack propagation resistance of the material.

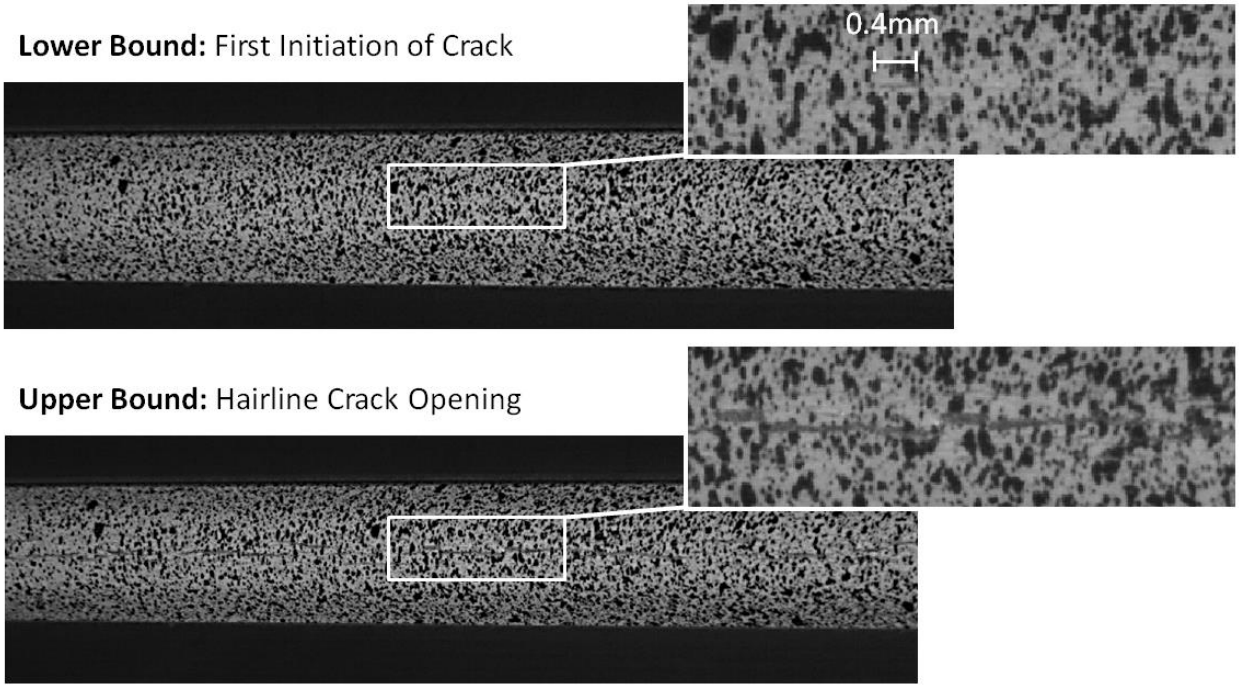

Figure 46 Example of the upper and lower bound of crack defined by the visual inspection

Three DP980 steels were provided from different steel suppliers for a comparison and characterization study. The sheet thicknesses of the materials were 1.2 mm, 1.4 mm, and 1.6 mm. These steels were tested in the rolling (RD) and transverse directions (TD), and the visual inspection results are shown in Figure 47. The comparison between the visual lower bound, VDA criterion, and the visual upper bound shows that, overall, the VDA method appears to be a reasonable initial estimation at least for the three variants of DP980 considered.

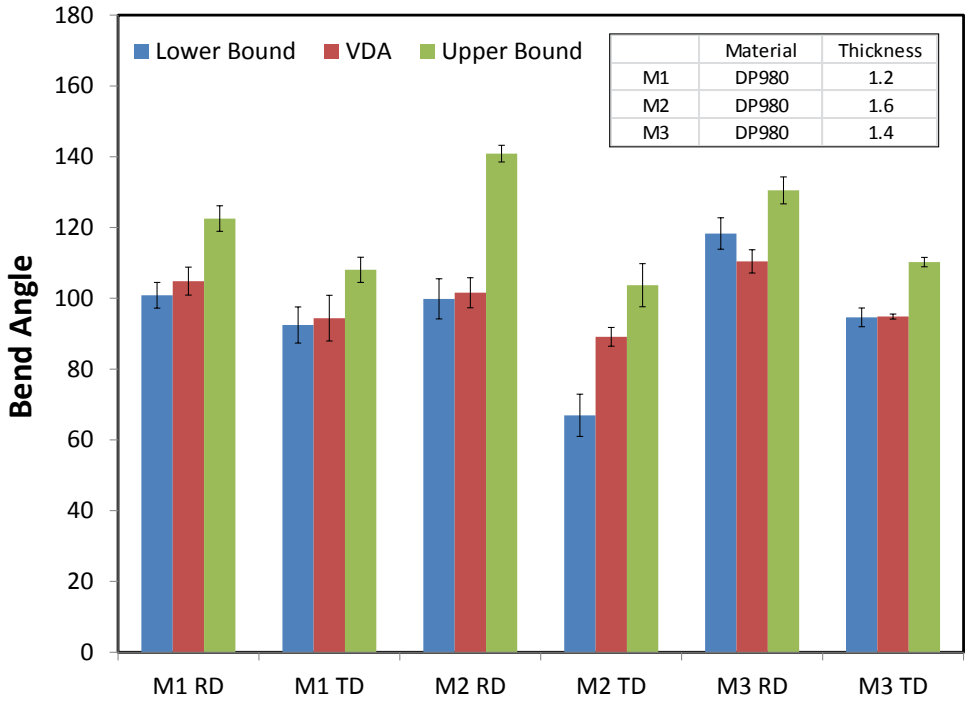

Figure 47 Visual determination of the crack using the upper bound, VDA load threshold, and the lower bound

The definition of cracking may also be dependent upon the desired application for the v-bend data. From a formability perspective, the onset of a hairline crack would denote a failed component as the surface has been compromised, thus the VDA estimate may become an upper bound. Conversely, from a crashworthiness perspective, complete cracking and rupture of the material might be preferred to identify the maximum amount of crash energy that can be absorbed by a structural component. In that case, the VDA criterion would likely constitute a lower bound estimate of the fracture limit.

Future work is required to refine the VDA failure criterion to detect the onset of cracking since visual identification of cracking can be subjective. For the remainder of this thesis, the VDA load threshold and the visual inspection of the onset of the crack will be adopted to report the failure strains while recognizing it may be imperfect and should be interpreted based upon the application of the material such as forming or crash.

4.2.3 Theoretical and Experimental Bend Angle

The VDA 238-100 specification and ISO 7438 standard are two common guidelines in the field of bendability analysis. Both provide analytical expressions for the bend angle based on punch displacement and test geometry. These equations were already introduced and can be found in Section 3.3, see Eq. (2) and Eq. (3). A noticeable difference between two theoretical formulas is that the VDA criterion uses a pre-determined punch tip radius, based upon the sheet thickness and material properties, whereas the ISO standard includes the punch radius in the formula.

Since the ISO and VDA formulas for the bend angle rely on mathematical calculations based on the punch displacement and test geometry, experimental errors are inevitable. Larour *et al*. (2013) demonstrated the sensitivity of these formulas to factors such as the machine stiffness, sheet curvature, punch tip lift off, and roller shift. To revisit the comparison between the different bend angle definitions with the DIC test results, the bend angles at fracture for the 17 conditions of materials listed in Table 3 were manually measured using a digital protractor. The considered materials are dual phase steels with different strength and thicknesses, TRIP steel, and various hot-stamped boron-alloy steels (Usibor® 1500-AS) quenched in air, oil, water, or using a die. An additional quench condition was performed in tooling at 400°C to provide a more ductile variant of the hot stamped material. Moreover, AA5182 was also considered as a representative of ductile aluminum alloy and a rare-earth alloy, magnesium ZEK100, was also investigated.

Table 3 Specimen types and testing conditions (total of 17 different conditions)

Material	Thickness	Direction	NOTE:
DP600	1.5	RD	DQ: Die quenched AC: Air cooled OQ: Oil quenched WQ: Water quenched RD: Rolling direction TD: Transverse direction DD: Diagonal direction Punch Radius = 0.43 mm
DP980	1.2/1.6/1.4	RD/TD	
Trip780	1.5	RD	
Usibor1500_DQ400	1.25	RD	
Usibor1500_DQ	1.22	RD	
Usibor1500_AC	1.22	RD	
Usibor1500_OQ	1.22	RD	
Usibor1500_WQ	1.22	RD	
AA5182-O	1.5	RD	
ZEK100-O	1.5	RD/TD/DD	

Measuring the angle of the samples that exhibited partial surface cracking was to minimize the influence of springback on the measurements since macro-level cracking will relieve the significant amount of the internal stress that is otherwise relieved by springback. Some level of springback will still be present in this study but was not quantified. For consistency, the last image recorded by the DIC system was analyzed as this coincided with the end of the test but before unloading of the specimen. The comparison results are presented in Figure 48. Overall, for the 17 material conditions evaluated, the VDA bend angle from Eq. (2) performed slightly better than the ISO bend angle from Eq. (3) which tends to overestimate the bend angle as the angle gets larger. This observation agrees with the study of Neuhaus *et al*. (2013) who also reported the better performance of the VDA correlation by using an optical measurement of the bend angle. The preference for agreement with the VDA over the ISO bend angle may also be related to the machine stiffness and the design of the inverted tooling which was developed based on the VDA criterion.

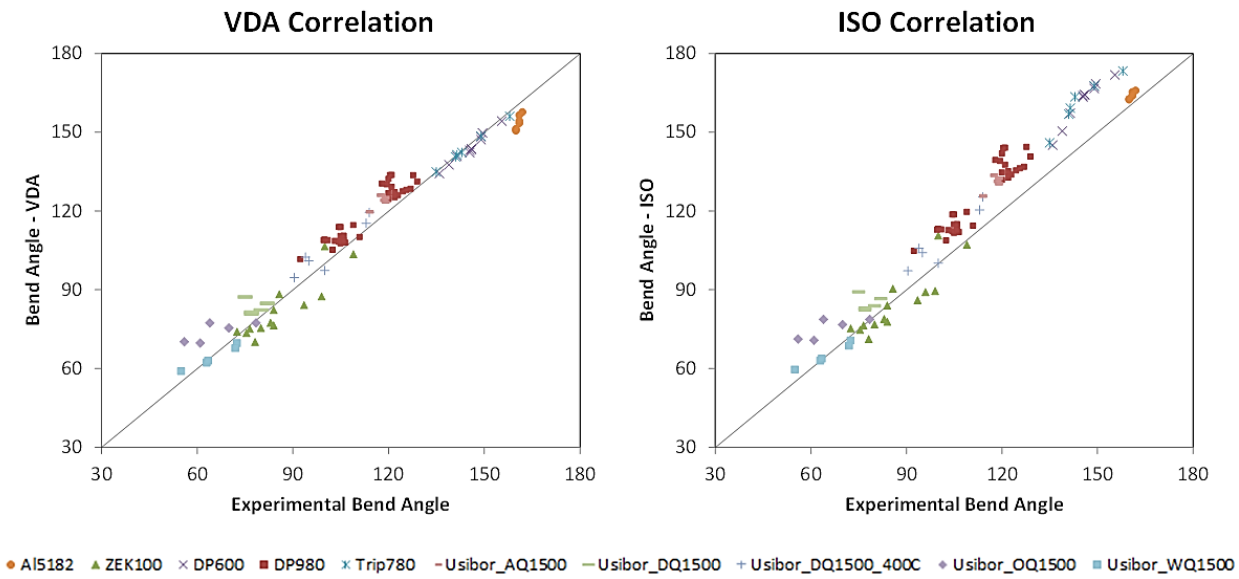

Figure 48 Comparison between the theoretical bend angle estimation and the manually measured experimental bend angle at fracture. ISO correlation (right) tends to overshoot the bend angle with large bend angle whereas VDA correlation (left) maintains its accuracy

4.2.4 Bend Angle Estimation using DIC

Analytical approach to estimate the bend angle was performed using the stereographic DIC data that the displacement of the region of interest can be retrieved. The bend specimen has a round tip at the fracture location thus extension lines have to be drawn to evaluate the bend angle, see Figure 19. The automated measurement of the bend angle using this data is not straightforward since the specimen is rounded and only a portion of the bend is visible. To mimic the physical measurement method using a protractor, a best fit linear line was drawn for each side of the bend and the intersection of the lines can define the bend angle, see Figure 49.

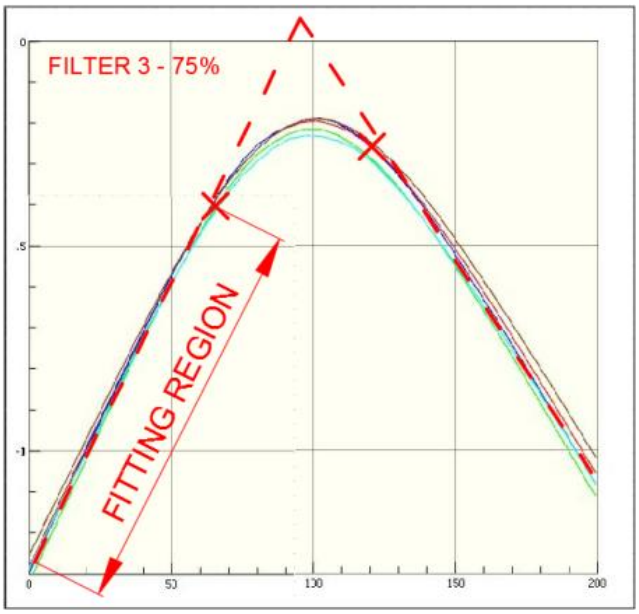

Figure 49 z-axis location of the bend from DIC measurement. Extension lines which are not necessarily symmetric are drawn to find the angle of intersection

However, due to the rounding of the sample in the area of interest, a selection criterion was needed to identify the points that are sufficiently far enough away from the bend apex where the strain is highest similar as shown in Figure 50. The proposed algorithm involved selecting the points based upon their relative strain level. If a point had a strain level of a specific threshold lower than the peak strain, it was included in the fitting region. The four threshold levels were 90%, 75%, 50%, and 25% as their strain filters.

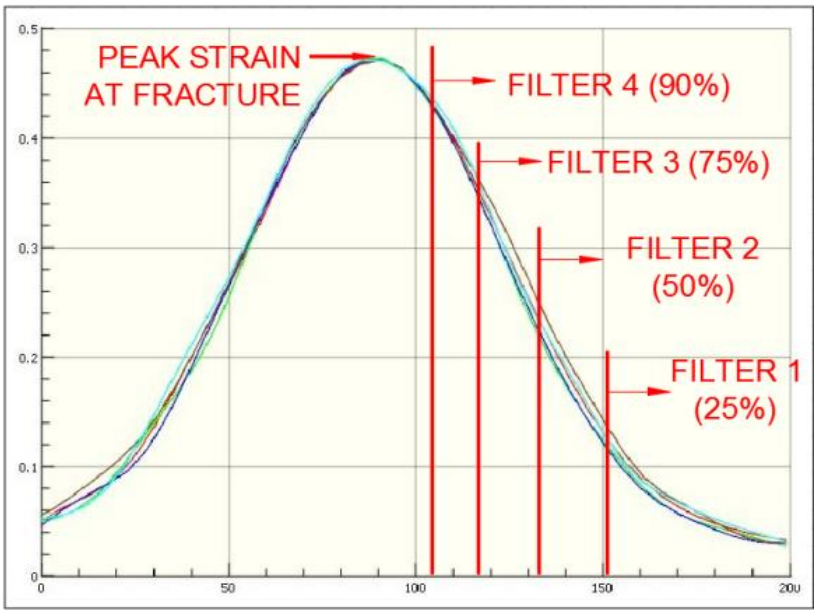

Figure 50 Filtering criterion based on the peak strain measurement. Four filters are selected based on the strain level of 90, 75, 50, and 25% of the peak strain

The performance of each filter was evaluated and compared by considering the coefficient of determination regarding the VDA bend angle correlation which can be calculated by

$$R^2 = 1 - \sum_{i=1}^{n} \frac{(\alpha_{DIC,i} - \alpha_{VDA,i})^2}{(\alpha_{DIC,i} - \alpha_{VDA,average})^2} \quad (4)$$

As shown in Table 4 and Figure 51, it can be observed that as fewer data points are included, the correlation becomes stronger. The best result was obtained using the strain filter of 25% with the DIC measured bend angle being in fair agreement with the bend angle from the VDA correlation. However, the reported accuracy was unfortunately not superior to the theoretical correlations. Due to the variability in the bend angle and the small viewing area in the DIC, it was decided to report all bend angles based upon the theoretical correlations from the VDA and ISO standards. Moreover, reporting of the bend angle using the VDA and ISO correlations, although imperfect, was also preferred by the industrial sponsors of this project to allow for comparison with existing VDA data provided from material producers. Consequently, improvement of the bend angle measurement using DIC was left for future work.

Table 4 Coefficient of determination corresponding to each filter. As fewer data points included, the correlation becomes stronger

	Filter 1	Filter 2	Filter 3	Filter 4
R^2	0.78	0.64	0.42	0.30

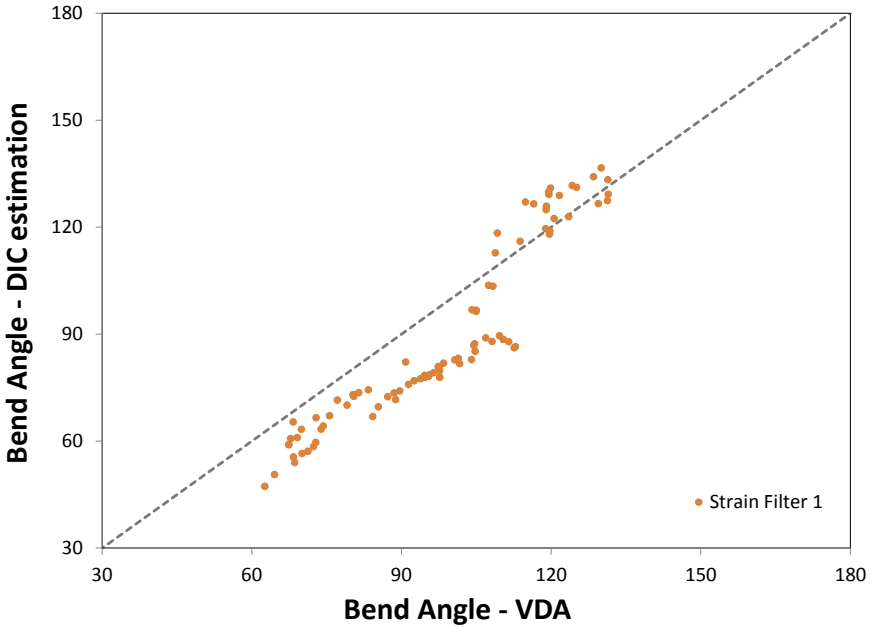

Figure 51 Comparison between the DIC measured bend angle with filter 1 and the estimated bend angle using the VDA correlation

4.3 Experimental Result of VDA Bend Test

In this section, experimental observations and data analysis using DIC post-processing will be presented. DP600, DP980, and HS1500 were selected to be the test materials for in-depth analysis using the VDA bend test. All tests were performed under identical testing conditions, and repeated observations will be introduced using representative test results.

4.3.1 VSGL study of VDA Bend Test

The concept of virtual strain gauge length (VSGL) is an emerging metric in the field of DIC to quantify the level of detail in post-processing. A sensitivity analysis of VSGL was performed prior to the further investigation to determine suitable parameters to be used for the current v-bend setup.

The major principal strain distribution over the outer surface of the VDA bend test is presented in Figure 52. It can be seen that the larger VSGL tends to smooth the curve by averaging a large number of data points thus underestimates peak strain. The failure strain appeared to be converging at 0.3 mm VSGL. The difference between the peak major strain from 0.2 mm VSGL and 0.3 mm VSGL was smaller than 0.5%. However, the VSGL of 0.5 mm was selected as a compromise between accuracy and computational efficiency with an error of less than 2% but required half of the processing time relative to the convergence VSGL of 0.3 mm.

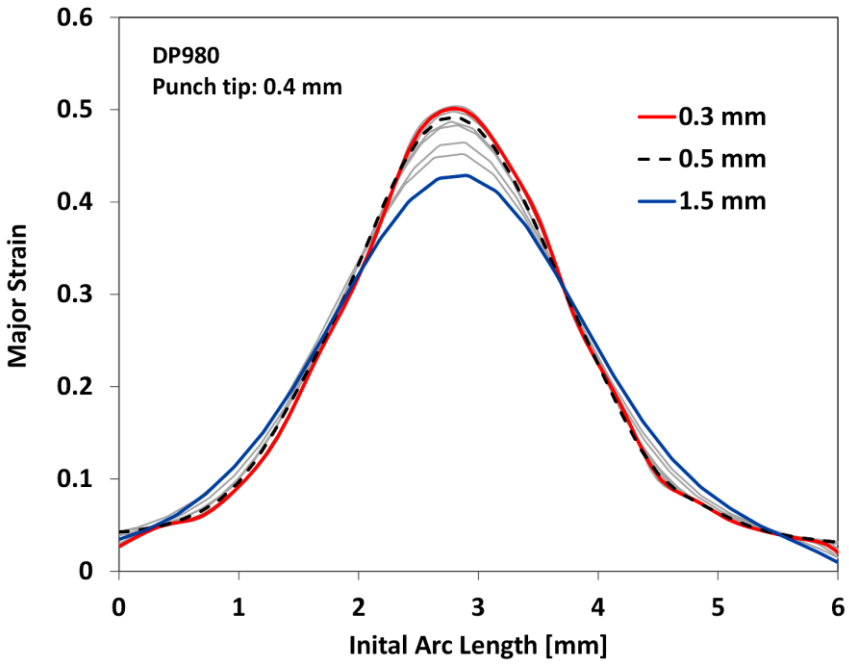

Figure 52 Influence of the VSGL on the major strain distribution in a DP980 specimen. The stain distribution was obtained from the image at the VDA load threshold. Initial arc length was oriented perpendicular to the punch knife

The VSGL analysis was repeated for the DP600 and HS1500 samples with similar results to the DP980. The major strains at failure for the three steel sheets for a VSGL of 0.3 and 0.5 mm are presented in Table 5. It can be seen that there is a negligible variation within the strain measurements to two decimal places.

Table 5 Major true strain of bend test at VDA load threshold using 0.3 mm and 0.5 mm VSGL

VSGL	Major Strain at VDA Threshold		
	DP600	DP980	HS1500
0.3 mm	0.47	0.50	0.29
0.5 mm	0.47	0.49	0.28

4.3.2 Experimental Observation

The surface measurement obtained by DIC analysis verified that the bending condition of VDA bend test is under plane strain condition as desired with a negligible width strain. A homogenous major strain distribution was observed across the width and the minor strain (width strain) was effectively zero, see Figure 53. Five DIC line slices were introduced, as shown in Figure 38, to obtain a representative strain measurement.

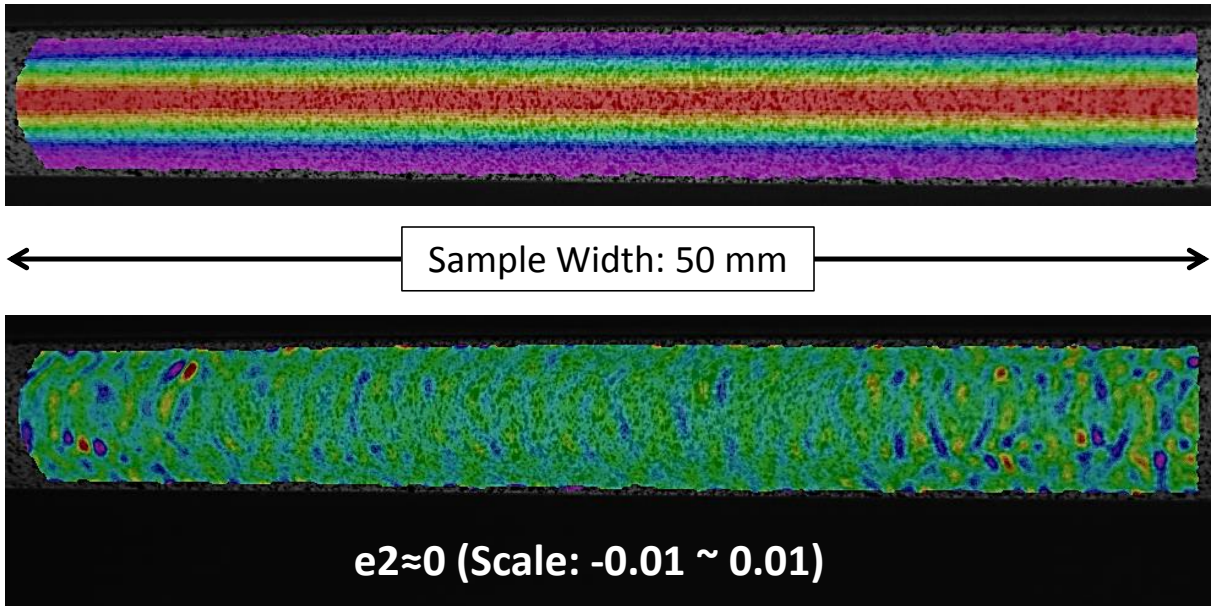

Figure 53 Major (top) and minor strain distribution (bottom) of the tensile surface. No deformation was observed in width direction as the process was under plane strain condition

The load curve from the test of DP980 specimens is presented in Figure 54. The first thing to notice is that the VDA bend test was very repeatable. The importance of load stability must be emphasized in this test setup since the reference point for data extraction of the entire analysis was dictated by the load

threshold. This reference point was determined by 30 N load drop from the peak load as suggested by VDA criterion, see Figure 54.

The general shape of the load curve is somewhat similar to the engineering stress-strain curve. In the initial bending stage, a linear and rapid load increase was observed until a yielding point where the non-linear load increase starts to occur. This initial bending stage is when the sample wraps around the punch and does not involve with significant surface deformation, see Figure 55. The non-linear load increase continues until the peak load point where the VDA load threshold is determined, and then a rapid drop of the load occurs as the surface crack is developed and propagates.

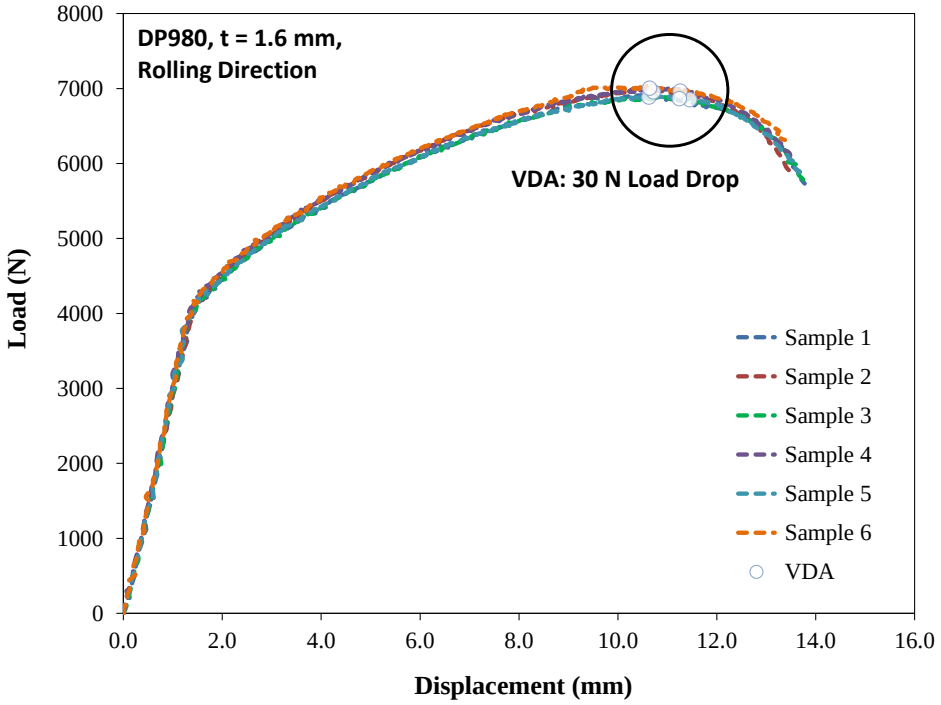

Figure 54 Load and punch displacement obtained from the MTS 407 controller using DP980 specimen. VDA load threshold was determined by the peak load point

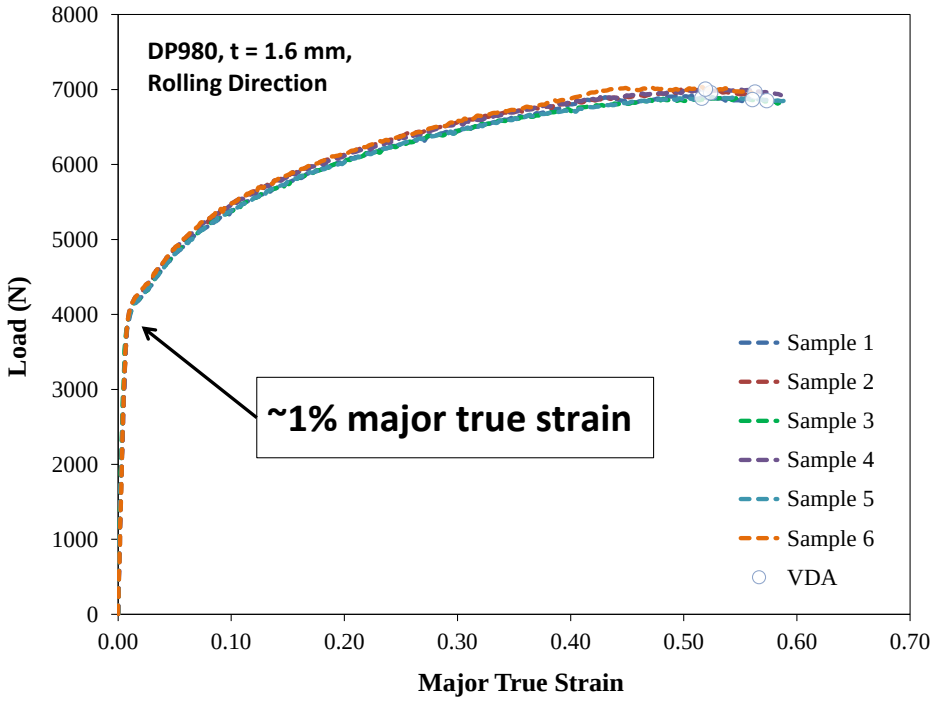

Figure 55 Relationship between the load and the major true strain of DP980 specimen

The principal strain histories of DP600, DP980 and HS1500 steels are presented in Table 6 and Figure 56. It is clear from Figure 56 that the VDA bend test provided a proportional strain path of plane strain tension until cracking. Perhaps most important is that the width strain (minor strain) is effectively zero throughout the process indicating that a proportional plane strain loading condition was obtained.

Table 6 Fracture limit under pure bending based on VDA bend test. The fracture is defined by VDA load threshold (30 N load drop from peak load), and the bend angle was calculated using both VDA and ISO correlations

Material	DP600		DP980		HS1500	
Major Strain, ε1	0.48	±0.03	0.46	±0.03	0.27	±0.01
Minor Strain, ε2	0.00	±0.00	0.00	±0.00	0.00	±0.00
VDA Bend Angle, θ_{VDA} [°]	108	± 4	82	± 3	52	± 2
ISO Bend Angle, θ_{ISO} [°]	112	± 4	84	± 3	52	± 2

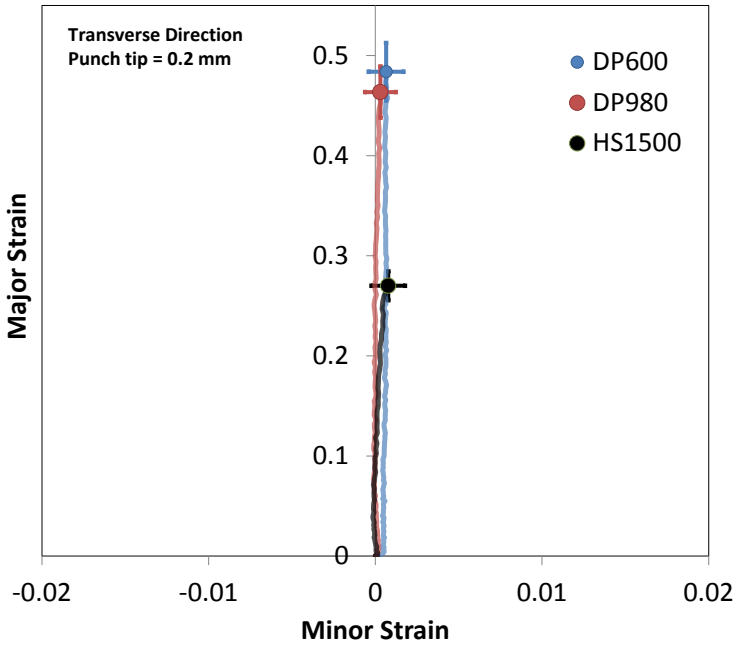

Figure 56 Evolution of the principal strains in the V-bend tests of the three steels using a punch tip radius of 0.2 mm

The relationship between the bend angle and the major strain is shown in Figure 57 and Figure 58. The major strain evolution during bending had a common behavior and can be described by three main components: the exponential region, the transition point, and the linear region. The relatively slow and non-linear strain development in the early stage of bending was accelerated as the specimen was deformed around the punch radius. The bending process eventually became stable thus the major strain development showed a linear growth until the VDA fracture limit. Durrenberger and Dietsch (2018) have reported a similar observation and described the bending behavior using the slope of the linear region and the x-intercept of an extension line from the linear region. It is important to understand that the fracture bend angle and the development of surface strain can be subjective and dependant on material and test condition. The idea of relating the material property to the slope of strain development will be discussed further in Section 4.4.1 with the concept of bend angle normalization.

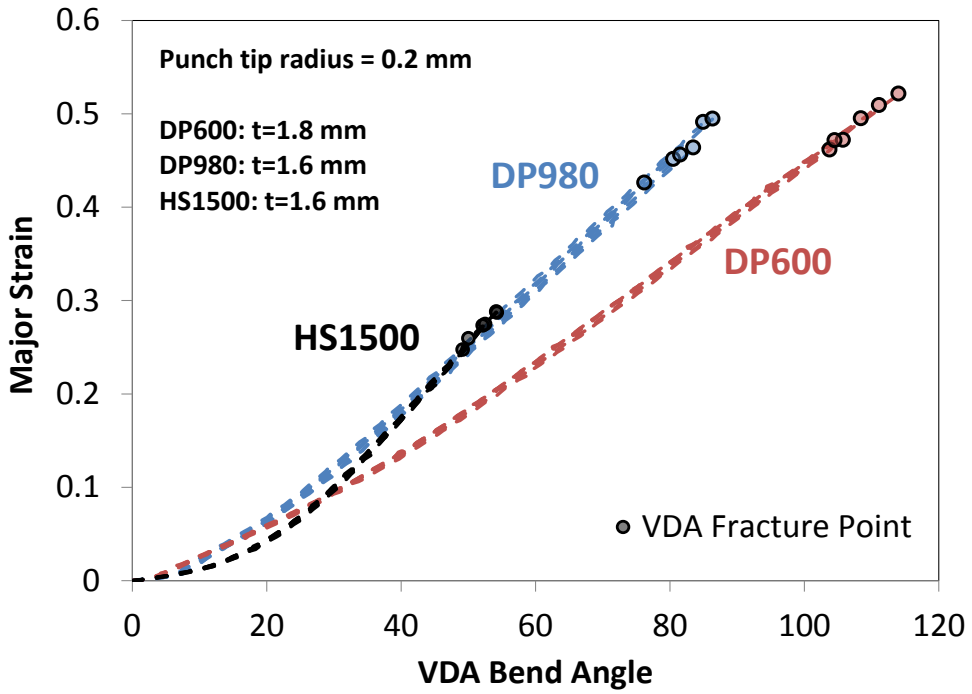

Figure 57 Major strain evolution of three AHSS plane strain specimen using the v-bend tests. Tests were done in the transverse direction with six repeats

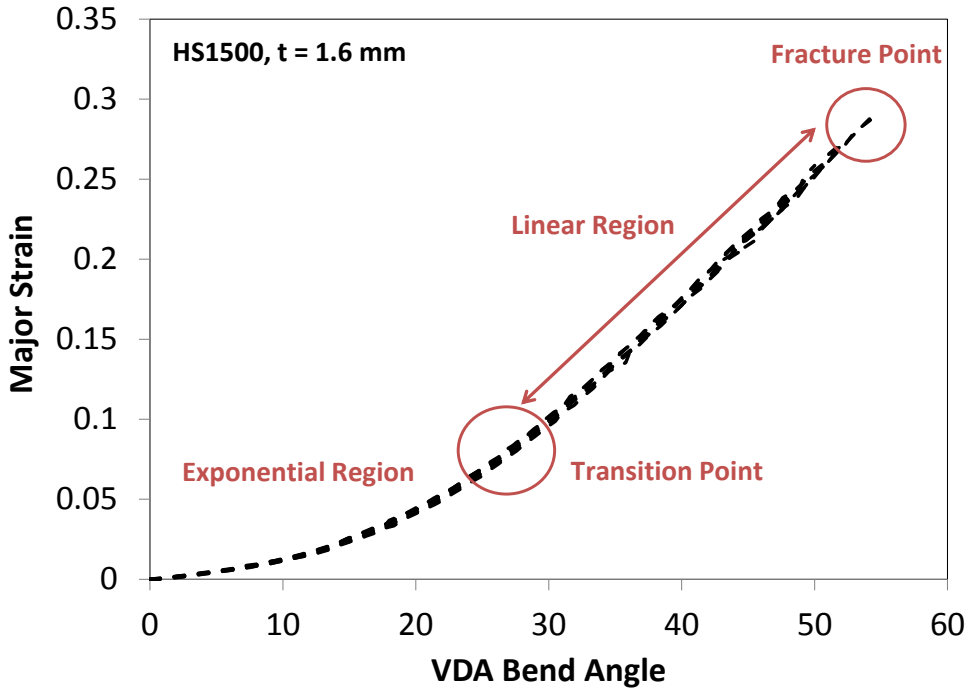

Figure 58 Typical strain development under pure bending test using 0.4 mm punch radius (HS1500 specimen)

4.3.3 Comparison with the Traditional In-Plane Test Result

Forming limit strains are defined as the onset of acute necking so that the mitigation of necking shifts the forming limit toward the fracture limit. In the case of pure bending, during which necking cannot develop, the concept of a forming limit becomes meaningless and the fracture limit becomes the effective forming limit. The difference is presented in Table 7 and Figure 59. The result was remarkable as the plane strain bending fracture limit from the v-bend test reached a major strain of about 0.50 whereas the plane strain forming limit under in-plane stretching was only 0.13. This significant difference directly highlights the importance of developing an advanced material characterization method accounting for the different stress-states.

Table 7 Forming limit strain of DP980 sample after deformed by two plane strain tests. Nakazima plane strain test was performed using the punch with 50 mm radius and the limit strain was identified using the ISO 12004-2 method

Forming Limit	Nakazima Dome		V-Bend	
Major Strain	0.12	±0.02	0.50	±0.02
Minor Strain	0.02	±0.00	0.00	±0.00

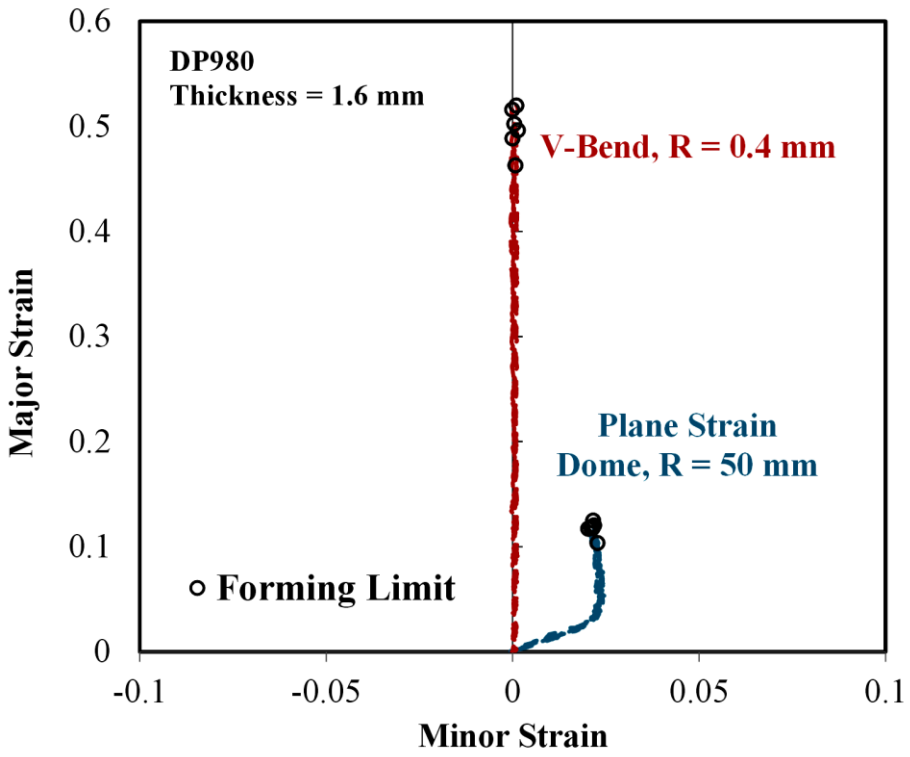

Figure 59 Strain evolution of DP980 plane strain specimens using the v-bend and Nakazima dome tests. Six repeated tests were performed for each geometry. The limit strain for the Nakazima test was obtained using ISO 12004-2

Moreover, another significant disagreement was observed from the fracture strain under plane strain condition. In Figure 60, the purple and light blue data points represent the fracture limit from the VDA bend test and plane strain notch test respectively. The plane strain notch test was performed by Dr. Abedini at UW as part of the industrial project. It was observed that the DP980 performed remarkably better with VDA bend tester even though both tests had nearly identical strain-state. This observation is counter-intuitive since the fracture limit is thought to be the material constant thus it should be independent of test condition as long as the stress-state does not change.

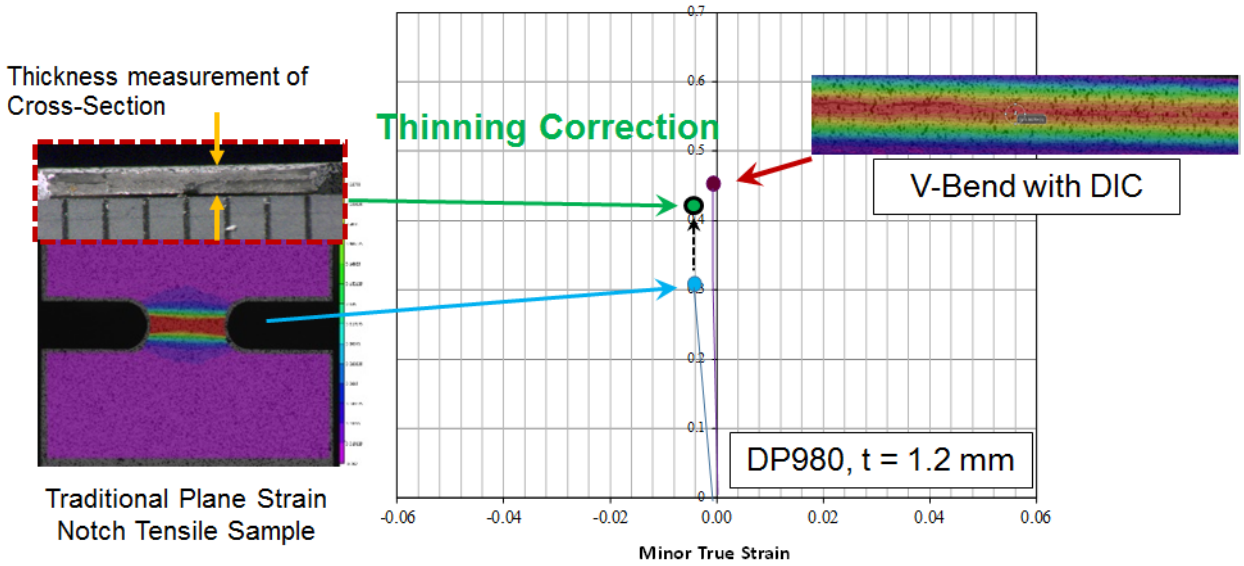

Figure 60 Comparison of plane strain fracture limits of DP980 using VDA bend test (purple), plane strain notch test (light blue), and plane strain notch test with the thinning correction (green)

Gorji *et al.* (2016) recognized this phenomenon and stated that the DIC might not be a reliable method to measure fracture strain since the rapid thinning at the fracture onset can introduce a significant error to DIC from calculating accurate strain measurement. Instead, an alternative method to measure the fracture strain was proposed by Gorji *et al.* based upon post-mortem thickness measurements of the fracture location. A similar approach was employed in this project to correct the DIC strain measurement based on the final thickness. The fractured notch test specimens were sent to Honda Research America (HRA) to measure the local thickness at fracture using an optical microscope and it was found that these post-mortem fracture strains compared closely with the v-bend results in this thesis. The fracture strain from the post-mortem thickness is presented in Figure 60 as a green data point. Similarly, this comparison was repeated using two additional DP980 sheets with different chemistries and thicknesses, see Figure 61. The result seems that the thinning correction can effectively improve the accuracy of the fracture limit estimation of in-plane stretching test. However, due to its ease of testing, stability and ideal loading condition, the VDA bend test is considered to be the optimal test method for plane strain fracture characterization.

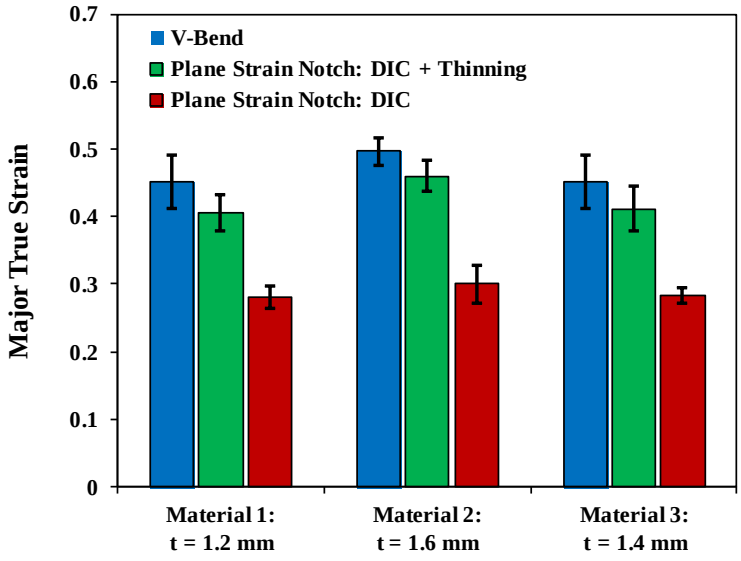

Figure 61 Summary chart of fracture limit from VDA bend test and plane strain notch test using various DP980 samples with and without thinning correction

4.4 Effect of Bend Severity, t/R

With the addition of the DIC system, it is important to understand the relationship between the bend angle and the major strain. The mechanics of bending will largely control the relationship between the major strain and bend angle but is expected to have some deviations due to the complexities of plastic bending and material behavior such as hardening rate. The VDA238-100 specification used throughout the automotive industry is only based upon the bend angle at the peak load. Although bend angles are intuitive and are easy to visualize when comparing materials, they depend upon the sheet thickness and bend radius unlike a strain measurement. As will be demonstrated in the subsequent sections, the fracture limit in plane strain is a fixed material property, but the bend angle will vary based upon the thickness and punch radius and is a non-unique metric for characterizing materials. The influence of the sample thickness and the bend radius can be described as a bend severity, often expressed as a ratio, *t/R*.

4.4.1 Bend Angle Normalization

As the bend severity can significantly alter the major strain development, a direct comparison between materials tested under different bend severity is questionable. However, bend angles are intuitive and are still preferred within industry to compare materials. To bypass the complexity of obtaining materials with specific thicknesses and fabricating a large number of punches with different tip radii, a theoretical approach was considered to eliminate the effect of bend severity from the strain measurement. An expression to normalize the measured major strain from the DIC system was developed using the maximum normal strain based on the punch geometry. The study of Wang *et al*. (1993) suggested that the radius corresponding to the position of the neutral axis of a specimen in tight radius bending can be estimated as

$$R_{Neutral} = \sqrt{R_{outer} R_{inner}} \qquad R_{outer} = R_{inner} + t \tag{5}$$

For simplicity, the inner bend radius was approximated by the punch tip radius which will be reasonable for moderate to large bend angles provided there is no lift-off from the punch. Thinning was also assumed to be negligible but does occur to some extent, especially at larger bend angles. Laurour *et al.* (2013) have reported that a noticeable amount of thinning occurred at large bend angle, as shown in Figure 62. That study also reported that almost no thinning was observed at the tangent to the side of the punch, as shown in Figure 62 thus the thinning of the sheet does not have significant effect on the bend angle calculation.

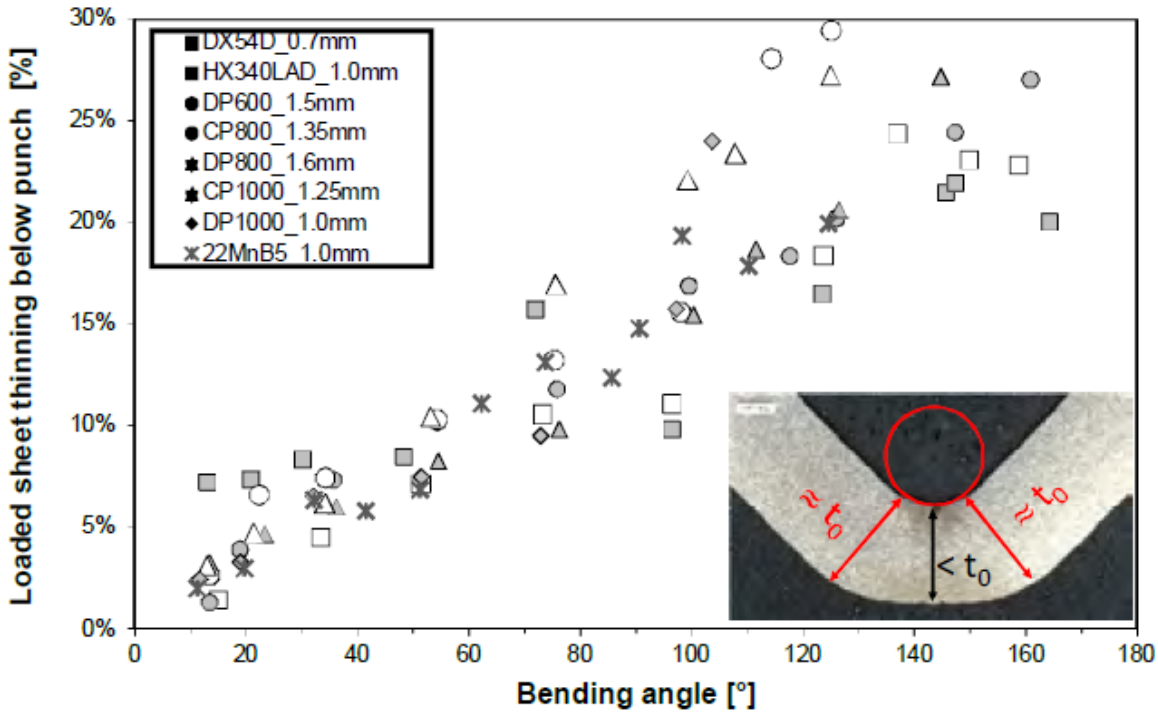

Figure 62 Thinning of a steel sheet at large bend angle reported by Laurour *et al.* (2016). Thinning only occurs at the center of the bend.

Therefore, the maximum tensile strain on the outer surface of the bend based upon the punch geometry is

$$\varepsilon_1^{max} = \ln\left(\frac{R_{outer}}{R_{\substack{Neutral\\Axis}}}\right) \tag{6}$$

hence

$$\varepsilon_1^{max} = \ln\left(\frac{R_{outer}}{R_{\substack{Neutral\\Axis}}}\right) \approx \frac{1}{2}\ln(1 + t_o / R_{punch}) \tag{7}$$

Finally, the normalized major strain, ε_1*, can be defined as

$$\varepsilon_1^* = \frac{\varepsilon_1^{DIC}}{\varepsilon_1^{max}} = \frac{2\varepsilon_1^{DIC}}{\ln(1 + t_o / R_{punch})} \tag{8}$$

where ε_1^{DIC} indicates the surface strain measurement from DIC. The normalized fracture strain can then be related to the bend angle to determine if a correlation can be obtained to relate the fracture strain and bend severity such that bend angles can still be used to interpret the v-bend test.

VDA fracture strains from three different DP980 samples with 1.2 mm, 1.4 mm, and 1.6 mm thickness are presented in Figure 63. Through the normalization, the relationship between the major strain and the bend angle was revealed, see Figure 64.

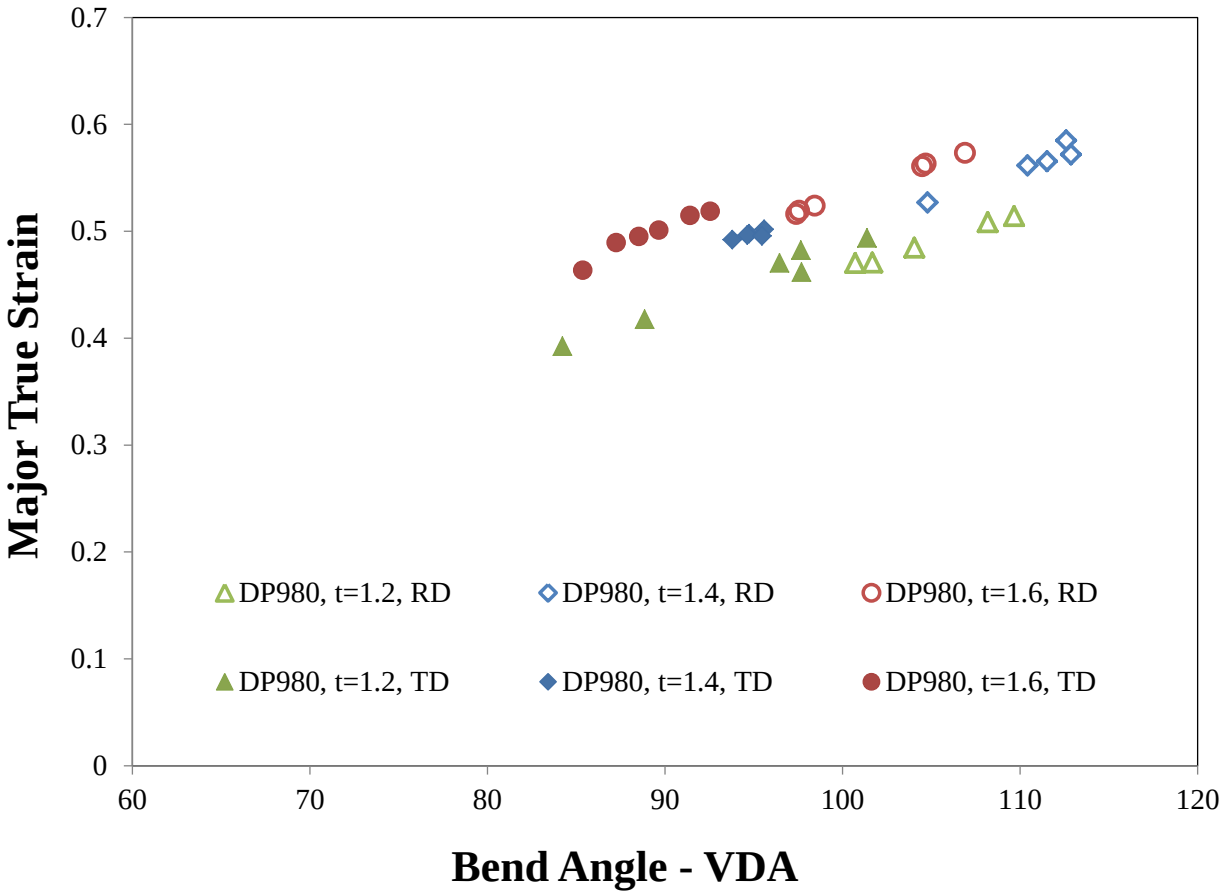

Figure 63 True DIC strain measurement of three DP980 using 0.43 mm punch radius. The bend severity varied depending on the sheet thickness

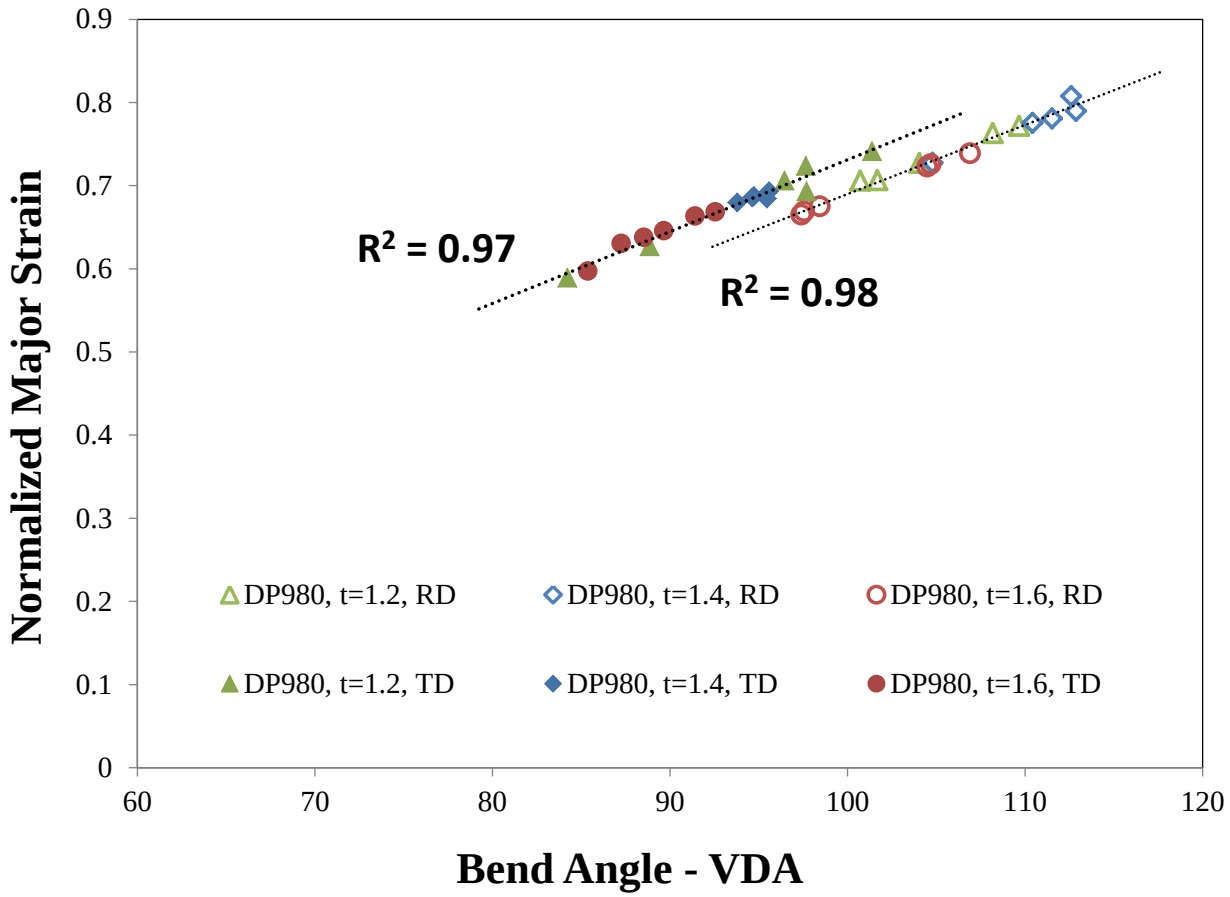

Figure 64 Normalized strain of DP980 samples from three different levels of bend severity. The normalized strain is independent of the bend severity effect

This relationship is remarkable as it is a unique material property that appears to be independent of the bend severity. This normalized strain relationship can be used to predict material responses under any level of bend severity. For instance, Eq. (8) can be re-organized into Eq. (9) to convert the normalized fracture strain of the material, ε*, back into the true strain plane as a generalized form using arbitrary thickness and bend radius as

$$\varepsilon_{1,generalized}(t, R_p) = \frac{\ln(1 + t_o / R_{punch})}{2} \cdot \varepsilon_1^*(\theta) \tag{9}$$

It is critical to state that the generalized data points do not contain any direct physical meaning. However, it was introduced in Section 4.3.2 that the slope of strain development can be used to describe the bending

behavior. This implies that the correlation, or trendline, of the generalized data points can become helpful to understand the mechanism of bending. By normalization, the evolution of major strain of v-bend tests can be estimated based on other experimental dataset under different bend severity.

An experimental approach was performed to verify this idea of bend severity conversion via normalization. The normalized strains from Figure 64 were converted into the true strain space by Eq. (9) with an approximated bend severity of 4, see blue data points in Figure 65. These data points do not represent the actual physical strain and it must be understood that only the trendline is a valid factor in this analysis. The slope of the generalized fracture strains was 0.0067. In Figure 65, the red dashed line represents the experimental strain history from the test with the bend severity of 4. The slope of the strain history was 0.0068. The slope of generalized data points fit well with the linear region of the experimental test result. Therefore, DP980 test results from various bend severity have been successfully transformed into an arbitrary bend severity.

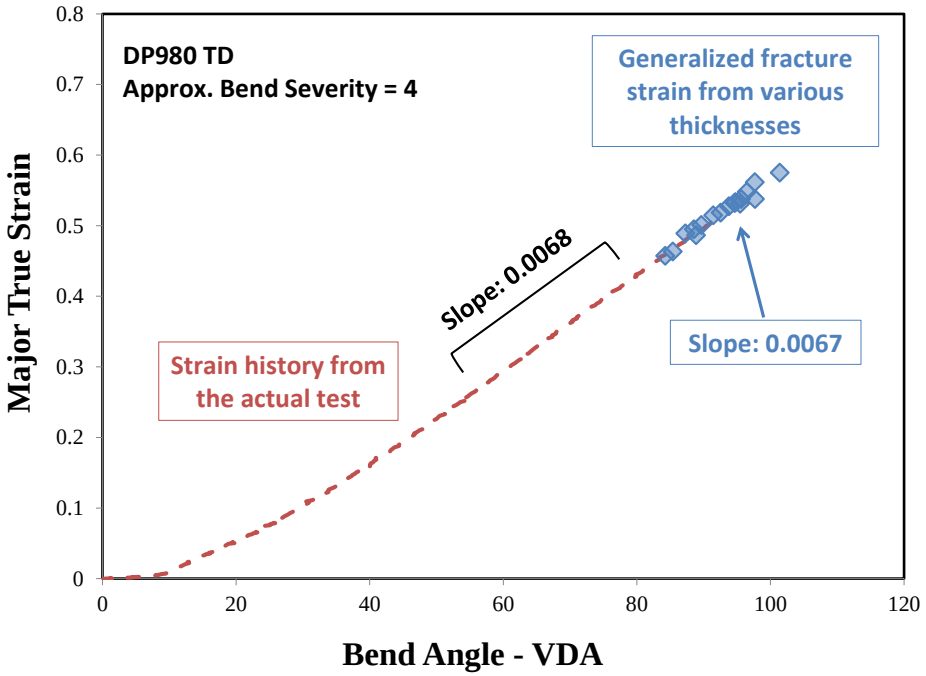

Figure 65 Comparison between the experimental test result and the trendline from generalized strain data. The bend severity was adjusted to be identical on both cases

As mentioned earlier, the significance of the normalized strain correlation from Figure 64 was that it could be converted into any level of bend severity via Eq. (9). A sensitivity analysis was performed to investigate the correlation between bend severity and strain evolution. Figure 66 illustrates the normalized strain correlation of DP980 from Figure 63 converted into various levels of bend severities. A positive relationship between the slope and the bend severity was observed.

The change in slope is an important feature of the correlation since the VDA bend angle will be a function of the bend severity, *t/R*, since the plane strain fracture limit is a material constant. Therefore, it can be concluded that the more severe the bending, the higher the strain gradient thus the major fracture strain will be reached at a lower bend angle due to the steeper relationship, see Figure 67. By using the concept of normalization, the fracture bend angle under other severity of bends can be estimated from a single dataset.

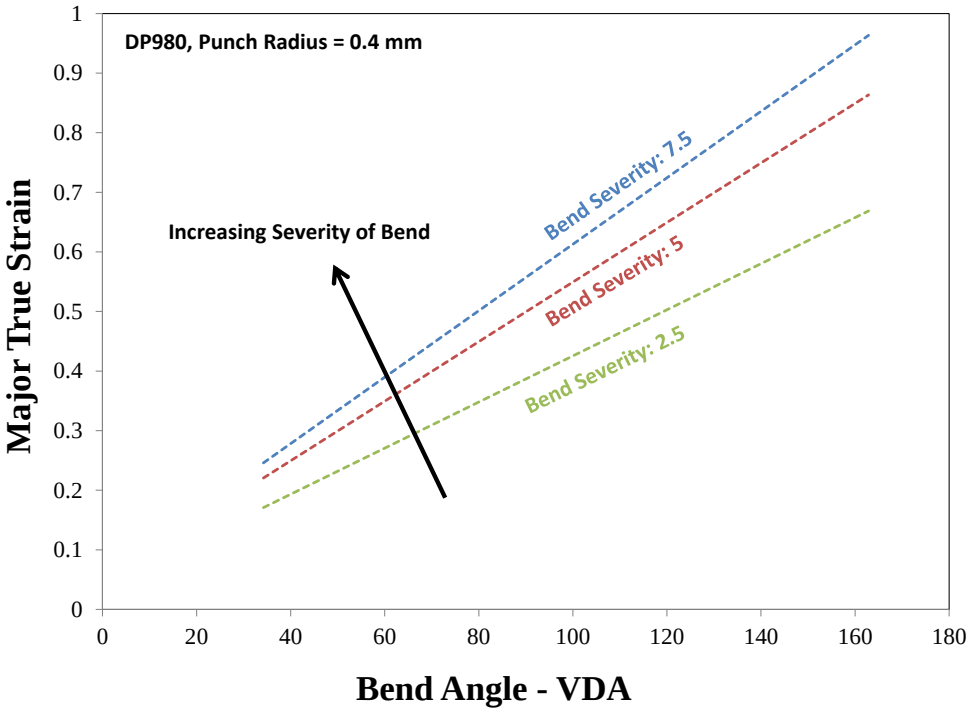

Figure 66 Predicted influence of bend severity on the bend angle. As the bend severity gets more severe, the slope of the correlation gets steeper as higher strains are required to form sharper bend radii

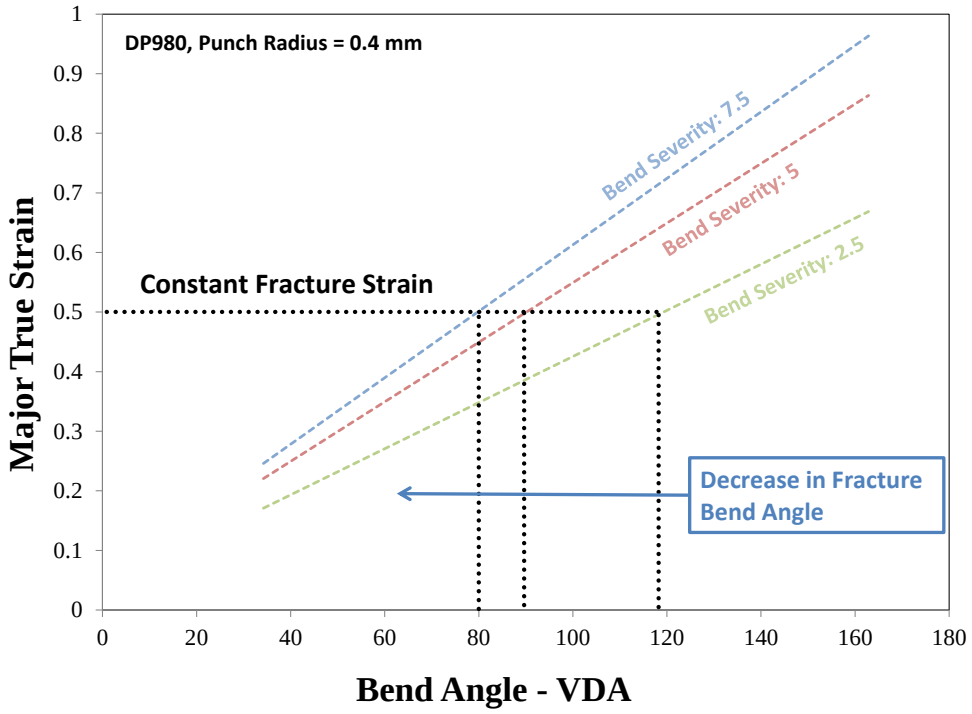

Figure 67 Change in fracture bend angle based on the sheet thickness and the bend radius. With higher bend angle, fracture strain can be reached with a smaller bend angle

4.4.2 Experimental Approach to Bend Severity Analysis

To explore the idea regarding the influence of the bend severity on the fracture bend angle, the DP980 and HS1500 were tested by VDA bend tester with punch tip radii of 0.2 mm, 0.4 mm, and a non-standard punch with a tip radius of 1.0 mm. As observed from the theoretical approach in the previous section, the bend angle is expected to be dependent on the bend severity. If the plane strain failure strain is a material constant, then it is expected that the fracture bend angle should reduce as the bend severity increases.

During the investigation, it was observed that the load history is dependent on the roller gap. To account for the 1 mm radius punch, the VDA guideline to select the roller gap was generalized as

$$L_{\text{Steel}} = 2 \cdot \left(a + r_{punch} - 0.4 \right) + 0.5 \quad [\text{mm}] \tag{10}$$

Thus, if a 0.4 mm radius punch is used, the gap should be the same as the VDA criterion. The larger roller gap required to perform the bend test with a larger punch radius altered the load history as shown in Table 8 and Figure 68. The visual inspection of the DIC images was performed to identify the onset of crack initiation. This method has been adopted here as an alternative method to using the VDA load threshold with the intention of removing the punch radius dependency.

Table 8 Punch load and displacement of HS1500 at VDA load threshold using three different punch tips

Punch Radius	0.2 mm		0.4 mm		1.0 mm	
Load [N]	6917	± 170	6885	± 238	6586	± 155
Disp. [mm]	6.35	± 0.22	6.56	± 0.21	6.97	± 0.14
VDA Bend Angle, θ_{VDA} [˚]	52	± 2	54	± 2	53	± 1
ISO Bend Angle, θ_{ISO} [˚]	52	± 2	55	± 2	54	± 1

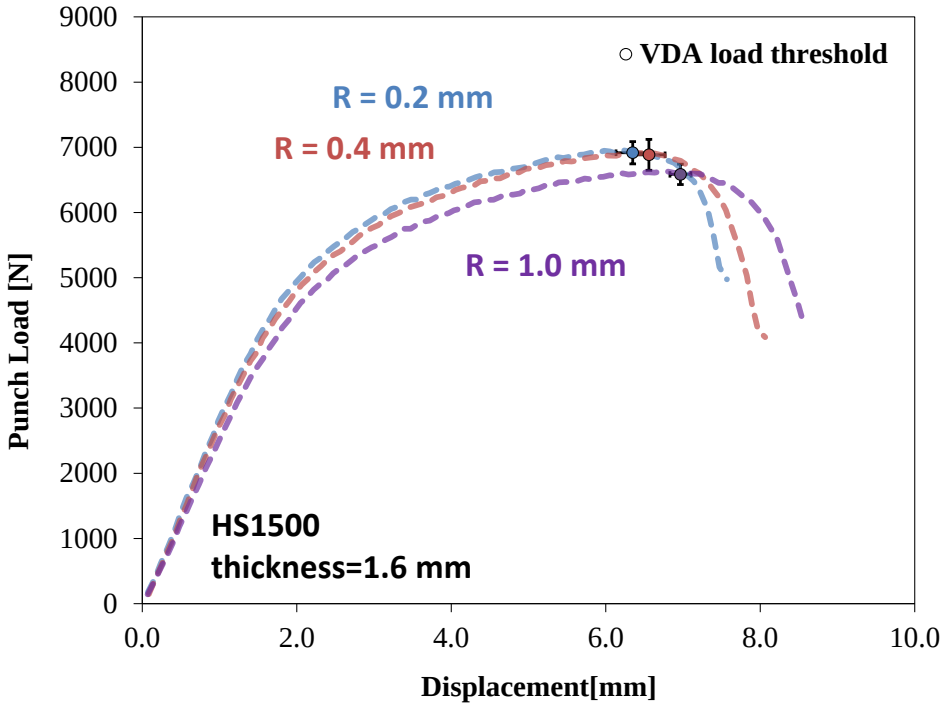

Figure 68 Relationship between punch load and displacement of HS1500 using three different punches. The load history for the larger 1 mm radius punch is significantly different from that of the smaller punches

The initiation of a crack was determined by a visible surface fracture at least 20 pixels long and 3 pixels wide which corresponds to 0.4 mm and 0.06 mm from the setup resolution. An example of defined crack

initiation is presented in Figure 69. Moreover, the bend angle correlation from ISO 7438 (see Eq. (3)) was employed to account the influence of the punch tip radius.

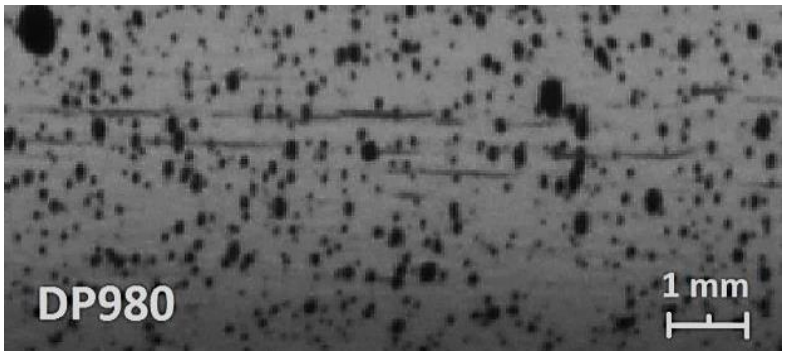

Figure 69 Initiation of hairline cracks of DP980. Crack reaches the width (vertical) of 0.06 mm

Prior to the bend severity analysis on strain development, the strain measurement at the onset of crack was extracted to investigate the influence of the bend severity on the fracture limit. The result indicates that major strain is independent of the bend severity within the considered range of punch radii, see Figure 70.

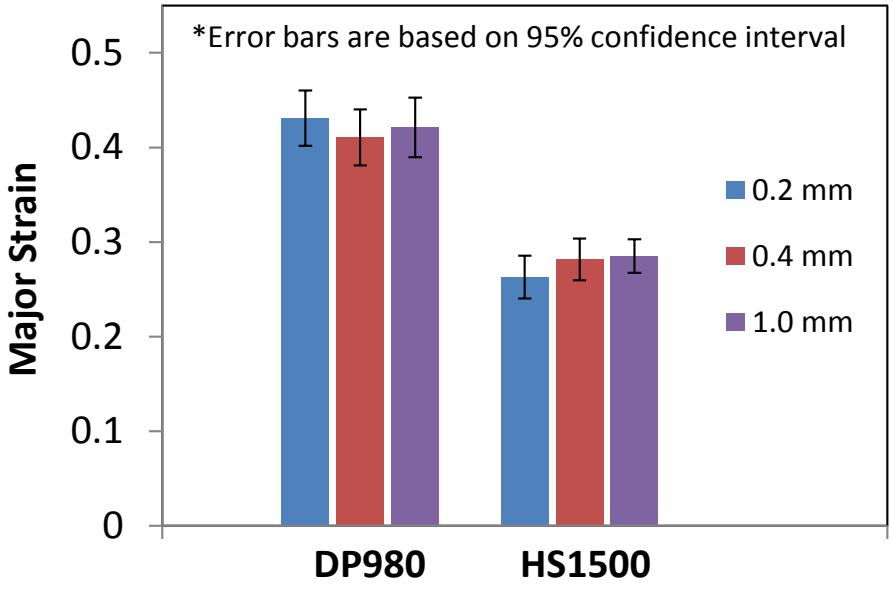

Figure 70 Major strain measurement at the initiation of a visible crack using different punch tip radius in the VDA bend test

The strain histories of DP980 and HS1500 specimens are presented to visualize the influence of the bend severity. A small but distinguishable difference was observed in Figure 71 and Figure 72. It is shown that

an increasing bend severity positively affected the strain evolution and consequently forces the relationship to have a steeper slope. Since the fracture limit for a given stress state is thought to be a constant material property, it can be concluded that the bend angle at fracture must be a function of the bend severity, *t/R*. In other words, the fracture strain will be reached at a lower bend angle if the bend severity is increased. This result coincides with the conclusion drawn from the theoretical analysis in Section 4.4.1.

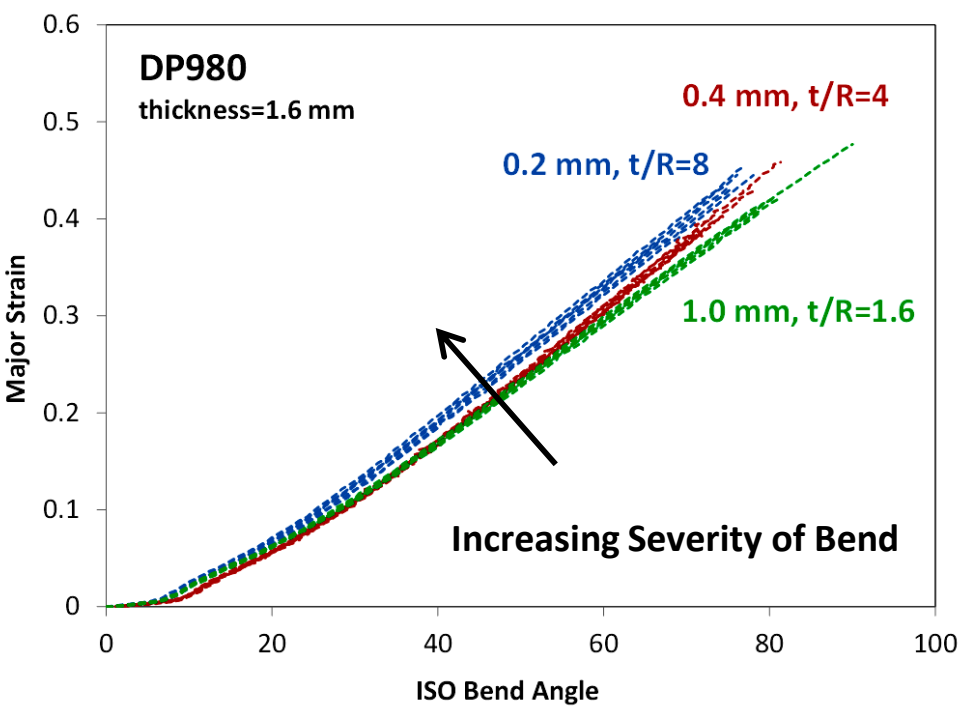

Figure 71 Evolution of the major true strain in DP980 v-bend tests based on the ISO bend angle with different bend severities

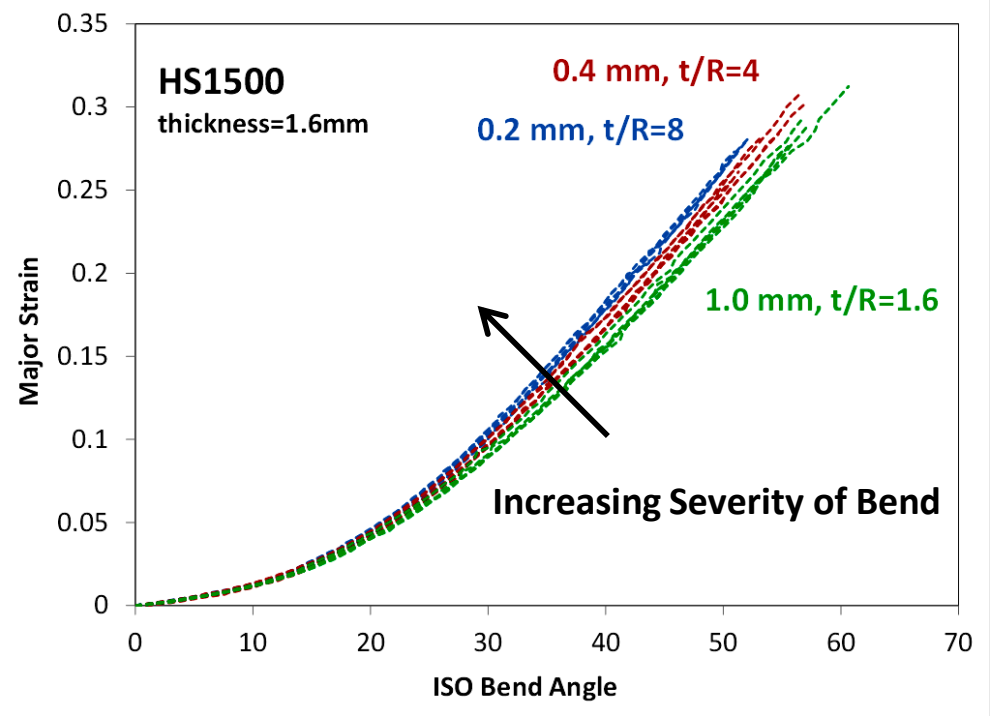

Figure 72 Strain development of HS1500 based on ISO bend angle with different bend severities

It is expected that a larger deviation in the punch radius would result in a more distinguishable difference. However, the first two punch radii were fixed to be 0.2 mm and 0.4 mm by the VDA criterion. The last punch radius was selected to obtain a gradual increase in the bend severity. Employing a larger punch radius increases the risk of lift-off of the material at the punch tip which effectively changes the bend severity by decreasing the inner bend radius as shown in Figure 73. For the considered materials and punch radii, it was verified that the contact between the sample and the punch was well maintained without lifting off.

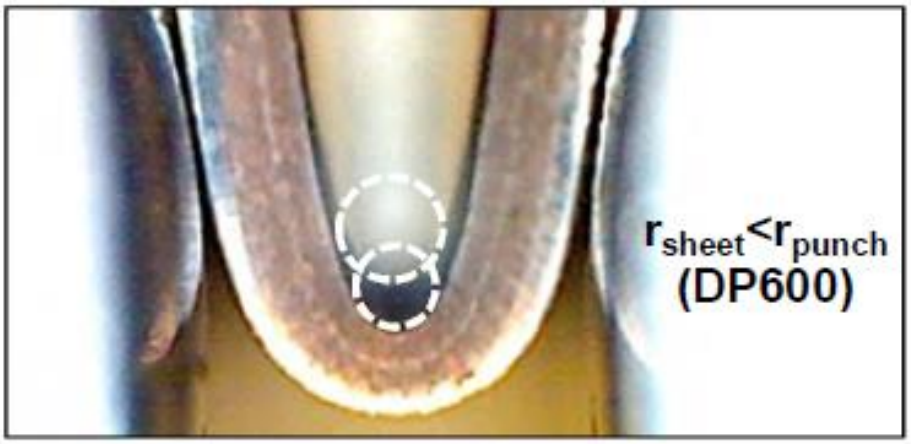

Figure 73 Example of the punch tip lift-off provided by Laurour *et al.* (2013). Due to the gap, the inner bend radius tends to be sharper than the actual punch tip radius.

4.5 Summary of VDA 238-100 Bend Test Result

Various aspects of VDA bend test was investigated and analyzed in this chapter. Novel approaches to establish the test guidelines were performed. With the addition of DIC optical measurement, traditional VDA 238-100 criterions have been evaluated and material responses under pure bending were investigated thoroughly.

The major research results in this chapter can be summarized as:

- A guideline of applying DIC optical measurement system to VDA best test was developed. Post-processing and data extraction method have been developed with custom Matlab script to analyze the obtained data.
- VDA bend tests provided repeatable results with proportional loading under plane strain conditions. Due to the strong through-thickness strain gradient, necking was sufficiently suppressed and multiple cracks occurred across the specimen width with relatively slow crack opening relative to in-plane tests. Therefore, unlike conventional in-plane stretching tests, fracture limit can be investigated clearly and efficiently.

- It was observed that the VDA load threshold provides a reasonable initial estimation for the onset of cracking from a comparison of the DIC images corresponding to the micro- and macro-crack. However, different level of safety factors can be applied based on the application and test condition.
- The theoretical bend angle correlation from VDA 238-100 showed an excellent match with the experimental bend angle measurement whereas the correlation from ISO 7483 tended to overestimate the bend angle with the large bend angle.
- The influence of the through-thickness strain gradient in plane strain bending can be expressed in terms of the bend severity, *t/R*. The strain development with respect to bend angle was observed to be one of the key features to describe the bending behavior which was dependent on the bend severity. From the experimental investigation, the plane strain fracture limit was observed to be a material constant. Therefore, the more severe the bending, the stronger the strain gradient thus the major fracture strain will be reached at a lower bend angle.

5.0 Miniature Nakazima Test

In the previous chapter, the positive influence of through-thickness strain gradient on plane strain fracture characterization was investigated. A similar concept was integrated into Nakazima test as part of this thesis to investigate the effect of curvature under equi-biaxial stretching condition. Traditionally in Nakazima tests, a 100 mm diameter punch is employed to provide *t/R* ratios of 0.006 to 0.08 based on the minimum and maximum thickness permitted in the ISO 12004-2 standard (2008). With the low level of bend severity, it is typically assumed that the effect of curvature is negligible and a homogeneous stretching condition exists through the thickness. In the present study that the mitigation of tensile instabilities is the objective, increasing the bend severity is desired to obtain the proportional biaxial loading condition.

Additional hemispherical punches were fabricated with punch radii of 5, 10, and 25 mm to complement the standard 50 mm radius punch, see Figure 74. The punches were fabricated from 4140 steel and surface hardened to 55-60 HRC. It is important to state that depending upon the material behavior and sheet thickness, a tensile instability may still occur even using the smallest 5 mm punch since the test still involves some stretching although deformation is bending-dominated. The test procedures and equipment were identical to the standard LDH test except that 35 mm lenses with higher magnification were employed since the deforming surface is much smaller. Two DP980 steels with different thicknesses were considered in this study to investigate the forming behavior of materials with a similar mechanical property but under different severity of bend. Moreover, AA5182 was also considered to investigate if the test is sensitive to the material since AA5182 has a dynamic hardening response that saturates at moderate strain levels. The selected materials were sheared into 203.2 mm x 203.2 mm (8” x 8”) square specimens for equi-biaxial stretching condition. Unfortunately, due to the complexity of scaling down the dog-bone specimens while maintaining the strain conditions, the bend severity analysis was performed only under

equi-biaxial loading. Future work will investigate performing miniaturized Nakazima-type tests to determine the limit strain for other strain states using the smaller punches.

Figure 74 Hemispherical dome punches. From left to right: 50 mm, 25 mm, 10 mm, and 5 mm in radius

5.1 Post-processing and Data Extraction

Both traditional Nakazima and miniature dome tests were performed using the formability press introduced in Section 3.2. DIC strain measurement was employed to obtain the surface measurement as introduced in Section 3.1. The recorded images from Vic-Snap software using a pair of 4-megapixel square sensor point-grey Gazelle cameras were post-processed with Vic-7 DIC software a VSGL of approximately 0.5 mm. This virtual strain gauge level was maintained constant while lens magnification varied with the punch size. The onset of cracking can be easily determined in the Nakazima tests as abrupt macroscopic cracking occurs. The fracture location was identified by inspecting the peak strain location from one image prior to the fracture moment as shown in Figure 75 and Figure 76. Similarly, the punch displacement was measured using DIC from the apex of the dome. *In-situ* strain measurement was extracted from a small circle of 0.5 mm radius, and the size of the circle decreased proportionally based upon the punch size.

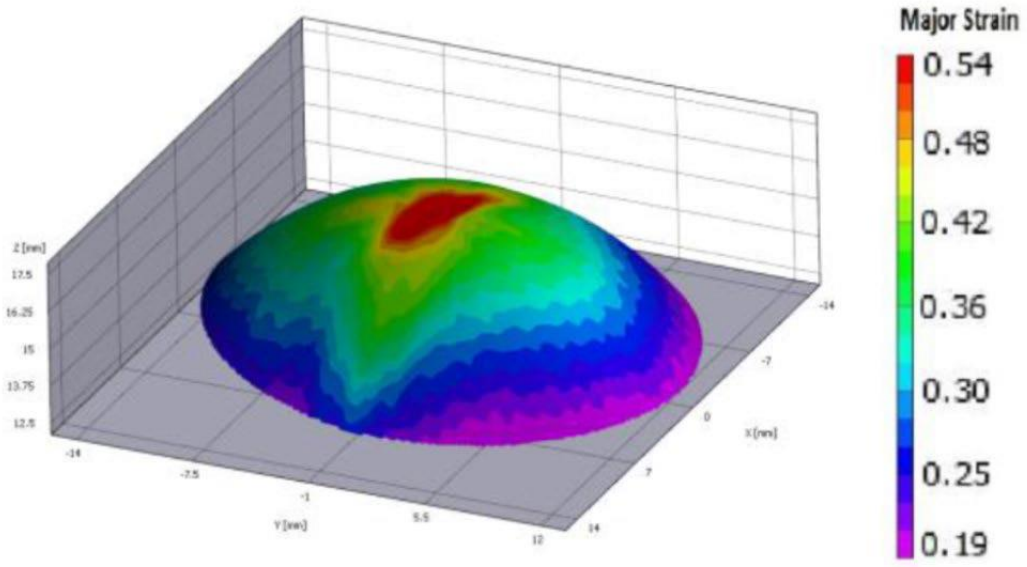

Figure 75 3D contour plot of the major strain measurement of the equi-biaxial dome test using DIC. The miniature punch with the radius of 25 mm was used on DP980 (t = 1.6 mm) specimen.

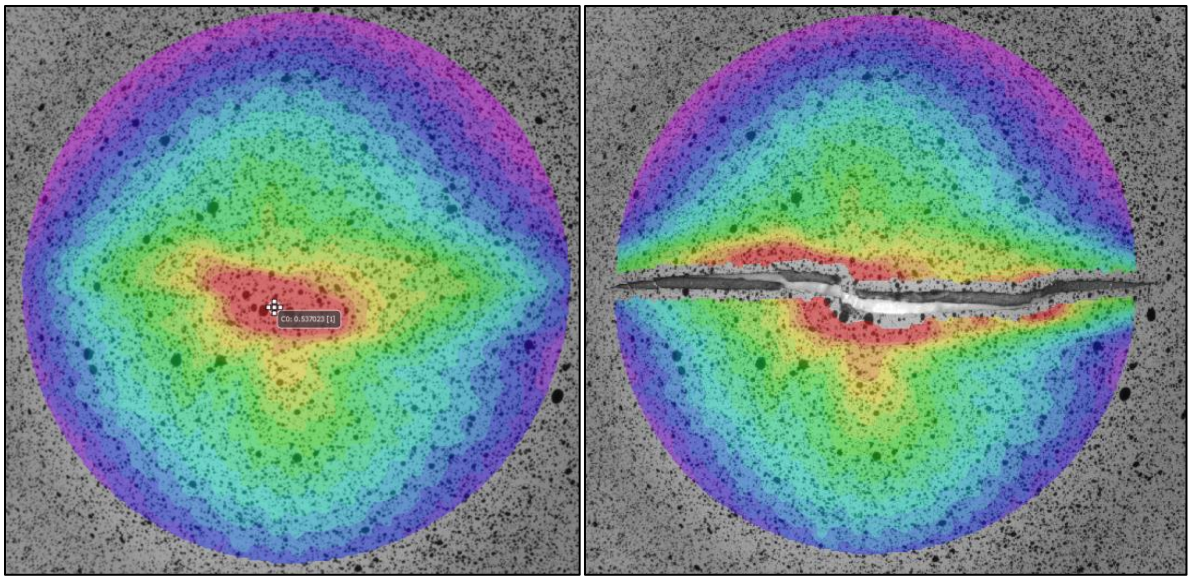

Figure 76 2D contour plot of DP980 specimen for one frame before the fracture (left) and at the fracture (right). Failure location is determined by the peak strain point on left figure (circle measurement)

5.1.1 VSGL study of Miniature Dome Test

A parametric study of the VSGL for the miniature Nakazima tests was also performed on the 5 mm radius hemispherical punch from which the largest major principal strains were observed and the deformation field is the smallest. The major strain measurements were found to be insensitive to the choice of VSGL.

The variation was minimal between VSGLs from 0.1 to 0.6 mm as shown in Table 9. Similar to the bending test, the VSGL of 0.5 mm was selected which is in the reasonable range of precision.

Table 9 Influence of the VSGL on the major failure strain for the DP980 steel using a 5 mm radius hemispherical punch

VSGL [mm]	0.1	0.2	0.3	0.4	0.5	0.6
Major True Strain at Fracture	0.75	0.75	0.75	0.74	0.74	0.73

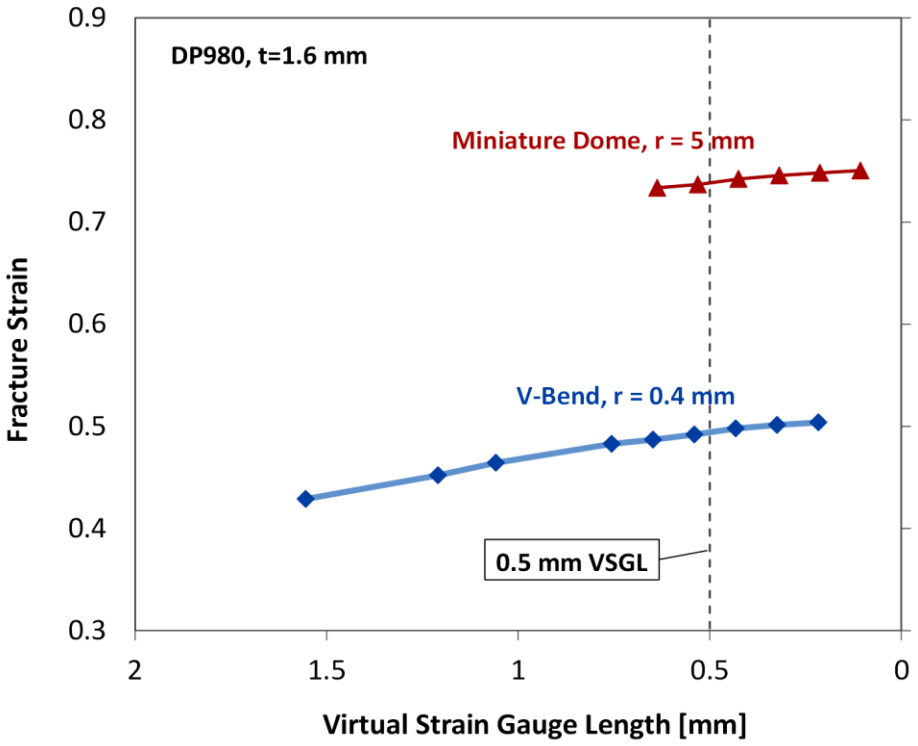

Figure 77 Comparison of VSGL on the major failure strain. Influence of the VSGL is minimal for the miniature dome test

5.2 The Effect of Bend Severity in Miniature Dome Test

The conventional 50 mm radius punch is designed to provide stretch-dominated stress-state so that strain localization appeared as shown in Figure 78. The localization results in the strain path diverging from the ideal path for equi-biaxial stretching. After localization, deformation concentrates in a direction based upon material anisotropy leading to a rapid acceleration of the major principal strain prior to fracture.

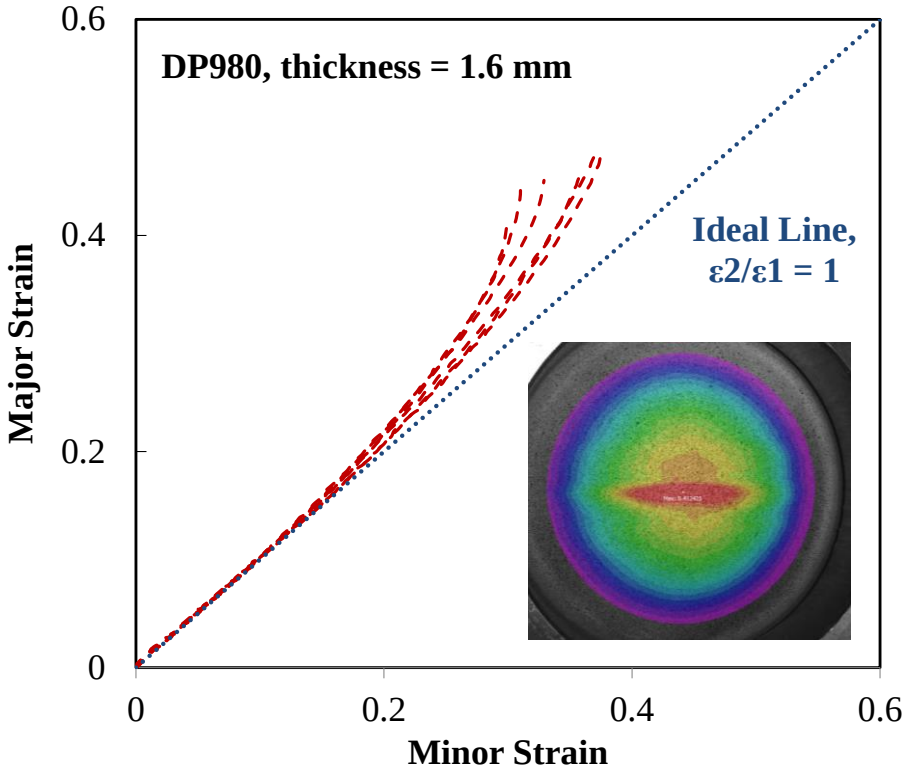

Figure 78 Strain evolution of equi-biaxial LDH dome test of DP980. Strain paths are diverging from the ideal path

To apply the concept of curvature on equi-biaxial tension test, the LDH tests were performed using hemispherical punches with the four different radii ranging from 50 mm to 5 mm. Similar to the previous analysis, smaller radius of the punch is intended to generate more severe bending thus suppresses the strain instability.

As expected, the punch load and displacement decreased with the punch radius, see Table 10 and Figure 79. The punch load decreased due to a smaller amount of material being deformed and the displacement also decreased because a higher strain gradient was obtained from the severe bending.

Table 10 Fracture load and punch displacement for DP980 using different hemispherical punches

Punch Radius	Load [kN]		Dome Height [mm]	
50 mm	200	±7.52	29	±1.27
25 mm	93	±1.57	17	±0.24
10 mm	39	±0.44	11	±0.22
5 mm	22	±0.48	8	±0.26

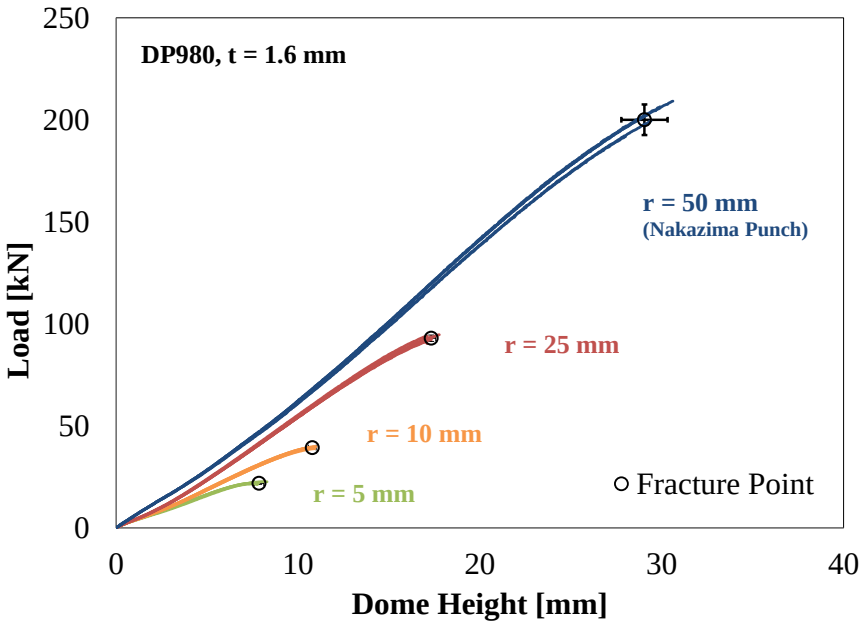

Figure 79 Load development of dome tests using different hemispherical punches. Higher load response was measured with larger punches as more material was engaged

The progressive linearization of the biaxial strain path with decreasing punch tip radius is clearly demonstrated in Figure 80. As the induced curvature of the sheet gets more severe, the influence of stretching is reduced and necking becomes suppressed. For the smallest hemispherical punch with the 5

mm radius, an approximately ideal equi-biaxial strain path was obtained with cracking at the dome apex (marked with a black dashed line in Figure 80).

Table 11 Fracture strain of DP980 samples from different punch sizes. Smaller punch corresponds to higher bend severity

Punch Radius	Major Strain		Minor Strain		Von Mises Eq. Strain	
50 mm	0.45	±0.02	0.34	±0.03	0.79	±0.05
25 mm	0.57	±0.03	0.46	±0.03	1.04	±0.05
10 mm	0.63	±0.05	0.56	±0.06	1.19	±0.10
5 mm	0.67	±0.04	0.64	±0.06	1.31	±0.09

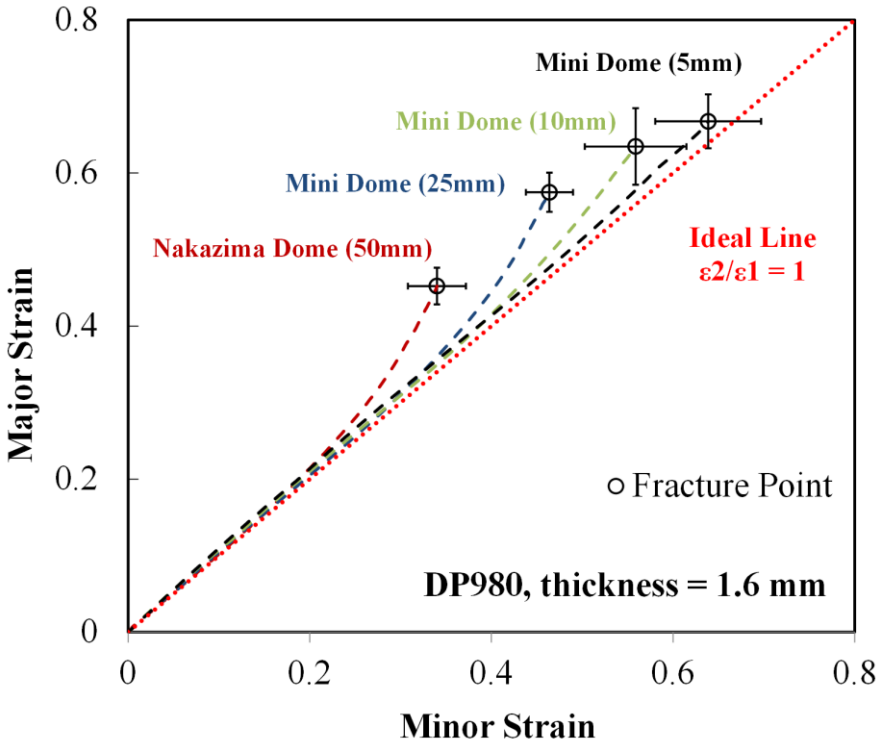

Figure 80 Representative strain path of DP980 equi-biaxial dome test using different punch sizes. Each test condition was tested at least 5 repeats

In Figure 80, it was noticeable that there is a relatively large variation in the strain path using the 5 and 10 mm punches. This is believed to be due to difficulty in controlling friction with the small punches so that some tests would localize away from the punch apex. Since there is still stretching along with bending in these tests, a tensile localization can still occur. The strain paths for five repeated tests using the 5 mm

radius punch are shown in Figure 81. Two of the tests did experience localization while the other three tests cracked at the dome apex under an ideal equi-biaxial strain path.

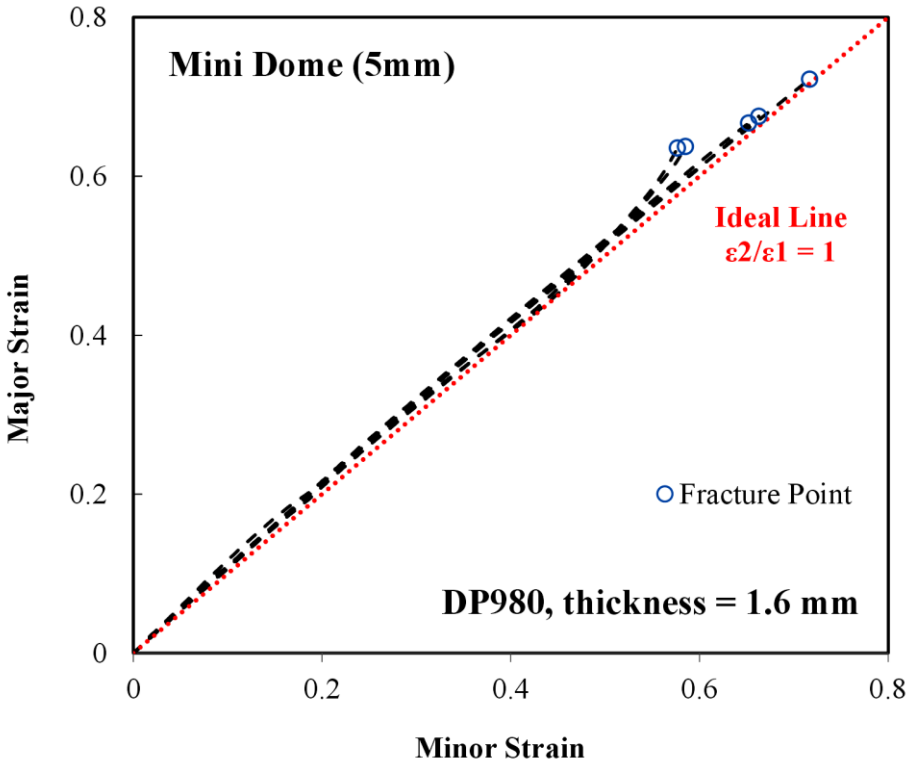

Figure 81 Strain path of dome tests of DP980 using the 5 mm radius punch

Similar results were derived from the repeated test using DP980 with the different thickness (1.2 mm) and AA5182 as shown in Figure 82 and Figure 83, respectively. A progressive linearization with a dramatic improvement on the fracture limit was recorded from both tests. It is remarkable to recognize how much the fracture limit is being underestimated by the effect of necking. As shown in Table 12 and Figure 84, the fracture equivalent strain showed a significant increase of almost 50% by using the 5 mm punch radius. Relying upon a standard 100 mm hemispherical punch for fracture characterization in biaxial stretching leads to significant errors even when using 3D DIC strain measurement.

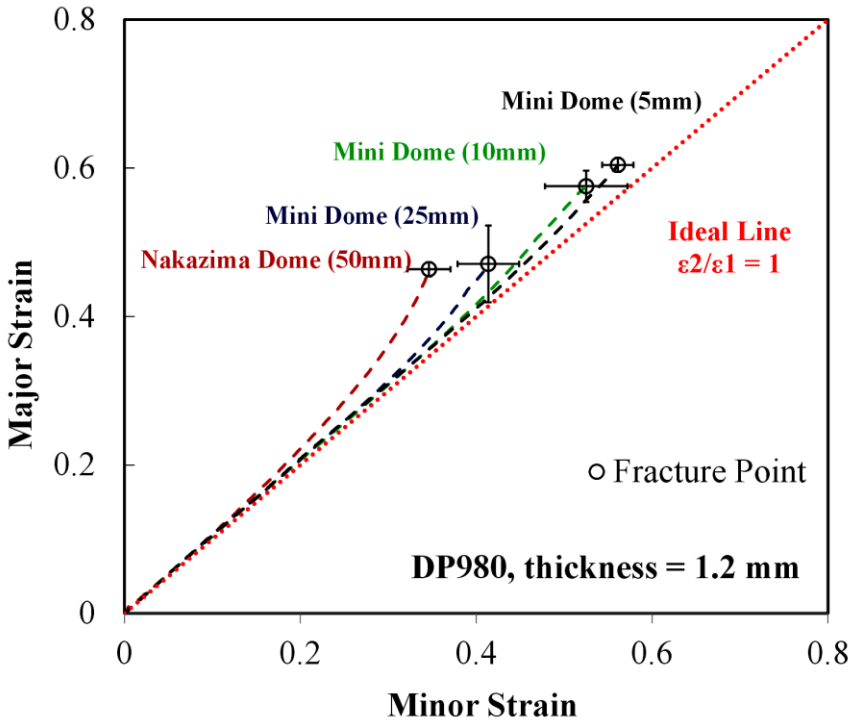

Figure 82 Representative strain path of DP980 equi-biaxial dome test using different punch sizes. Note that this DP980 has a different thickness than the DP980 investigated in Figure 80

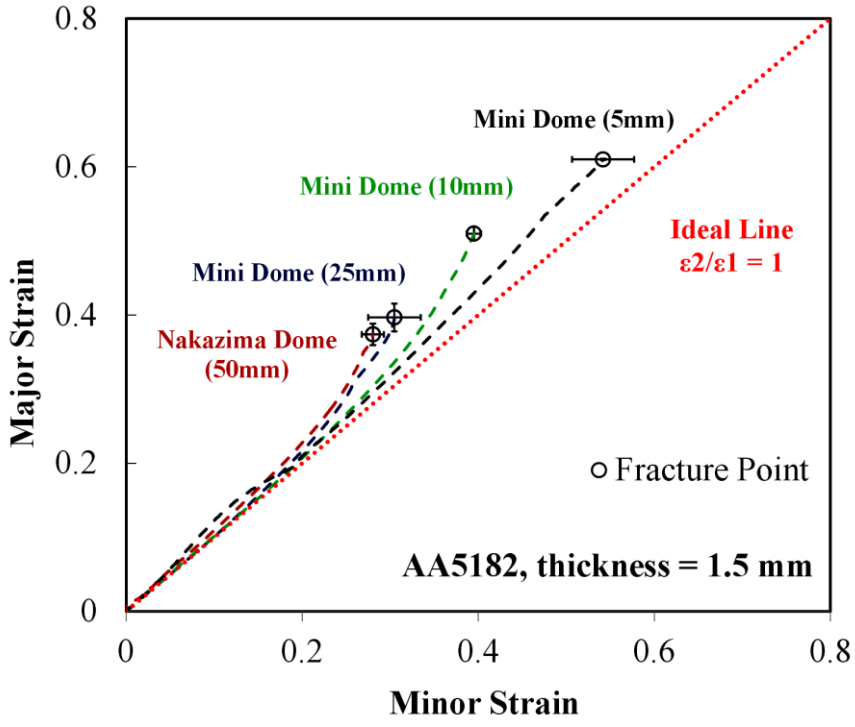

Figure 83 Representative strain path of AA5182 equi-biaxial dome test using different punch sizes. Each test condition was tested at least 5 repeats

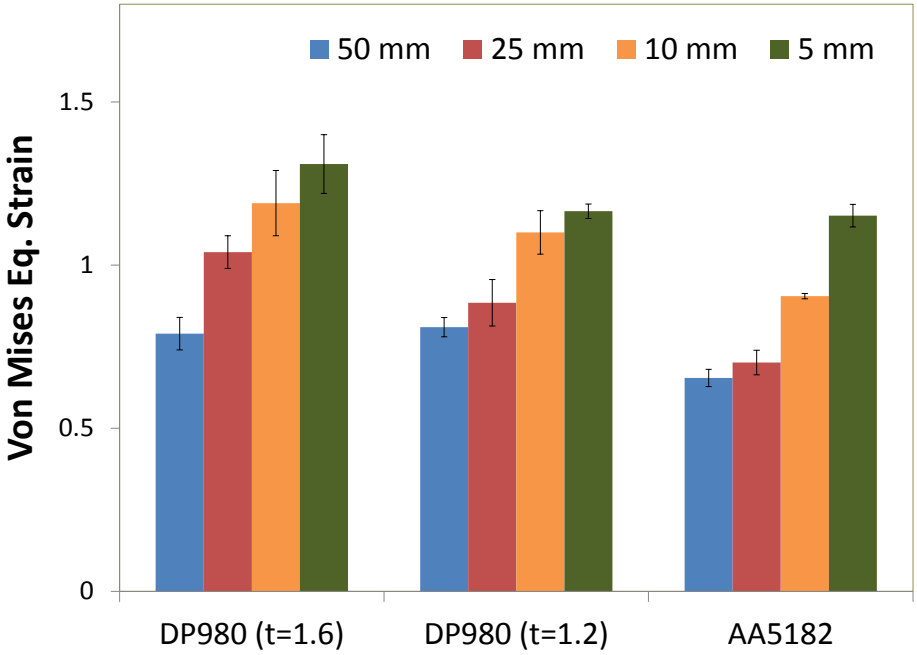

Figure 84 Comparison of equivalent strain results under different level of bend severities of each material

Table 12 Summary of equivalent strain results under different level of bend severities of each material

Punch Radius	**Equivalent Strain Measurement at Fracture**		
	DP980 (t = 1.6 mm)	DP980 (t = 1.2 mm)	AA5182 (t = 1.5 mm)
50 mm	0.79	0.81	0.65
25 mm	1.04	0.89	0.70
10 mm	1.19	1.10	0.91
5 mm	1.31	1.17	1.15

Evidence of the necking mitigation by punch radius was also seen in the strain distributions as shown in Figure 85. As the punch radius decreases, the strain distribution becomes more uniform since localization in the limiting direction of the material was delayed until larger strain levels. At last, the smallest punch with a radius of 5 mm showed a circular strain distribution, and it can be concluded that the strain instability appears to have been successfully suppressed.

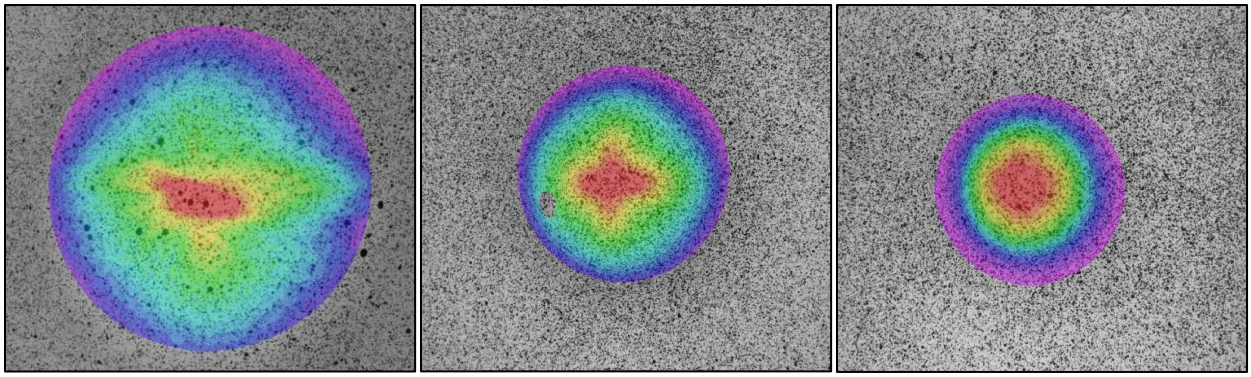

Figure 85 Strain distributions at failure moment of 3 mini-dome punches: 25 mm (left), 10 mm (center), and 5 mm (right, non-localized sample result) radius punches

It is also interesting to note that the fractured specimens appeared to show a transition away from necking-based failure as the punch radius was decreased as shown in Figure 86. Using the traditional LDH test as a reference, crack orientation aligns with the rolling direction for the 50, 25 and 10 mm punches which corresponds to fracture occurring in the transverse direction. However, the majority of the test specimens using the 5 mm punch showed a cross-shaped fracture pattern as shown in the bottom right corner of Figure 86. This phenomenon indicated that the strain localization is effectively suppressed and the equi-biaxial loading condition is truly maintained until the fracture moment. Consequently, the visual inspection of the fracture also agreed with the previous conclusion that the test becomes non-directional when a severe curvature is induced upon the sheet.

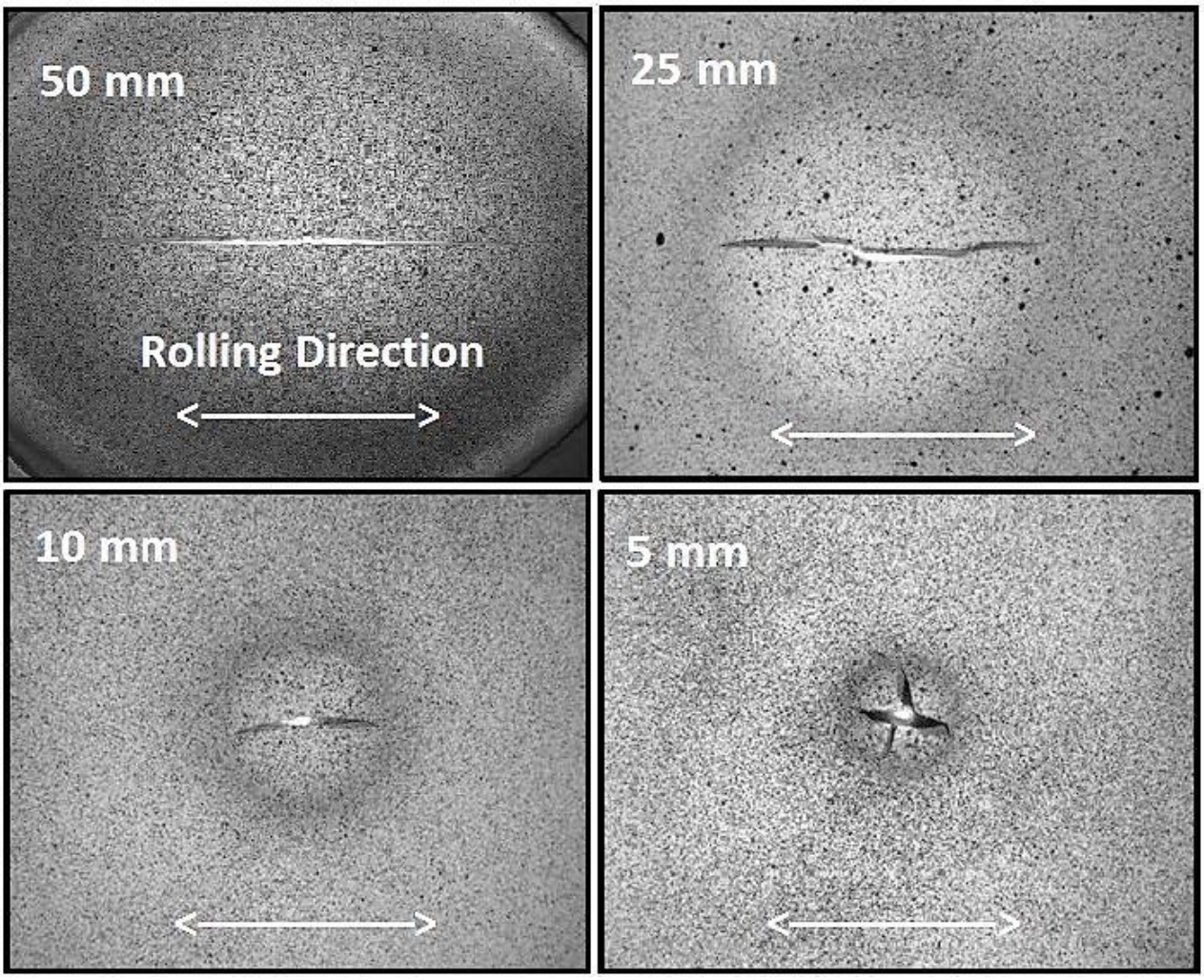

Figure 86 Shape of the post-failure crack of DP980 (t=1.6mm) specimen using punch radius of 50 mm (top left), 25 mm (top right), 10 mm (bottom left), and 5 mm (bottom right)

5.3 Summary of Miniature Nakazima Test Result

The application of the through-thickness strain gradient on equi-biaxial stretching was experimentally investigated in this chapter. The result and analysis were in line with the previous observation from the VDA bend test as improvement in formability was clearly identified as severe bending was applied.

In contrast to the VDA bend test in which the pure bending condition is expected, the miniature dome test involved a noticeable amount of stretching during the process. As a result, evidence of localized necking

was found especially in tests with larger punches. However, as more severe bending was applied by smaller punches, a gradual linearization on the strain path was observed along with non-directional strain distribution from DIC surface measurement. With the smallest punch radius of 5 mm, the fracture limit under proportional equi-biaxial loading was obtained. The linear strain path provided a remarkable amount of improvement in the equivalent fracture strain and it emphasized why the influence of through-thickness strain gradient has to be considered in the practice of fracture characterization.

6.0 Stretch Bend Test

From the previous analysis in Chapter 4.0 and Chapter 5.0 regarding the v-bend test and the miniature dome test, the significant disagreement between the bending and the stretching deformation was identified and analyzed. Pure bending, such as VDA bend test, is an efficient method to describe material's fracture limit whereas the conventional forming limit can be characterized via stretch-dominant test setup, such as Nakazima test. However, the combined effect of stretch-bendability of a material are not well documented within the literature and no standardized test exists to characterize these effect even though this type of deformation mode is common in many forming operations. Therefore, in this thesis, the stretch-bend test was proposed to explore combined effect of stretching and bending under near-plane strain conditions in an effort to bridge the gap between observations in the plane strain stretching and plane strain bending.

6.1 Experimental Setup of Stretch Bend Test

A stretch bend tool was manufactured with an adjustable punch tip radius. The punch tip radius varies from 0.4 mm to 15 mm to provide a variety of stretch-bend ratio as shown in Figure 87. These punch tools can be integrated into the MTS dome tester based on the ISO 12004-2 standard (2008) described in Section 3.2.

Figure 87 Stretch-bend punches with different radii (left) from left to right: 0.4, 1, 2, 5, 10, and 15 mm in radius. Smaller punch radius corresponds to the higher bend severity. Punch assembled to the holder (right)

The blank geometry used in the stretch-bend test was consistent with the 1" and 3" Nakazima dome specimens derived from the ISO 12004-2 (2008), see Figure 28. DP980 with the thickness of 1.2 mm and AA5182 were selected for the stretch-bendability analysis due to their well-balanced bendability and strength. The edge of the specimens was CNC machined to ensure that no edge cracking occurred during testing. The sample alignment is very sensitive in this test setup. The specimens must be aligned exactly perpendicular to the punch knife to ensure no shear deformation would occur. An example of stretch-bend deformation is shown in Figure 88 in which the bending is perpendicular to the specimen length.

Figure 88 Deformation of a 3" wide specimen during stretch-bending process illustrating that the specimen is perpendicular to the punch

After preliminary trials with various punch tip radii, it was noticed that punch radius smaller than 2.0 mm results in a "cutting" type operation instead of forming due to the large gap between the punch and binder. The radius was too sharp given the gap to promote any wrapping of the sheet around the punch radius. Therefore, punch radii of 2, 5, 10, and 15 mm were selected for further testing. Similar to the miniature dome test, the sharper punch with a smaller radius was expected to provide a more severe bending and less stretching. Future work will investigate the fabrication of an adjustable die to change the gap and to promote more bending such that the smaller punch radius of 2.0 mm can be employed.

DP980 with the thickness of 1.2 mm and AA5182 with the thickness of 1.5 mm were machined into dog-bone shaped specimens with 1" and 3" in width. These widths were selected to obtain a distinct difference in test conditions. 3" specimen was selected since it was the largest width which can be subjected to the stretch bend tool. This geometry was expected to provide near-plane strain condition. On the other hand, 1" specimen was designed to provide more a noticeable path change as the punch radius was varied. For example, 1" specimen with the largest punch (r = 15 mm) would give the strain path closest to the uniaxial stretching.

General test settings such as die geometries and clamping are identical from the Nakazima dome test. A constant clamping force of 640 kN with lock bead was applied throughout the process. The test was a displacement-controlled process with a constant punch speed of 0.25 mm/s which is intended to reduce any influences related to strain-rate effects. Similar to the Nakazima test, the punch and the specimen interface was lubricated with a combination of Teflon sheets and Vaseline which was observed to be sufficient for the selected testing range.

6.2 Post-Processing and VSGL Study of Stretch Bending

The camera setup used in the stretch-bendability assessment was identical to that used in the dome tests (Section 3.1). A pair of cameras was used in a 3D stereoscopic configuration to acquire time-synchronized images of each stretch-bend test. The cameras were rated for up to 150 frames per second of operation, given that stretch-bend tests were completed at a punch speed of 0.25 mm/s, approximately 8 to 10 frames per second were used for image acquisition purposes. This frame rate and punch speed combination yielded approximately 32 to 40 frames per mm of punch displacement. Similar to the miniature dome test, the small circle with a radius of 0.2 mm was used to extract *in-situ* strain measurement.

A brief convergence study on the effect of VSGL on the stretch-bend test using a 2 mm radius punch was performed for DP980 material. The result is summarized in Figure 89. It can be seen that the major fracture strain continuously increases with the reduction of VSGL. Similar to previous test designs, 0.4 mm VSGL was determined to a fair trade-off between the accuracy and the computational resource consumption.

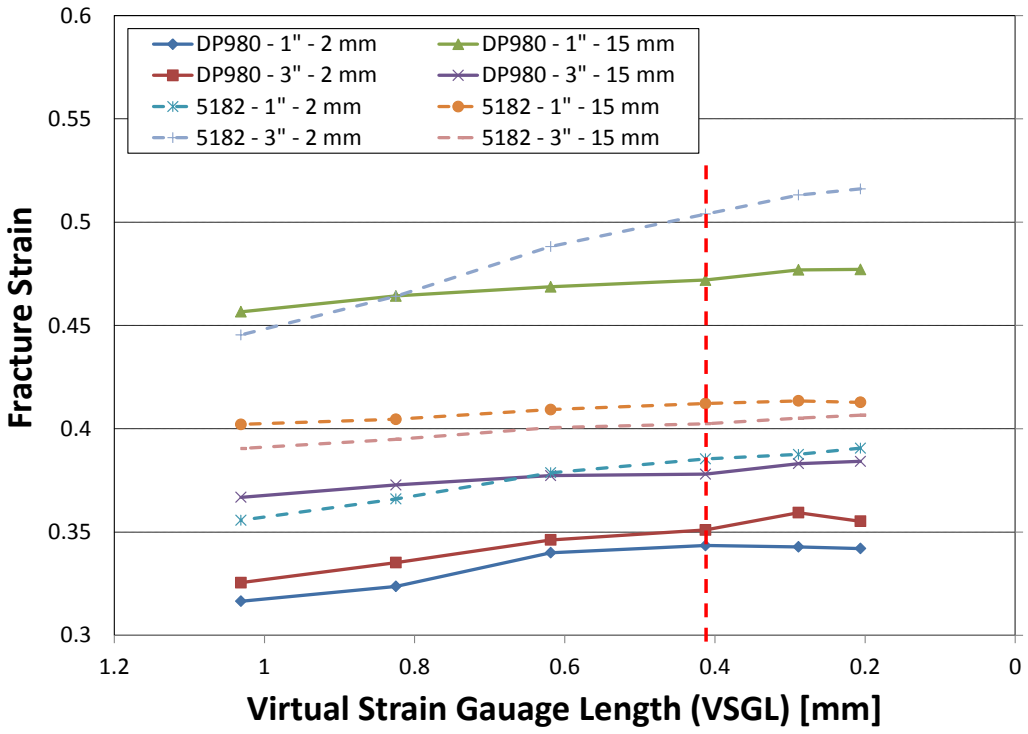

Figure 89 Influence of the VSGL on the peak major strain using various VSGL. An approximately 0.4 mm VSGL was selected and applied for all analysis in this section.

6.3 Time-dependent Limit Strain Determination

This stretch-bendability work is a new type of test and no formal standards are currently available regarding the analysis of the resulting data. The ISO 12004-2 (2008) method is an approach for determining formability from dome tests; however, it was developed for the reconstruction of strain distributions on the much larger sample and cannot be applied in the current work without modification of the fitting parameters as stated by Centeno *et al.* (2014). Conversely, the time-dependent method, such as Volk and Hora (2011) and Martínez-Donaire *et al.* (2014), is a strictly local approach and focuses on the necking location only. Therefore, this approach was employed in this study to find stretch-bendability limit strains. As shown in Figure 90 as an example, a rapid acceleration in strain rate (blue line) was used as an indicator of the onset of necking. Fitting lines were drawn from the initial and final stage of the deformation as shown in Figure 90 as black dashed lines. These fitting lines were determined by the least

square method. The intersection between the two fitting lines was identified as the forming limit of this test.

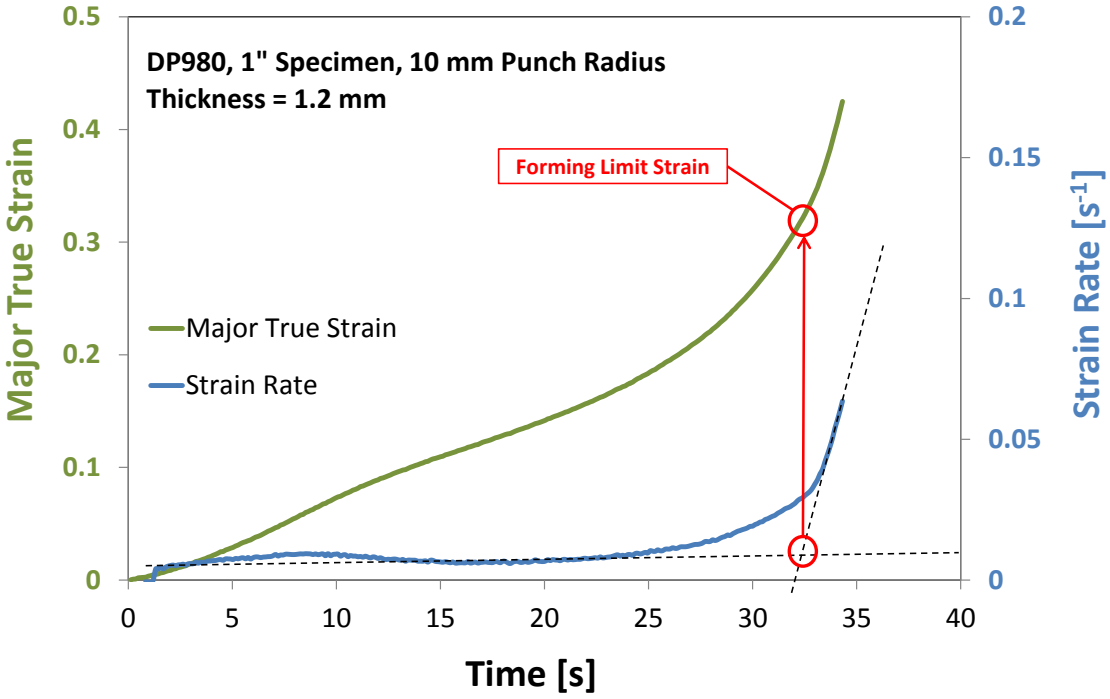

Figure 90 Detection of the onset of strain instability with linear curve fitting method. Due to the combined effect of bending and stretching, the strain rate before the localization was not perfectly linear

6.4 Experimental Observation

The load responses of stretch-bend tests are shown in Figure 91. The higher peak load was recorded as the punch radius gets bigger since more material was engaged by the punch. Similar to the VDA bend test case, a linear load increment was observed at the initial stage of bending. Conversely to the v-bend case, the load then increases near-linearly until the fracture without any significant load drop.

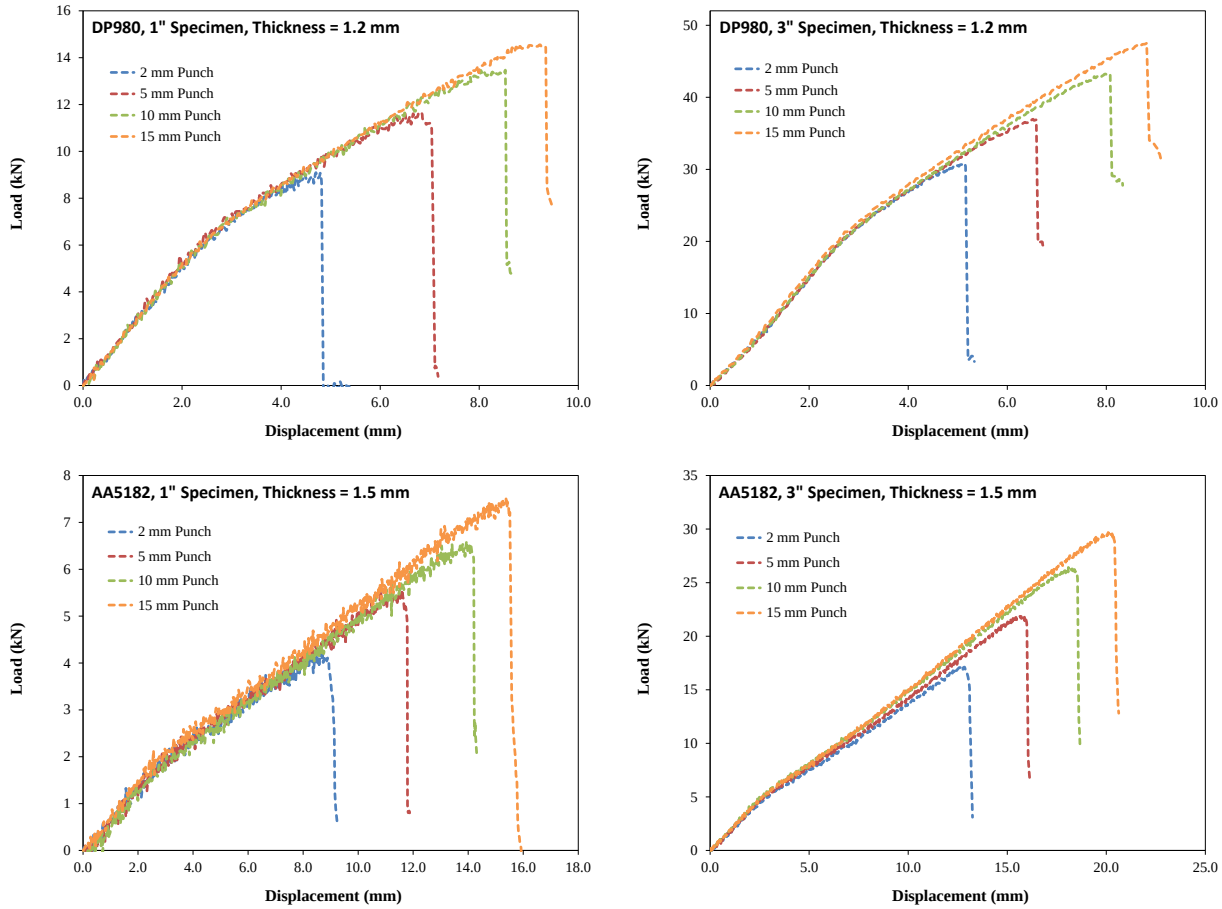

Figure 91 Load and displacement measurements of all test conditions: DP980 specimens (top), AA5182 specimens (bottom), 1" specimens (left) and 3" specimens (right)

The development of the major strain under stretch-bending is shown in Figure 92. Due to the complicated test geometry involving with both stretching and bending, the strain evolution showed a non-linear behavior. Moreover, the strain development was rapidly accelerated at the end of the deformation which can be considered as an indicator of the strain localization. This rapid acceleration was observed from all test conditions.

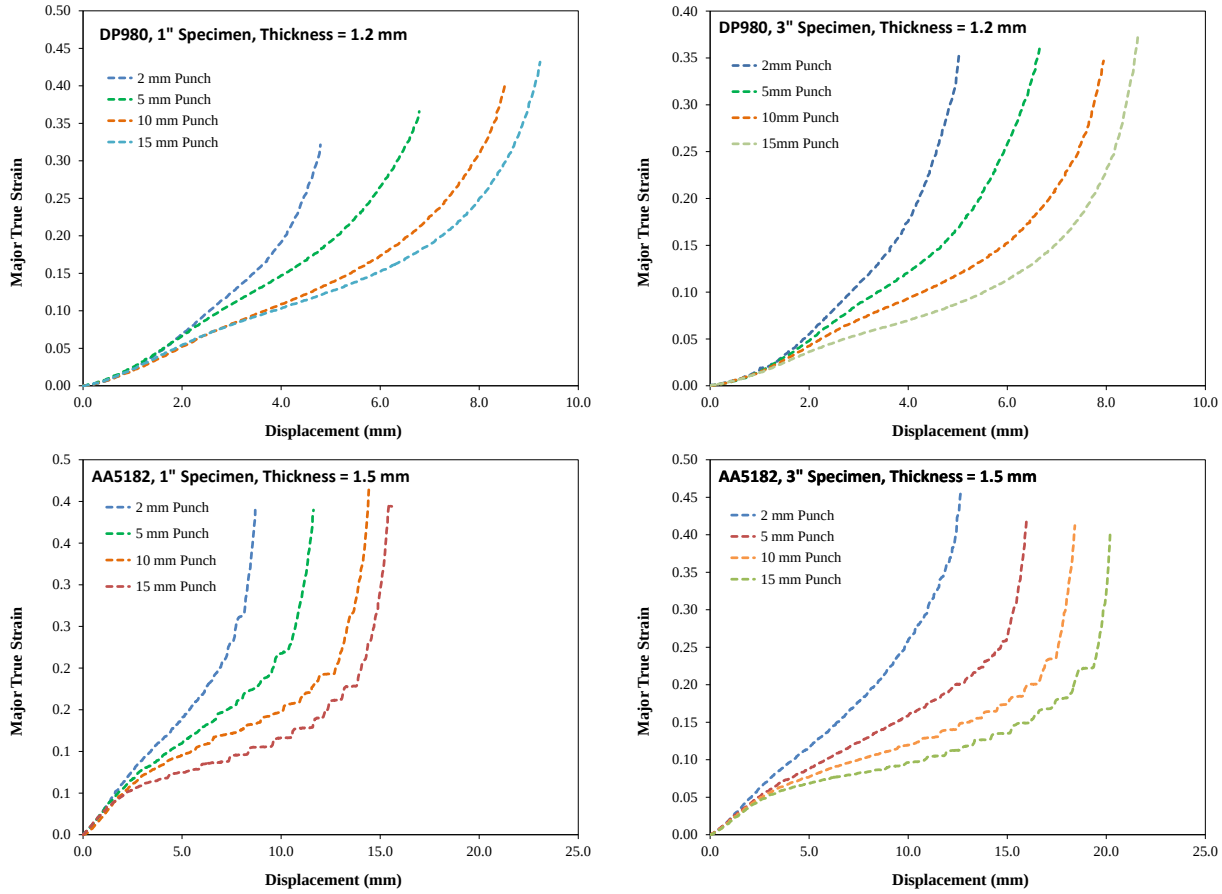

Figure 92 Major strain evolutions of all test conditions: DP980 specimens (top), AA5182 specimens (bottom), 1" specimens (left) and 3" specimens (right)

Conversely to the DP980 result which showed a smooth deformation curve as shown in Figure 92, a stress wave traveling along the major strain direction was observed during the test of AA5182 specimens. This phenomenon can be also seen in the strain history as shown in Figure 93. There are multiple steps in the major strain which corresponds to spikes in the strain rate. This behavior is due to the Portevin-Le Chatelier (PLC) band behavior that is commonly found in 5000 series aluminum alloys. Similar observation was reported from Neuhäuser *et al.* (2004) and Halim *et al.* (2007) that both studies used 5000 series aluminum alloy to investigate the PLC effect under tensile deformation.

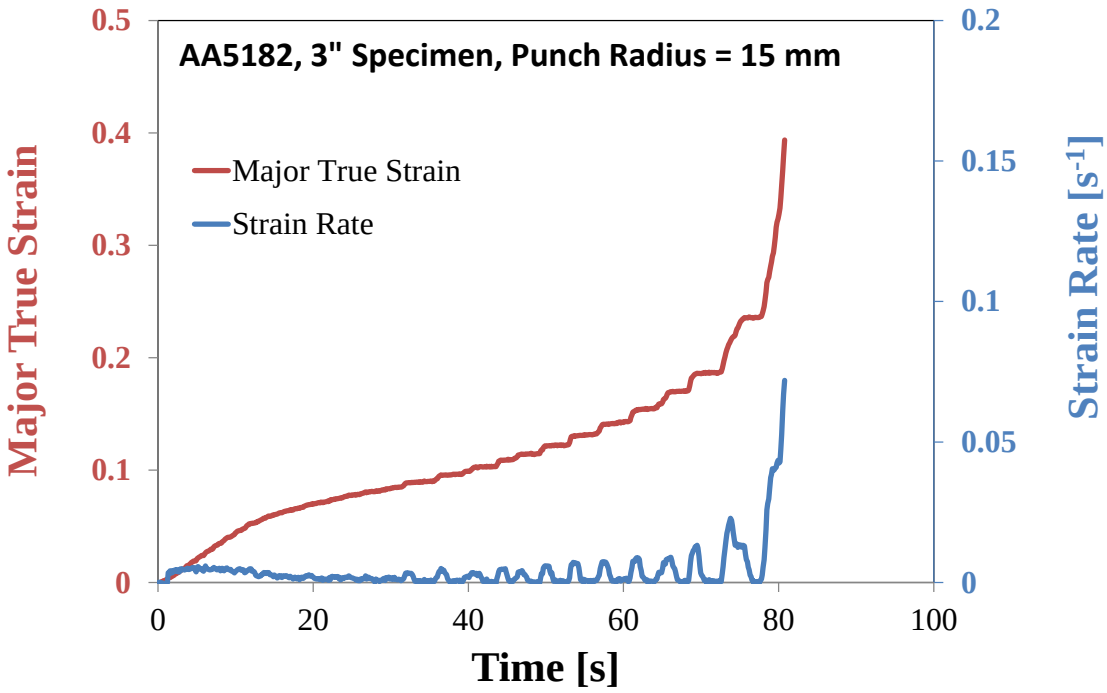

Figure 93 Major strain evolution and the corresponding strain rate of 3" wide AA5182 specimen using a 15 mm punch radius

6.4.1 Evidence of Localized Necking

During the DIC analysis, the evidence of local thinning was clearly observed. Both materials commonly showed that the stronger localization occurred by the wider specimen with the larger punch. The test results using 1" width subjected to 2 mm radius punch and 3" width subjected to 15 mm radius punch are presented in Figure 94 for comparison as these two test conditions were two extreme cases. At the end of the forming process, the stretching in the deformation becomes dominant and a clear sign of localization was visible in the center of the specimen, see Figure 95.

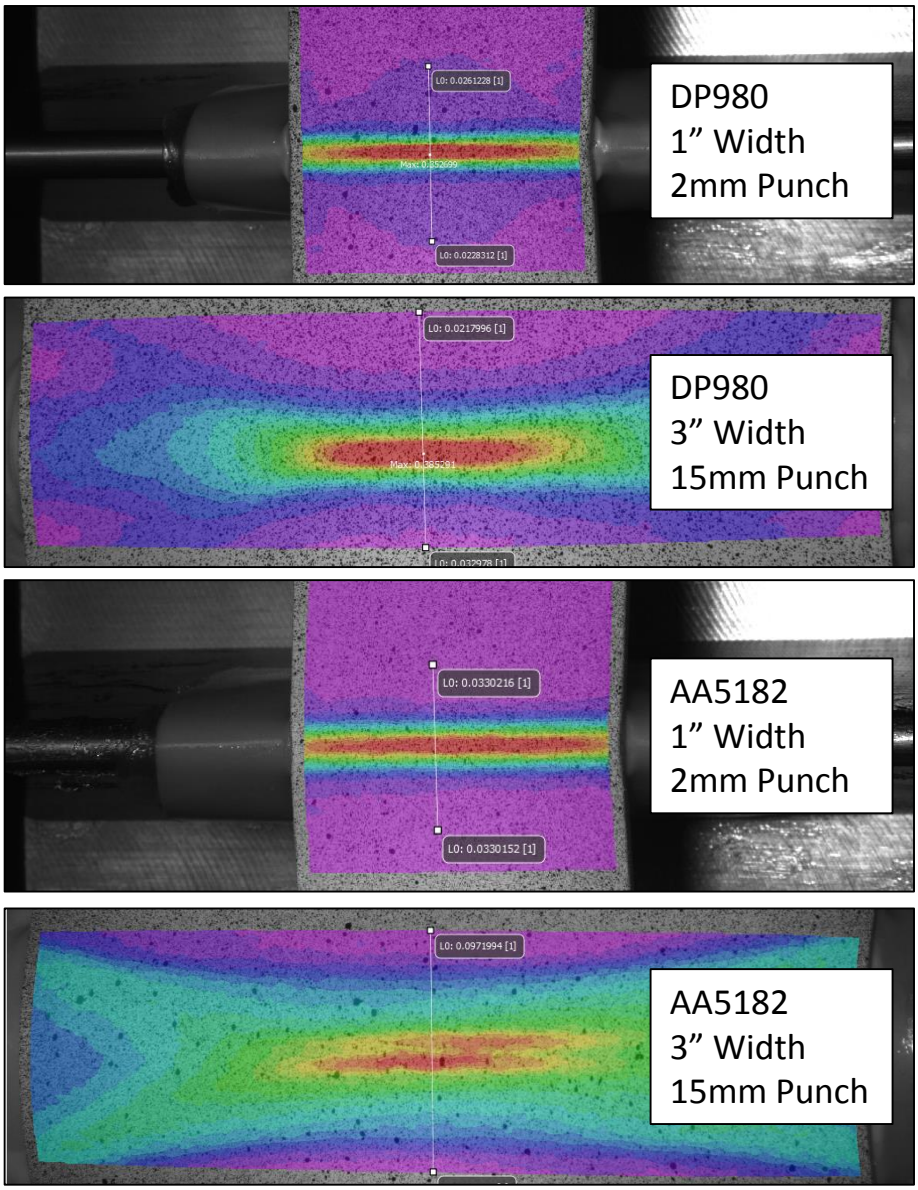

Figure 94 2D contour plot of major strain distribution of AA5182 specimen using 2mm radius punch with 1” specimen (top) and 15 mm radius punch with 3” specimen (bottom)

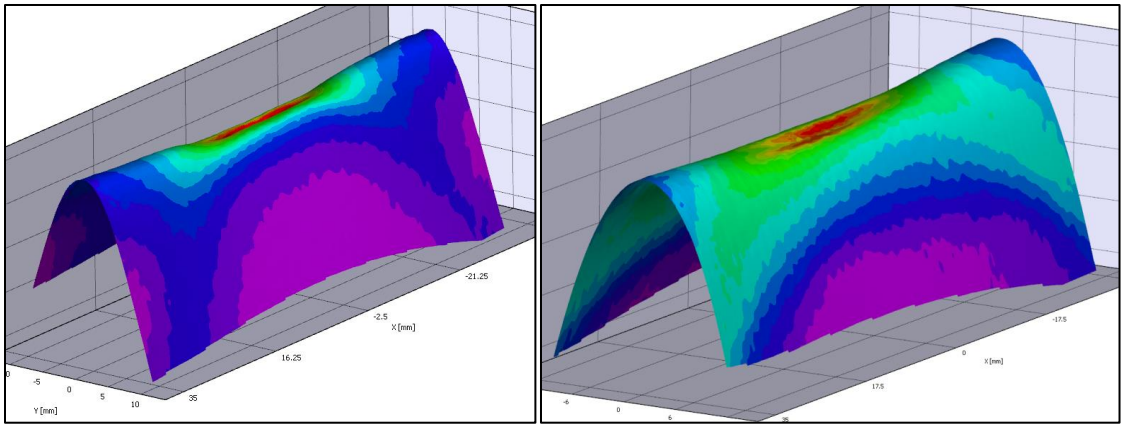

Figure 95 3D contour plot of major strain distribution of 3” specimens with 15 mm radius punch: DP980 (left) and AA5182 (right). The local thinning at the center of the specimen is clearly visible

6.5 Effect of Bend Severity under Stretch-Bending

The strain paths were measured at the peak major true strain location until the last recorded image before fracture over a circle with a radius of approximately 0.2 mm. The strain histories of each test condition are shown in Figure 96. For more intuitive visual comparison, identical major and minor strain scales were used. For both test materials, it can be seen that increasing the sample width and reducing the punch radius promotes plane strain deformation as the minor strain decreases. On the other hand, strain paths from the combination of 1” specimen and large punch tended to lean towards uniaxial stretching.

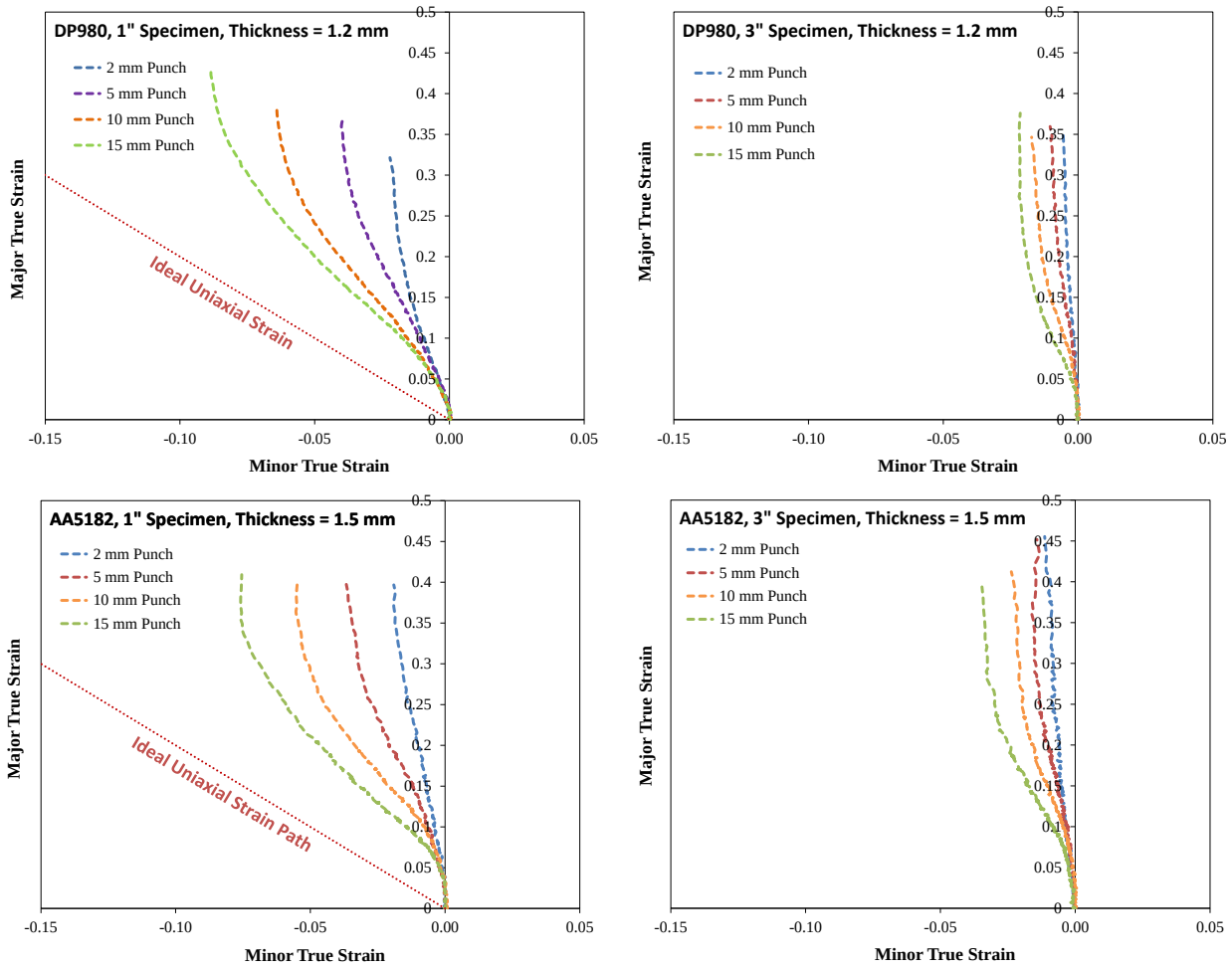

Figure 96 Evolution of the principal strains in the stretch-bend tests: DP980 specimens (top), AA5182 specimens (bottom), 1" specimens (left) and 3" specimens (right)

For both materials, the strain paths using 3" wide specimens showed relatively smaller deviation as the specimen geometry effectively restricted the test condition to be plane strain condition. On the other hand, the relationship between the bend severity and the strain development would be more visible in the test results using 1" wide specimens. An important observation to highlight is that each punch radius provided different strain-state. Similar to 3" wide specimen test results, the most severe bending with 2 mm radius punch provided a near plane strain condition even with the 1" wide specimen. However, the strain paths were gradually shifted toward the uniaxial strain condition since the effect of stretching became greater with the larger punch radius. This shift in strain path was a significant concern in the analysis as it resulted in multiple factors affecting the formability. As illustrated in Figure 97, smaller punches would

result in higher bend severity thus the formability was expected to be positively affected. In contrast, larger punches tended to have more uniaxial strain-state which naturally has higher formability than the plane strain. The competing effects of bend severity (delays necking) and strain path changes towards uniaxial tension (higher limit strains than plane strain) must be kept in mind when interpreting the results for the 1" wide test specimens.

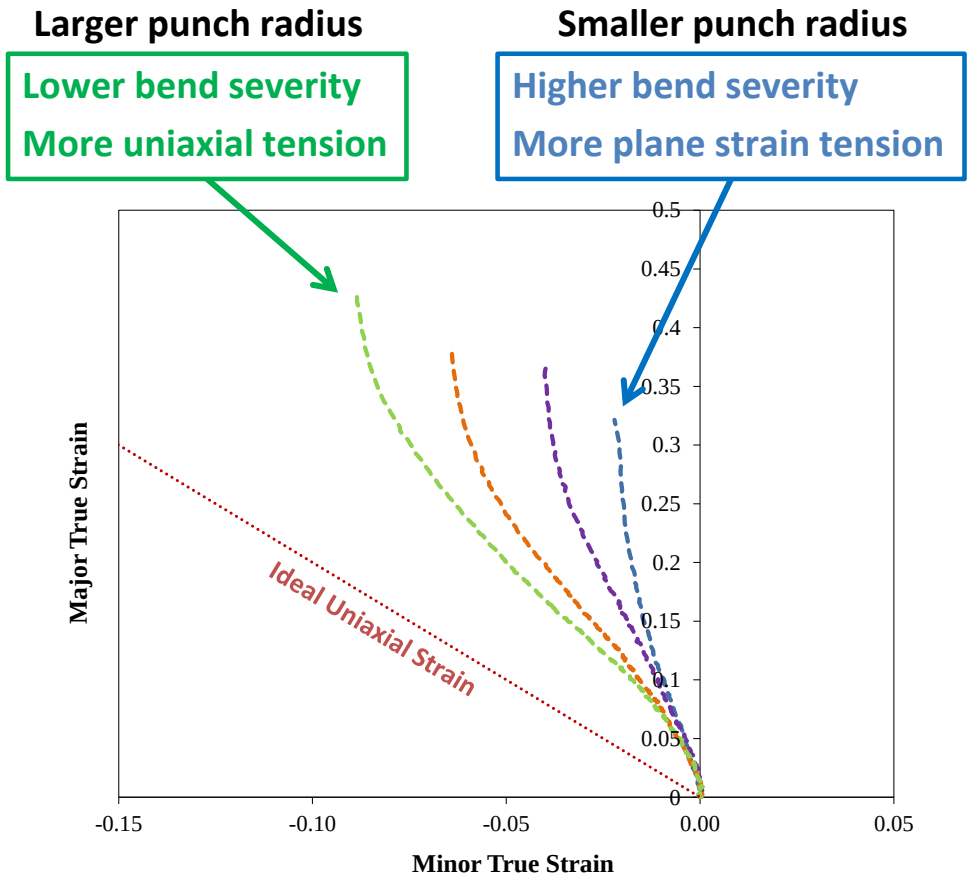

Figure 97 Strain history of 1" DP980 specimen. Two different factors are altering the formability

The limit strains of all test conditions were obtained using the time-dependent method introduced in Section 6.3. The result is summarized in Figure 98 and Figure 99. The equivalent forming limit strains of 1" specimens seemed to be independent of punch size. However, it is hard to draw a solid conclusion with this data since stress- and strain-states have been changed in 1" specimen test cases as punch radius changes. As mentioned in Figure 97, the influence of the change in bend severity and change in strain path were working against each other. The combined effect of these two factors was merged together and

not distinguishable. Fortunately, a more straightforward result was obtained from the tests using 3" specimens. Since the strain-state of 3" specimen tests were restricted to be near plane strain condition due to the test geometry, the correlation between the bend severity and the limit strain could be unveiled. On both materials, a positive influence of bend severity on limit strain was recorded. This result is in line with the bend severity analysis using the pure bending test that the necking was mitigated by the severe bending.

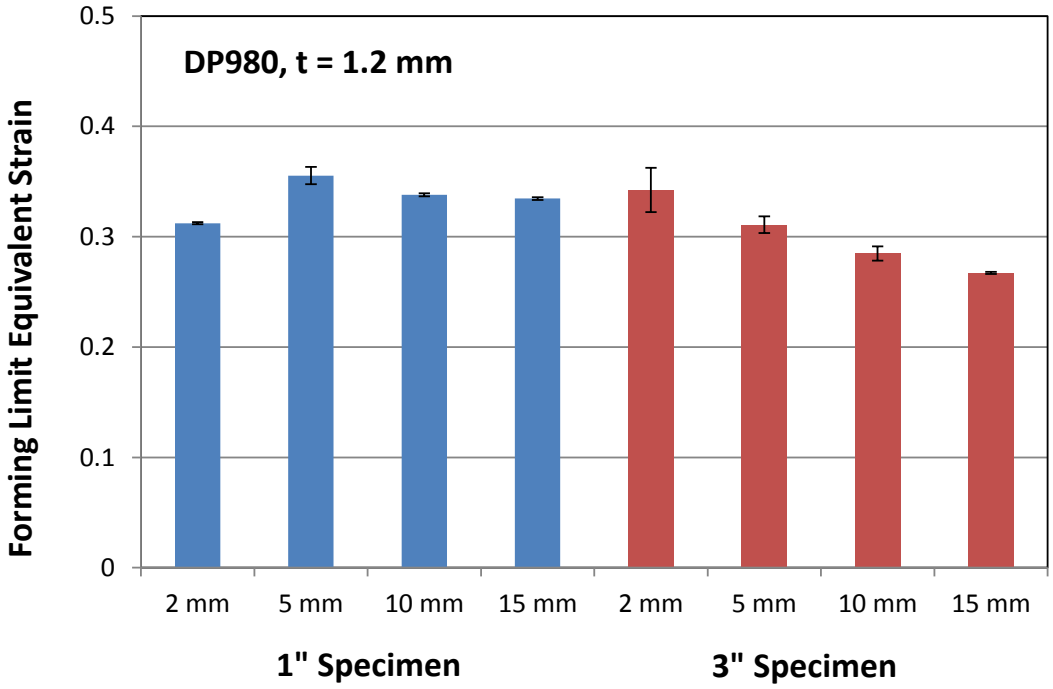

Figure 98 Summary of the forming limit of DP980 specimens using various sample width and punch tip radii

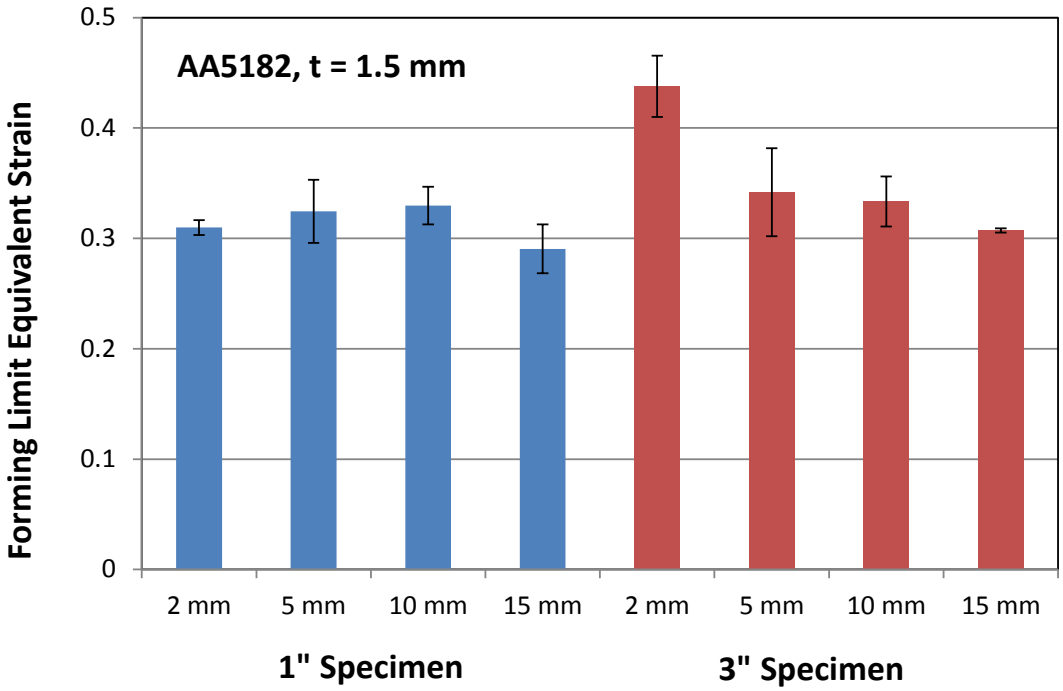

Figure 99 Summary of the forming limit of AA5182 specimens using various sample width and punch tips. The influence of bend severity is most apparent for the 3" specimen in which strain path changes were minimal.

6.6 Linearization of Strain Path

It is shown in Figure 96 that the strain evolution tended to become noticeably non-linear when the large punch radius was used on 1" wide specimens. As stated in Section 1.2, various literature have reported that the non-linearity on the strain path would significantly alter the forming behavior. Min *et al.* (2016) have investigated two different dome tests, Nakazima and Marciniak, and proposed a correction method to convert non-linear limit strains from Nakazima test into limit strains from Marciniak test. To avoid any potential ambiguity, the stretch-bend results were processed by Min's correction method to approximate linear limit strains. This method integrates the equivalent strain and stress from the DIC strain path under a von Mises assumption for the yield function. The equivalent strain at the limit strain and its corresponding strain state is then used to linearize the equivalent strain to obtain the major and minor strain components. The hardening law for each material described in Section 2.0 was used in the

linearization procedure. The results for DP980 are presented in Figure 100 and Figure 101. In the figure, hollow datapoints represent the experimental limit strains determined by the time-dependent method from Section 6.3 using non-linear strain path. On the other hand, the solid datapoints correspond to limit strains after linearization.

It was observed that all datapoints were shifted toward the major strain axis near plane strain condition by linearization. The datapoints also tended to slight shift downward since the plane strain condition has the most limited formability. The effect of linearization was more significant on 1" specimen tests than 3" specimen tests in which the strain paths were relatively linear already.

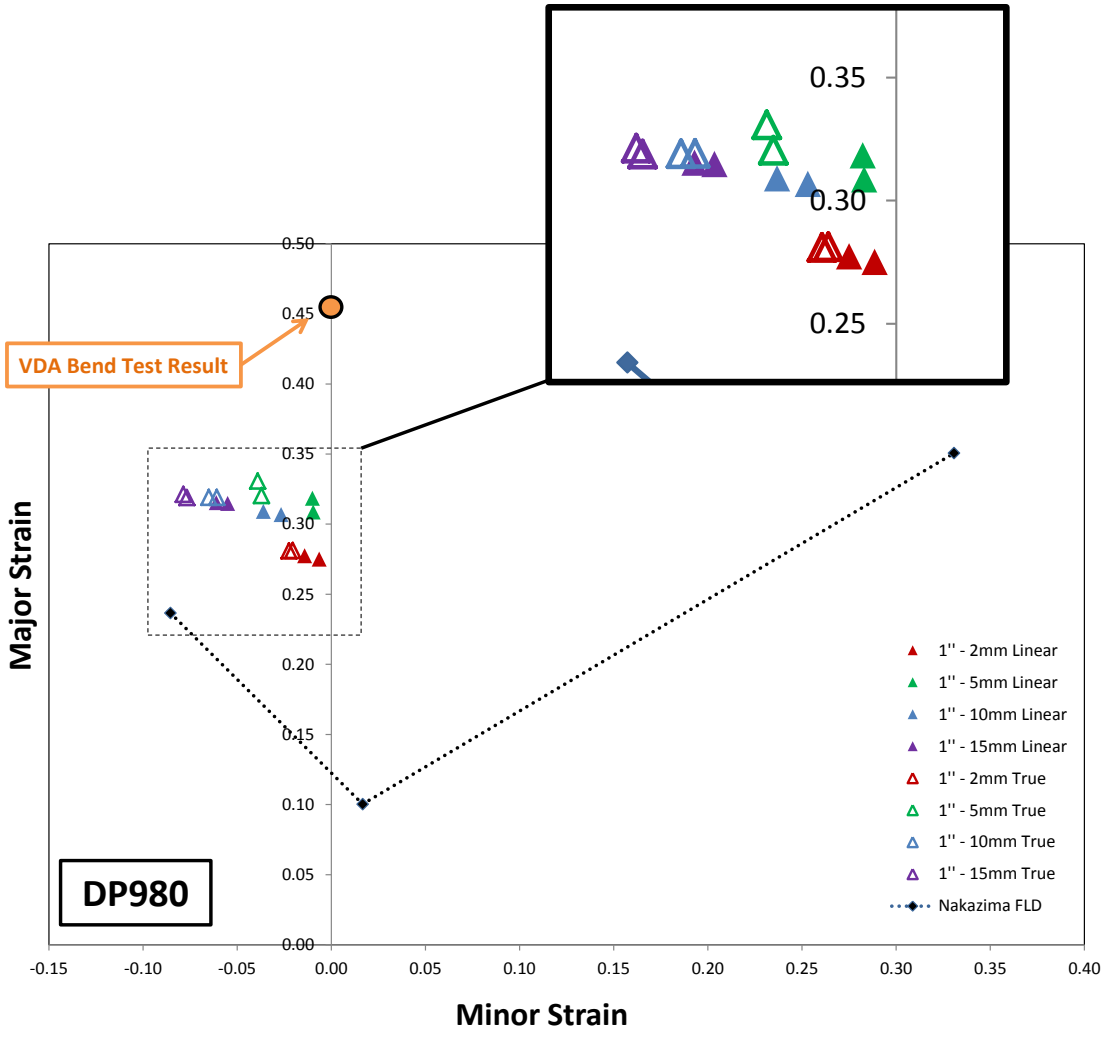

Figure 100 Illustration of limit strains of 1" DP980 specimens. Solid data points represent linearized limit strains and hollow data points represent experimental data

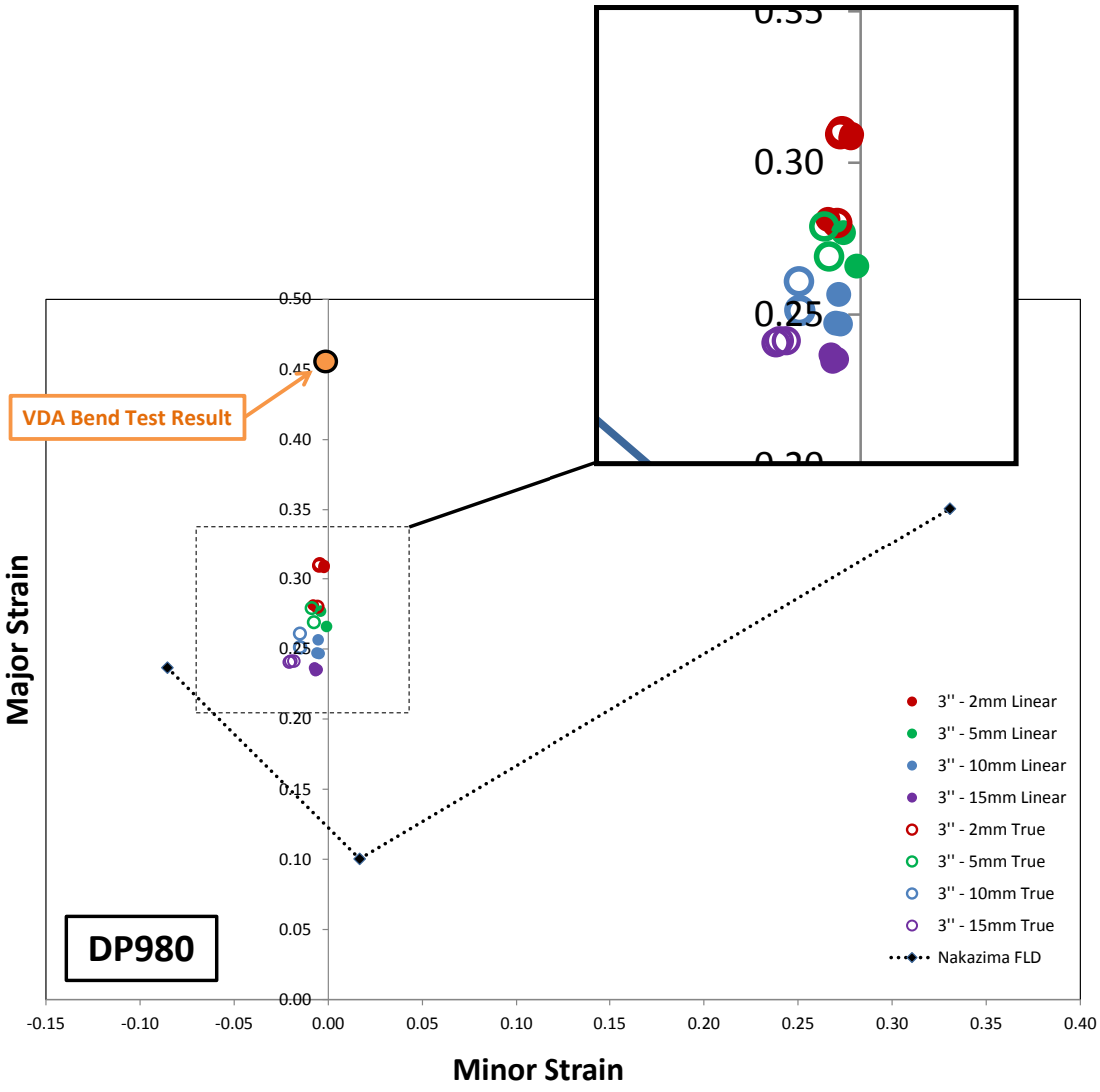

Figure 101 Illustration of limit strains of 3" DP980 specimens. Solid data points represent linearized limit strains and hollow data points represent experimental data

As shown in Figure 100 and Figure 101, the overall limit strain results were in line with conclusions from previous chapters. Especially, 3" specimen results clearly demonstrated that the curvature on deforming surface is positively influencing the forming performance of a material. Since the test setup was designed to apply combined stretching and bending deformation, the limit strains located in between two extreme cases; in-plane stretching from Nakazima and Marciniak test and pure bending fracture limit from bending. On the other hand, a direct comparison between 1" specimen results and VDA bend test result was not applicable since strain-state was still different even after linearization. However, it was observed that the stretch-bend result still followed the general trend of FLD.

A similar analysis was repeated using AA5182 specimens and the result is shown in Figure 102 and Figure 103. Overall behaviors were identical to the DP980 test results. Key observations such as the shift of linearized limit strains and improvement of formability with higher bend severity were also reported. Especially, a very strong dependence on the bend severity was revealed under approximately linear strain paths near plane strain using 3" specimens.

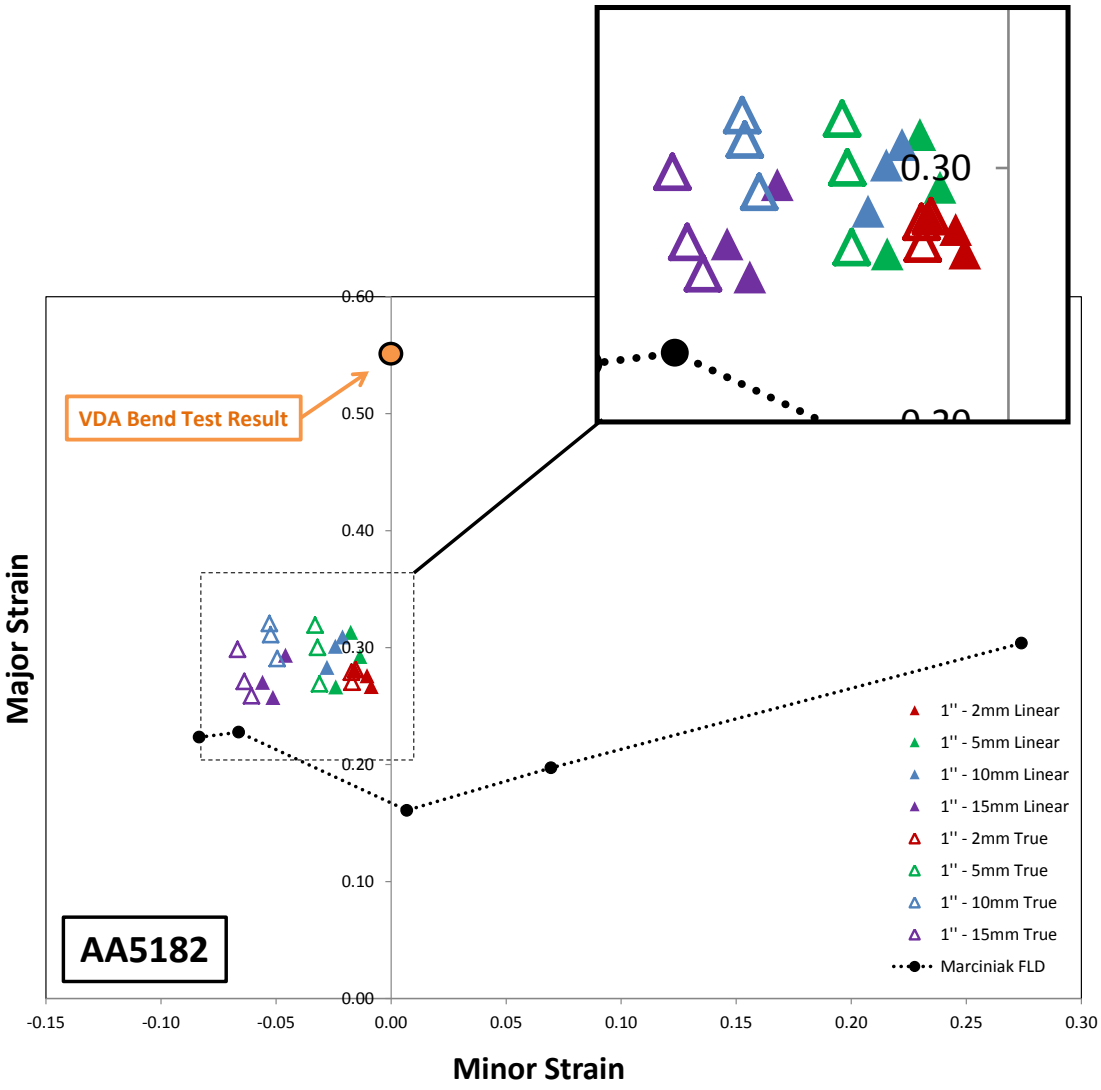

Figure 102 Illustration of limit strains of 1" AA5182 specimens. Solid data points represent linearized limit strains and hollow data points represent experimental data. The 5-point Marciniak FLD was provided by Jacqueline Noder (reference – private communication, 2019)

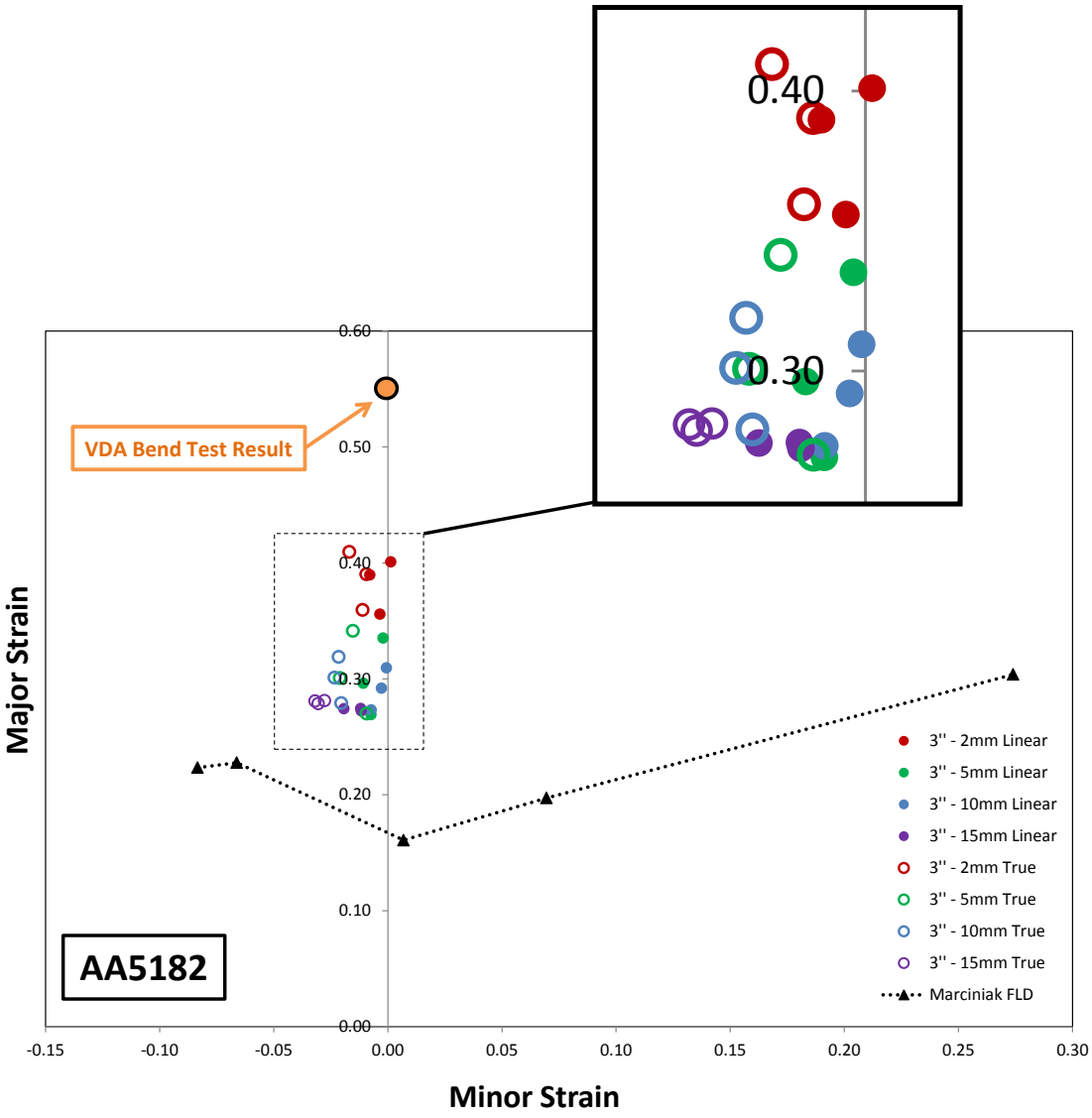

Figure 103 Illustration of limit strains of 3" AA5182 specimens. Solid data points represent linearized limit strains and hollow data points represent experimental data. The 5-point Marciniak FLD was provided by Jacqueline Noder (Private Conversation, 2019)

6.7 Summary of Stretch Bend Test Result

In this chapter, stretch-bend tests of DP980 and AA5182 were designed and investigated. This test design was intended to fill the significant gap between two extreme plane strain forming cases considered in this thesis: in-plane stretching and pure bending. Since bending was strongly involved in the test design, global approaches to limit strain determination such as ISO 12004-2 (2008) were not applicable. Instead,

local approach by Volk and Hora (2011) was employed to determine the limit strains based on time-dependent method. The findings from this chapter agreed with the main theme of this thesis which is the positive influence of the through-thickness strain gradient on the formability of sheet material. Similar to previous tests in this thesis, the stretch-bend test showed that the sharper punch radius with higher strain gradient tended to result in improvement of formability.

Moreover, many unique observations were also reported. The results identified the complexity of changing the strain path along with applying the through-thickness strain gradient. As a result, the combined effect of non-linear strain path and the change in bend severity experienced inconclusive results in which the gain in formability was muted. On the other hand, the change in path was minimal in 3" specimen test cases as the strain-state was constrained to remain in approximately plane strain due to the sample geometry. The influence of the bend severity was clearly revealed which coincided with the results from the VDA bend test.

Non-linear strain path corrections using the methodology of Min et al. (2016) were employed to interpret the result with the analytically linearized strain path so the result can be directly compared with the proportional strain data in the thesis. Since this test was designed to investigate the combined effect of bending and stretching, the limit strains from stretch-bending test varied within the range between in-plane stretching from FLC and pure bending from the v-bend test. Unfortunately, the ratio of stretching to bending could not be quantified. Inverse FEA is planned for future work which requires kinematic hardening since inner layers of material can experience a substantial transition from compression to tensile loading.

7.0 Traditional Formability Tests

The current definition of forming limit represents that materials can be formed under proportional loading conditions. However, the potential forming range beyond this in-plane conservative forming limit was discussed and investigated throughout this thesis with the help of through-thickness strain gradient. After out-of-plane deformation was analyzed under various stress-states, the collected data was integrated into the conventional FLD. For example, it was shown from the VDA bend test that materials could be formed up to its fracture limit under pure plane strain bending which represents the upper limit of the conditional forming range. As part of this research, representative traditional formability tests were also performed to obtain reference data to complete the analysis. Nakazima test was performed to construct the conventional FLC, and this data had been used throughout the thesis for comparison purposes. Moreover, the hole expansion test was performed to complete the draw side of the fracture limit curve. The analyzing method was based on studies of Butcher *et al*. (2013) and Pathak *et al*. (2017). Even though these test setups and procedures do not involve with significant novelty, these tests are included in this thesis in the context of formability analysis to construct the in-plane FLC and complete the fracture limit strain characterization under approximately proportional loading conditions.

7.1 Nakazima Dome Test

Nakazima test is the most common test method in the field of formability to investigate the formable range of a sheet metal. As it is widely used in both industry and academic, various literature are available and various aspects of this test setup have been studied by researchers. The Nakazima dome test was expected to provide a solid reference point to investigate and validate the novel approaches made in this thesis. Therefore, Nakazima test was selected to represent the traditional in-plane stretching test in which a severe localized necking is expected.

Two DP980 sheet materials with a thickness of 1.2 and 1.6 mm were manufactured into dogbone-shaped specimens with a width of 1" and 3" which are designed to experience uniaxial and plane strain loading condition. Moreover, an equi-biaxial specimen of 8" x 8" dimension was also prepared to construct the three-point FLD. These samples were subjected into the Nakazima dome tester with 100 mm diameter hemispherical punch and deformed until it fractured. The entire process was recorded and analyzed by DIC optical measurement to obtain *in-situ* surface strain measurement. Detailed specification of the test station and DIC can be found in Section 3.1 and 3.2.

The summarized results of Nakazima dome test using two DP980 steels are presented in Table 13 and the representative strain paths are illustrated in Figure 105 and Figure 105. The limit strains were estimated by the necking determining method from ISO 12004-2008 (2008). Based on fracture limit analysis in this thesis, the fracture limit strains obtained from the Nakazima test are suspect and should not be used without additional verification based upon post-mortem thickness measurements. Strain path corrections by Min *et al.* (2016) can be used to eliminate potential error due to non-linear strain path but is not required by ISO12004-2 (2008) and is not yet common practice. Moreover, thinning correction of Gorji *et al.* (2016) can be applied to estimate proper DIC fracture strain. However, none of these corrections were performed in the thesis since the primary objective of this test was to construct in-plane stretching FLD. The forming limit curves are illustrated in Figure 105 and Figure 105 as black solid lines.

Table 13 Summary of Nakazima dome test result using DP980 dogbone specimens

Test Setup	DP980, t = 1.2 mm		DP980, t = 1.6 mm	
	e1	e2	e1	e2
Uniaxial Dome	0.23 ± 0.0	- 0.08 ± 0.00	0.24 ± 0.02	- 0.09 ± 0.01
Plane Strain Dome	0.12 ± 0.01	0.02 ± 0.00	0.10 ±0.001	0.02 ± 0.00
Equi-biaxial Dome	0.36 ± 0.03	0.34 ± 0.03	0.35 ± 0.03	0.33 ± 0.03

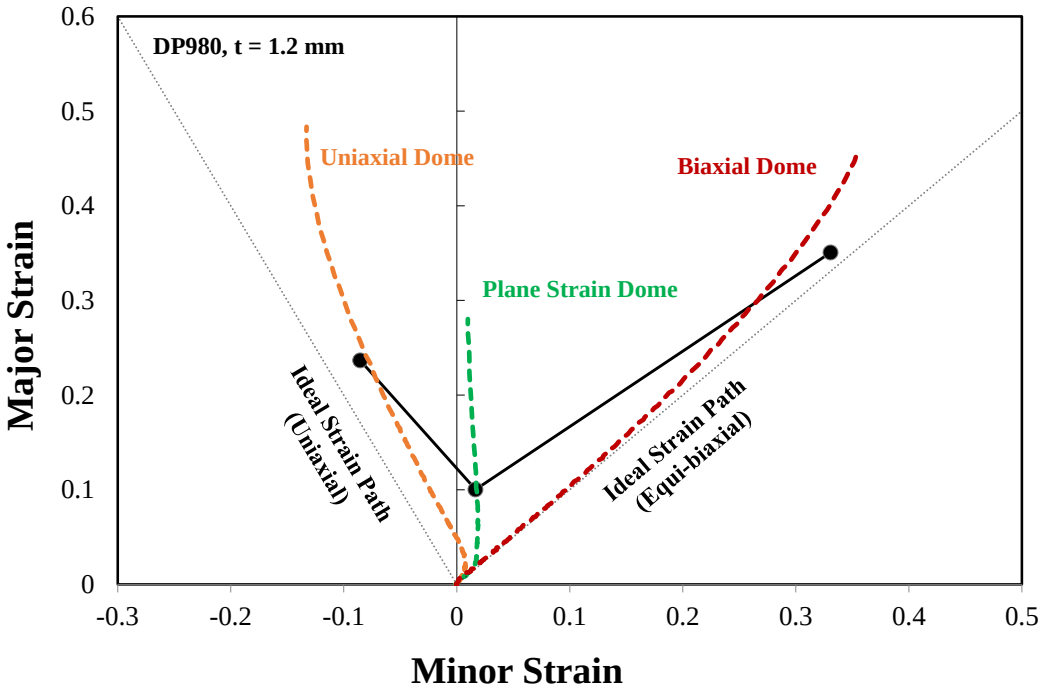

Figure 104 Forming limit diagram (FLD) of DP980 with a thickness of 1.2 mm using Nakazima dome test. The solid black line represents the forming limit curve (FLC)

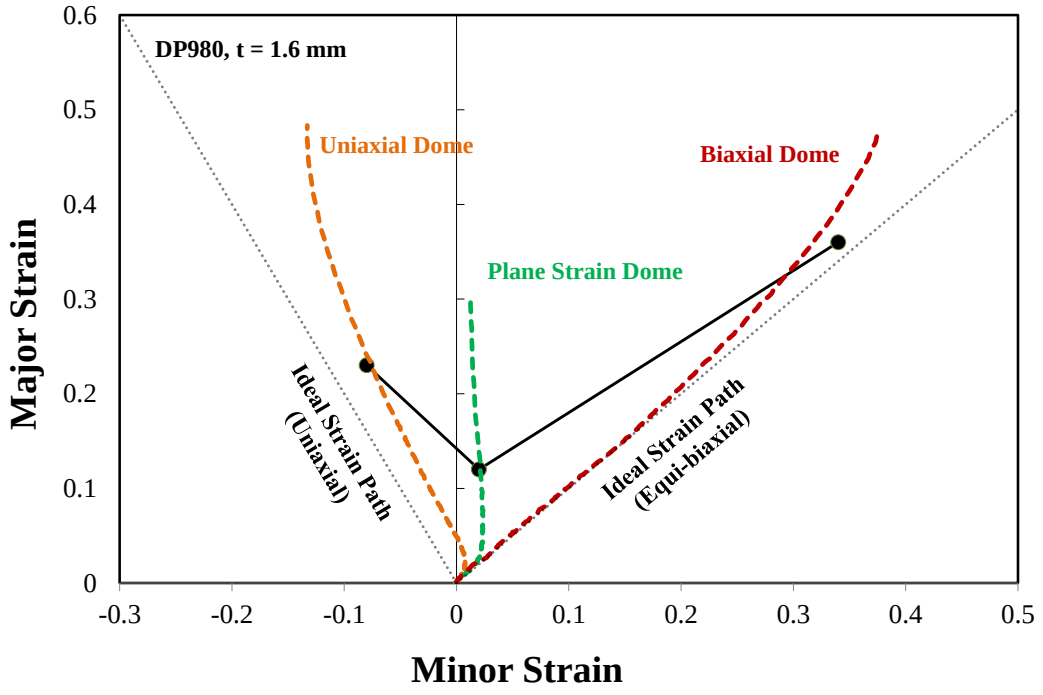

Figure 105 Forming limit diagram (FLD) of DP980 with a thickness of 1.6 mm using Nakazima dome test. The solid black line represents the forming limit curve (FLC)

7.2 Hole Expansion Test

A hole expansion test is a common method used to characterize the sheared edge formability of materials. In this thesis, the hole expansion test was performed to investigate the fracture behavior under uniaxial tension. Therefore, fracture behavior under three representative strain conditions which are uniaxial, plane strain, and biaxial stretching can be described by the hole expansion test, v-bend test, and miniature dome test respectively.

In the test setup from ISO 16630 standard (2009), a 10 mm diameter hole is punched at a prescribed clearance (12% typically) and then expanded until the first through-thickness crack occurs using a conical punch with an angle of 60˚. The general test setup is identical from the LDH test except for the shape of the punch as shown in Figure 106. A schematic of the test is shown in Figure 107.

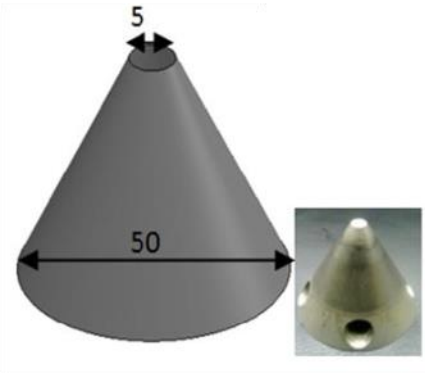

Figure 106 Shape of the conical punch used for the hole expansion test

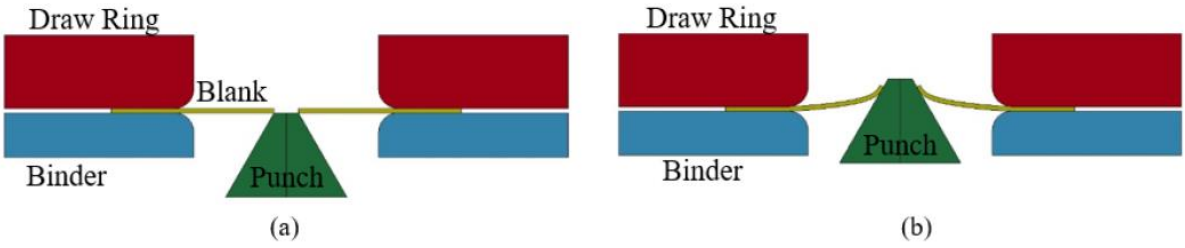

Figure 107 Schematic of the hole expansion process. The test continues until the through-thickness crack occurs

Since the scope of the current study is the fracture characterization of the material, the machined hole was employed instead of the sheared edge to eliminate the potential impact of the surface imperfection and the

residual strain field. The hole expansion specimen in this study consists of a square 8” x 8” blank which is identical to the equi-biaxial Nakazima test specimen but with a 10 mm central hole fabricated using CNC machining. Inner hole surface was lightly polished using sandpaper to ensure a smooth surface that helps to prevent cracks initiated by processing defects.

The acquired images from test were manually analyzed to identify the image when the first through-thickness crack appears. Following identification of the crack image, the commercial image analysis software, ImageProPlus®, was used to measure the inner and outer diameters of the specimens used best-fit circles. To reduce operator variability, a minimum of four different best-fit circles were used to measure the inner and outer diameters, and the average was reported. An example of the initial and fractured image for the test setup is presented in Figure 108 where a single through-thickness crack can be seen.

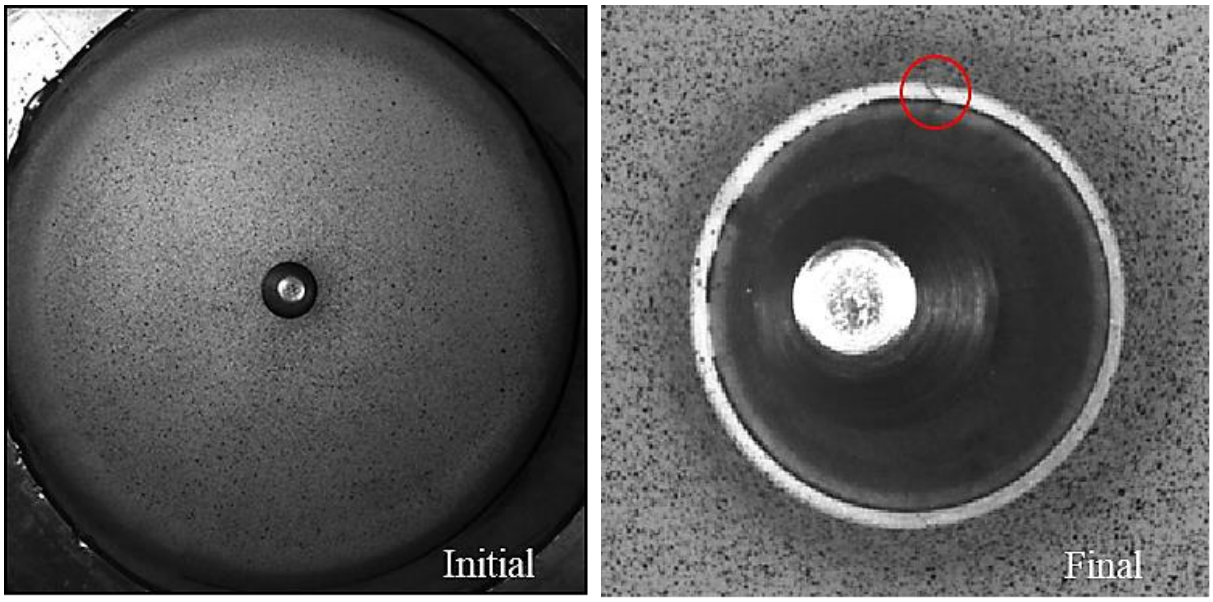

Figure 108 Recorded image of the initial (left) and the deformed (right) specimen. Due to the smooth inner surface, a single through-thickness crack was observed in most of the tests

The standard reporting metric for the hole expansion test is the hole expansion ratio (HER). The HER is the ratio of the inner hole diameter at fracture with respect to the initial inner diameter.

$$HER(\%) = 100 \cdot \left(\frac{d_{inner}^{f} - d_{o}}{d_{o}} \right) \tag{11}$$

However, as demonstrated in Butcher *et al*. (2013) and Pathak *et al*. (2017), the outer diameter of the expanding hole is free of any contact with the punch during the expansion process and is in a constant state of uniaxial tension due to the circumferential expansion. Due to the through-thickness stress gradient at the edge from compression to tension and the axisymmetric constraint due to circumferential stretching, tensile necking instabilities are suppressed until very large strains and thus fracture occurs at the outer edge which is the most severe stress state of constant uniaxial tension. The hole expansion test can therefore also be used for fracture characterization in approximately constant uniaxial tension without necking by measuring the outer diameter at the failure to obtain the major strain as Eq. (12). The stress state at the outer fiber is in approximately constant uniaxial tension and therefore the equivalent strain is equal to the major strain.

$$\varepsilon_{eq}^{f} \approx \varepsilon_{1}^{f} = \ln \left(\frac{d_{outer}^{f}}{d_{o}} \right) \tag{12}$$

In Table 14, the hole expansion ratios (HER) and the circumferential strains of DP980 steels and AA5182 specimens are summarized.

Table 14 Summarized result of DP980 and AA5182 hole expansion tests.

Material	**DP980 (t = 1.2)**	**DP980 (t = 1.6)**	**AA5182**
HER (%)	123	156	69
Von Mises Eq. Strain: ε_{eq}	0.84	0.99	0.64

7.3 Out-of-plane Fracture Limit Curve

With the analysis presented in this thesis, it was highlighted that conventional methods of fracture characterization might require additional correction process to provide a sufficient level of reliability. As an alternative solution, a new fracture limit curve based on proportional loading conditions has been proposed. As suggested from previous chapters, the hole expansion test, the VDA bend test, and the miniature dome test can be employed to represent true fracture limits of uniaxial, plane strain, and biaxial stretching condition respectively. The importance of this curve is that this is an effective forming limit curve under the out-of-plane deformation in which necking is suppressed. Based on the summary data from the traditional and novel formability tests in Table 15, a new form of FLD was developed which considers the effect of curvature when determining the feasibility of operation, see Figure 109. This novel fracture limit curve under curvature effect is illustrated as a dashed line.

Table 15 Summarized result of various formability tests for newly proposed proportional loading tests

Test Setup	DP980, t = 1.2 mm		DP980, t = 1.6 mm		AA5182, t = 1.5 mm	
	e1	e2	e1	e2	e1	e2
Hole Expansion Test	0.84	- 0.42	0.99	- 0.50	0.64	- 0.32
V-Bend Test	0.45	0.00	0.50	0.00	0.55	0.01
Miniature Dome Test	0.60	0.56	0.67	0.64	0.61	0.54

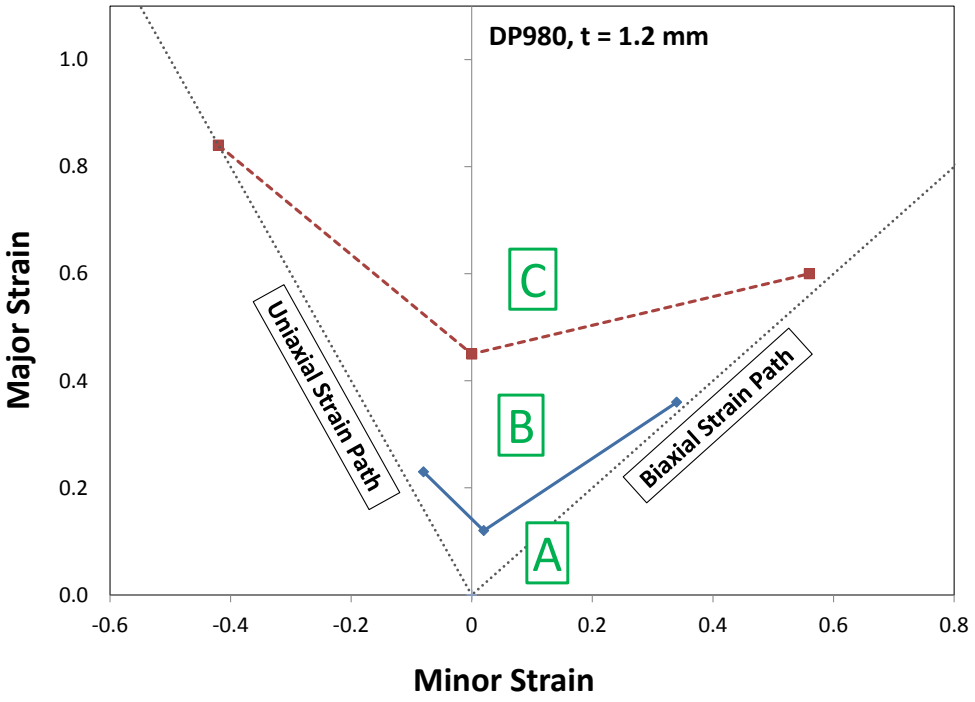

Figure 109 Illustration of three main regions of suggested FLD: (A) safe zone, (B) conditionally formable zone, and (C) Fracture zone

As investigated in Section 6.6 by using stretch-bending test, materials can be formed beyond the traditional forming limit (the solid line in Figure 109) if sufficient amount of through-thickness strain is presented. Therefore, the final shape of the suggested FLD with the novel fracture limit curve would be divided into three regions: (A) the area under the conventional forming limit curve where material is safe, (B) where material can be formed conditionally depending upon the bend severity, and (C) where material is expected to be fracture, see Figure 109. A similar analysis was performed to another DP980 and AA5182 sheets and the results are illustrated in Figure 110 and Figure 111.

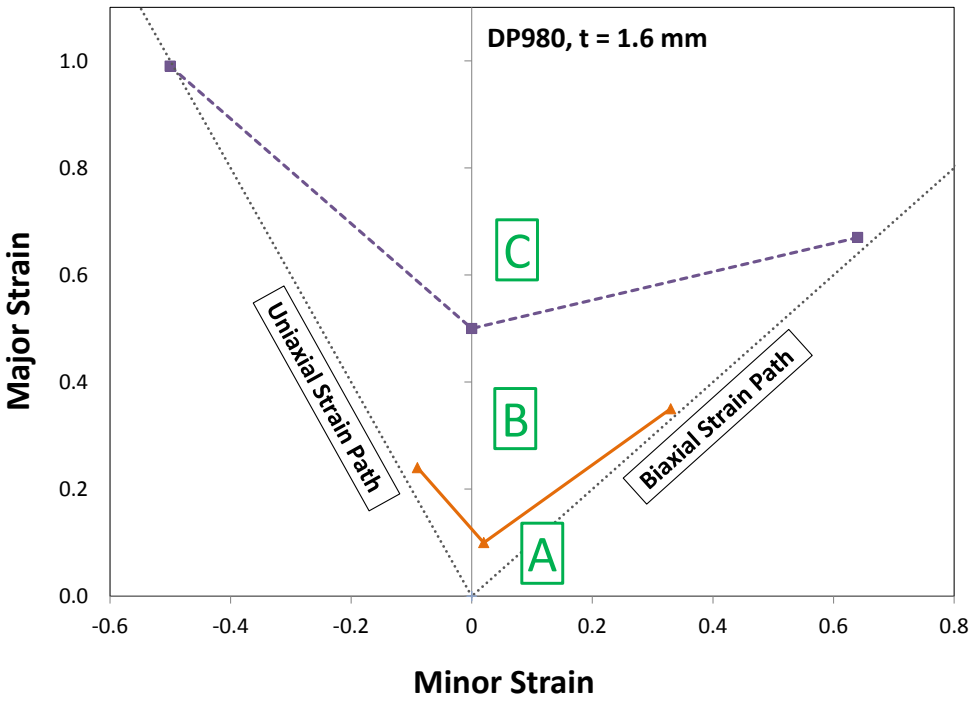

Figure 110 Illustration of proposed form of FLD including out-of-plane fracture curve using DP980 with a thickness of 1.6 mm

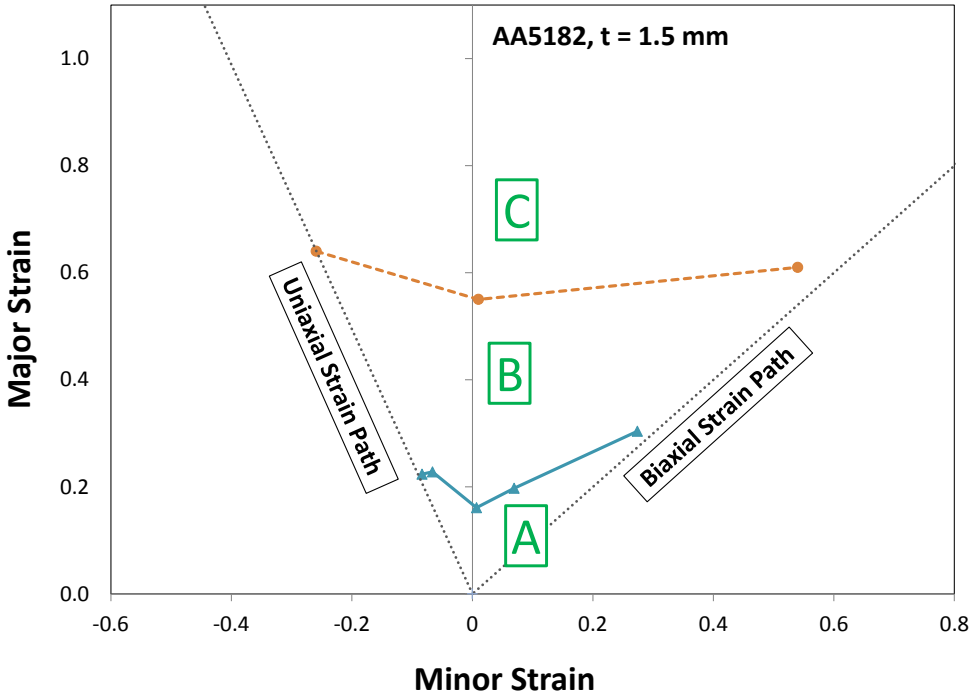

Figure 111 Illustration of proposed form of FLD including out-of-plane fracture curve using AA5182. The 5-point Marciniak FLD was provided by Jacqueline Noder (reference – private communication, 2019)

As mentioned in Chapter 6, the forming operation in the actual production commonly experiences a combination of bending and stretching. In such deformation mode, the forming limit is expected to be improved by curvature but lower than pure bending. As shown in Figure 112, stretching bend result would vary within the range (B). Therefore, by knowing how much bending would be involved in the operation, the precise forming limit can be customized for each forming process.

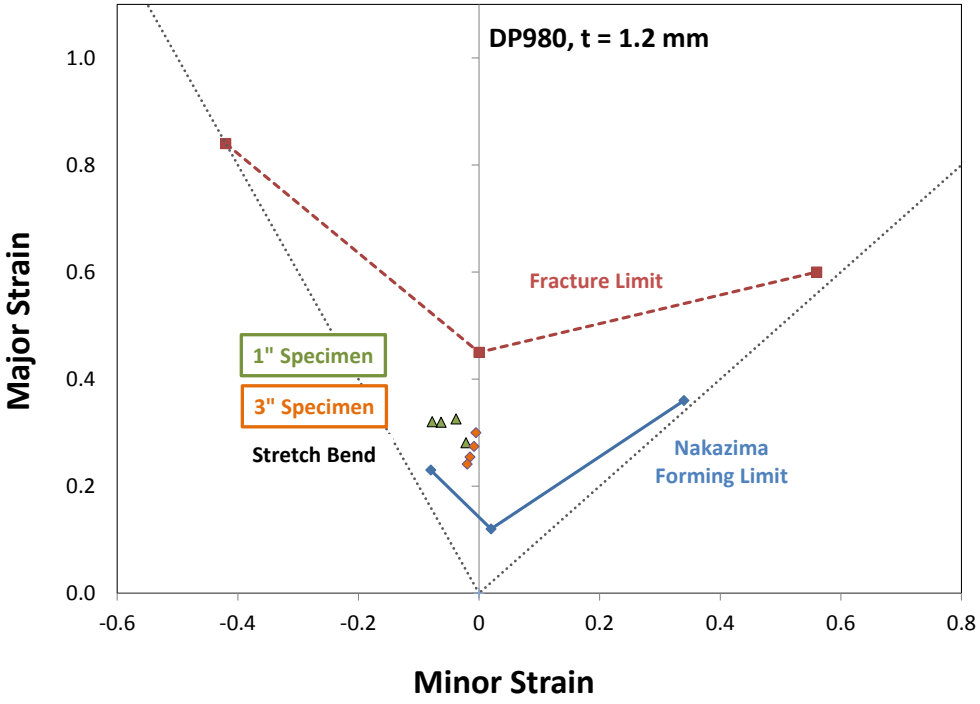

Figure 112 Illustration of FLD with limit strains from the stretch-bend test of DP980. All data points have different test conditions in terms of specimen width and punch radii.

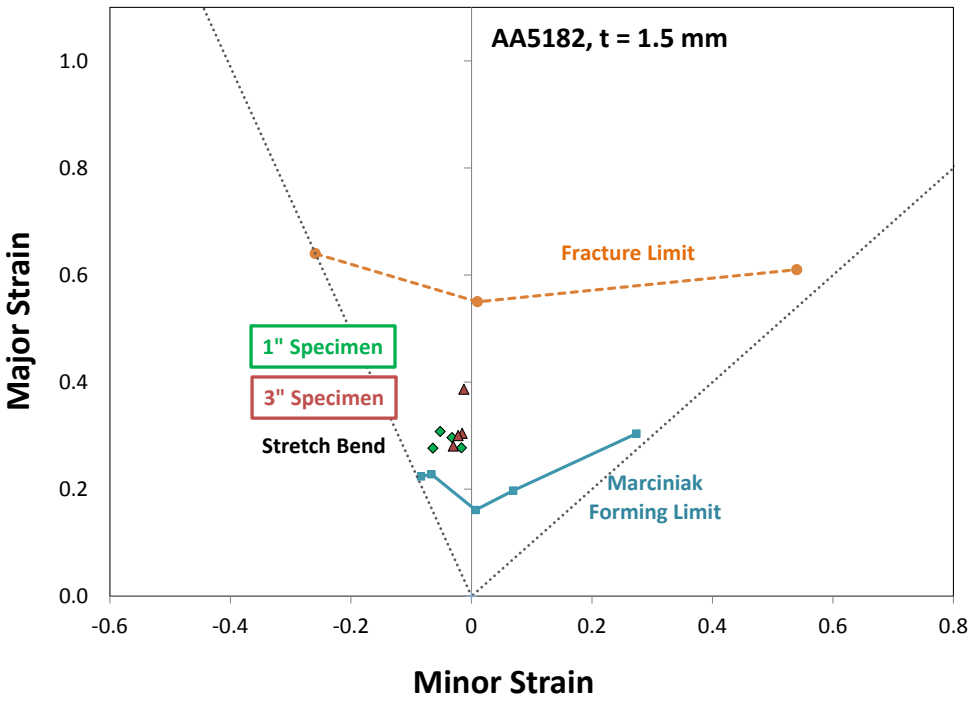

Figure 113 Illustration of FLD with limit strains from the stretch-bend test of AA5182. All data points have different test conditions in terms of specimen width and punch radii. The 5-point Marciniak FLD was provided by Jacqueline Noder (reference – private communication)

8.0 Conclusion

Throughout the thesis, various aspects of material formability were investigated. The emphasis was put on the influence of through-thickness strain gradient often generated by the out-of-plane deformation. Even though it is practically known that the bending on the deforming surface has a positive impact on material formability, current techniques used for experimental formability characterization are still relying on in-plane stretching. To investigate and characterize the influence of curvature on deformation, novel test designs were developed and corresponding test procedures and standards were constructed. Digital Image Correlation (DIC) technique was employed to obtain the *in-situ* surface measurement. Identical post-processing parameters were used throughout the research to prevent any potential DIC confusion. Approximated VSGL of 0.5 mm was used commonly as a fair trade-off between the accuracy and the computational resource.

The overall investigation showed a common conclusion that the presence of through-thickness strain gradient suppresses the strain instability, or simply necking. Since the conventional Forming Limit Diagram (FLD) is solely determined by the onset of necking, the delay in localization can directly translate into the improvement in formability.

Main research findings from this thesis can be stated as:

- It was evaluated that VDA 238-100 bend test criteria provided a reasonable estimation of bending behavior. The load threshold method can be used as the initial estimation to approximate the onset of cracking but the accuracy might vary depending on the material and application. Theoretical bend angle calculation proposed by VDA 238-100 showed a remarkable accuracy whereas the correlation from ISO 7438 tended to overestimate the bend angle with a large bending

- The concept of using punch displacement and theoretical bend angle has fundamental limitations, thus use of DIC optical measurement is strongly recommended. With the addition of DIC, it was verified that the v-bend test specimen is under pure bending with a plane strain condition as designed. The strain instability was suppressed by strong through-thickness strain gradient. No evidence of necking was observed throughout the process thus the fracture limit becomes the effective forming limit.

- Major strain development under bending was observed to have a common characteristic trend as initial non-linear strain development followed by linear development until the fracture. Based on both theoretical and experimental approaches, the slope of linear strain evolution was found to be a function of bend severity. Since the fracture limit is a material constant, the fracture bend angle was observed to be dependent on the bend severity. The smaller bend radius with the higher bend severity showed the steeper slope which means that the fracture strain can be achieved with a lower bend angle.

- A method to mathematically normalize the experimental strain was developed. This normalized strain correlation is independent of bend severity. Then the theoretical adjustment of bend severity can be performed by this method to estimate the forming behavior under various bend radii and sheet thicknesses without additional experiments.

- After the significant effect of curvature under plane strain was investigated by VDA bend test, a similar approach was applied to equi-biaxial stretching test using two DP980 steels and AA5182 sheets. Multiple hemispherical dome punches with small radii were manufactured to introduce the severe bending condition within a Nakazima test setup. The key findings from the VDA bend test were also observed from the miniature dome test again. For example, the mitigation of necking also occurred as the punch radius gets smaller. The strain paths were linearized and remained near ideal equi-biaxial strain-state as severe bending was applied. A remarkable improvement on

fracture strain was also observed as the necking is suppressed and the strain path is linearized. With the punch radius of 5 mm, a near-perfect equi-biaxial strain-state was achieved.

- In the context of completing the analysis of formability under various stress-states from stretching to bending, the stretch-bend test was proposed to investigate the combined effect of bending and stretching under near plane strain condition. In contrast to the bend test, the strain history tended to be non-linear by the effect of stretching thus a linearization method by Min and Stoughton (2016) was applied to refine the test result. The stretch bend result was in line with the findings from VDA bend test such as the positive correlation between the bend severity and material formability. The limit strains from various stretch bend tests were located between the VDA bend test and Nakazima test result as these are two representative test setups for pure bending and in-plane stretching respectively.

- In addition to novel test designs, traditional tests such as the Nakazima test and hole expansion test were performed for the completeness of the research. The Nakazima test was employed to provide a conservative forming limit under in-plane stretching. A brief investigation on uniaxial strain-state formability was performed using the hole expansion test. From the collected result throughout the thesis, a new form of FLD was proposed which has an out-of-plane fracture limit curve from proportional loading conditions in addition to the conventional in-plane forming limit curve. This proposed FLD is designed to account the effect of bending when it determines the feasibility of operation. Therefore, each forming operation could have a customized FLD depending on the amount of bending involved in the process.

9.0 Recommendations

1. The fracture identification of VDA bend test still has room for improvement. In this thesis, the visual approach was attempted but the result was not impressive and time-consuming. The traditional load threshold method can provide an acceptable level of accuracy but the more objective and intuitive method is certainly desirable. Other approaches such as the usage of image processing software to trace the crack opening or time-dependent strain rate approach can be attempted.

2. Since the VDA load threshold only concerns about the peak load point, the load behavior after the peak load is often neglected. However, it was observed that the post-crack load behavior is very distinguishable between materials. For example, HS1500 tended to experience a rapid reduction in the load after reaching its peak load, whereas the load curves of DP steels tended to remain fairly flat even after the peak load. Therefore, the post-crack material data from v-bend could be useful to investigate the material crack resistivity that will aid in the selection of materials for crash applications.

3. Currently, stretch-bending tools are implemented in the MTS dome tester which has a wide opening with 100 mm in diameter. This geometry was observed to be overly wide for stretch-bend analysis as the portion of stretching easily overwhelms the bending. A customized station for stretch-bend is recommended for a better balance between the bending and stretching.

4. At the end of this thesis, a customized FLD depending on the stress-state was proposed. However, the analysis of the current study cannot differentiate or quantify the effect of bending and stretching. Inverse finite element analysis (FEA) would be required for future work to separately investigate the effect of bending and stretching under stretch-bending stress-state. Moreover, the current results are expected to be under the effect of contact pressure which can also be investigated via inverse FEA.

References

Aretz, H., 2007. Numerical analysis of diffuse and localized necking in orthotropic sheet metals. *International Journal of Plasticity*, 23(5), pp.798-840.

Arrieux, R., Bedrin, C. and Boivin, M., 1982, May. Determination of an intrinsic forming limit stress diagram for isotropic sheets. *In Proceedings of the 12th IDDRG Congress* (Vol. 2, pp. 61-71).

Bai, Y. and Wierzbicki, T., 2010. Application of extended Mohr–Coulomb criterion to ductile fracture. *International Journal of Fracture*, 161(1), p.1.

Barlat, F., 1987. Crystallographic texture, anisotropic yield surfaces and forming limits of sheet metals. *Materials Science and Engineering*, 91, pp.55-72.

Butcher, C., Anderson, D. and Worswick, M., 2013. Predicting failure during sheared edge stretching using a damage-based model for the shear-affected zone. *SAE International Journal of Materials and Manufacturing*, 6(2), pp.304-312.

Centeno, G., Bagudanch, I., Martínez-Donaire, A.J., Garcia-Romeu, M.L. and Vallellano, C., 2014. Critical analysis of necking and fracture limit strains and forming forces in single-point incremental forming. *Materials & Design*, 63, pp.20-29.

Cheong, K., Omer, K., Butcher, C., George, R. and Dykeman, J., 2017, September. Evaluation of the VDA 238-100 Tight Radius Bending Test using Digital Image Correlation Strain Measurement. *In Journal of Physics: Conference Series (Vol. 896, No. 1, p. 012075)*. IOP Publishing.

Chu, X., Leotoing, L., Guines, D. and Ragneau, E., 2014. Temperature and strain rate influence on AA5086 Forming Limit Curves: Experimental results and discussion on the validity of the MK model. *International Journal of Mechanical Sciences*, 78, pp.27-34.

Considère, M., 1885. Memoire sur l'emploi du fer et de l'acier dans les constructions. Dunod.

Dicecco, S., Butcher, C., Worswick, M., Boettcher, E., Chu, E. and Shi, C., 2016, November. Determination of forming limit diagrams of AA6013-T6 aluminum alloy sheet using a time and position dependent localized necking criterion. *In IOP Conference Series: Materials Science and Engineering* (Vol. 159, No. 1, p. 012009). IOP Publishing.

Dunand, M. and Mohr, D., 2010. Hybrid experimental–numerical analysis of basic ductile fracture experiments for sheet metals. *International journal of solids and structures*, 47(9), pp.1130-1143.

Dykeman, J., Hoydick, D., Link, T. and Mitsuji, H., 2009. Material property and formability characterization of various types of high strength dual phase steel (No. 2009-01-0794). *SAE Technical Paper*.

Effelsberg, J., Haufe, A., Feucht, M., Neukamm, F. and Du Bois, P., 2012, June. On parameter identification for the GISSMO damage model. In *12th International LS-DYNA® Users Conference*, Dearborn, MI, USA.

El-Domiaty, A.A., Shabara, M.A.N. and Al-Ansary, M.D., 1996. Determination of stretch-bendability of sheet metals. *The International Journal of Advanced Manufacturing Technology*, 12(3), pp.207-220.

George, R., 2011. Hot Forming of Boron Steels with Tailored Mechanical Properties: Experiments and Numerical Simulations. *UWSpace*. http://hdl.handle.net/10012/5927

Ghosh, A.K. and Hecker, S.S., 1974. Stretching limits in sheet metals: in-plane versus out-of-plane deformation. *Metallurgical Transactions*, 5(10), pp.2161-2164.

Goodwin, G.M., 1968. Application of strain analysis to sheet metal forming problems in the press shop. *SAE Transactions*, pp.380-387.

Gorji, M., Berisha, B., Hora, P. and Barlat, F., 2016. Modeling of localization and fracture phenomena in strain and stress space for sheet metal forming. *International Journal of Material Forming*, 9(5), pp.573-584.

Graf, A. and Hosford, W.F., 1994. The influence of strain-path changes on forming limit diagrams of A1 6111 T4. *International Journal of Mechanical Sciences*, 36(10): 897-910.

Haddad, A., Arrieux, R. and Vacher, P., 2000. Use of two behaviour laws for the determination of the forming-limit stress diagram of a thin steel sheet: results and comparisons. *Journal of Materials Processing Technology*, 106(1-3), pp.49-53.

Halim, H., Wilkinson, D.S. and Niewczas, M., 2007. The Portevin–Le Chatelier (PLC) effect and shear band formation in an AA5754 alloy. *Acta Materialia*, 55(12), pp.4151-4160.

Hance, B.M., 2016, September. Advanced High Strength Steel: Deciphering Local and Global Formability. In Proc. *International Automotive Body Congress (IABC 2016)*, Dearborn, MI (pp. 28-29).

Hill, R., 1998. The mathematical theory of plasticity (Vol. 11). *Oxford university press*.

Hill, R.T., 1952. On discontinuous plastic states, with special reference to localized necking in thin sheets. *Journal of the Mechanics and Physics of Solids*, 1(1), pp.19-30.

Hotz, W., Merklein, M., Kuppert, A., Friebe, H. and Klein, M., 2013. Time dependent FLC determination comparison of different algorithms to detect the onset of unstable necking before fracture. *In Key Engineering Materials* (Vol. 549, pp. 397-404). Trans Tech Publications.

Hutchinson, J.W. and Neale, K.W., 1977. Influence of strain-rate sensitivity on necking under uniaxial tension. *Acta Metallurgica*, 25(8), pp.839-846.

ISO 12004-2: 2008, 2008. Metallic Materials–sheet and strip–determination of forming-limit curves–part 2: determination of forming-limit curves in the laboratory. *ISO*, 1, pp.1-27.

ISO 16630, 2009. Metallic materials - Sheet and strip - Hole expanding test

ISO, B., 2005. 7438: 2005 (E), Metallic Materials, Bend test. *London: British Standards Institution*.

ISO, P., 20482: 2004. Metallic materials-Sheet and strip-Erichsen Cupping test method

Keeler, S.P. and Backofen, W.A., 1963. Plastic instability and fracture in sheets stretched over rigid punches. *Asm Trans Q*, 56(1), pp.25-48.

Keeler, S.P., 1968. Circular grid system—a valuable aid for evaluating sheet metal formability. *SAE Transactions*, pp.371-379.

Kitting, D., Ofenheimer, A., Pauli, H. and Till, E.T., 2011, May. Experimental Characterization of Stretch-Bending Formability of AHSS Sheets. *In AIP conference Proceedings* (Vol. 1353, No. 1, pp. 1589-1594). AIP.

Kleemola, H.J. and Pelkkikangas, M.T., 1977. Effect of predeformation and strain path on the forming limits of steel, copper and brass. *Sheet Met Ind*, 64(6), pp.591-592.

Kortenaar, L., 2016. Failure Characterization of Hot Formed Boron Steels with Tailored Mechanical Properties. *UWSpace*. http://hdl.handle.net/10012/10351

Kuroda, M. and Tvergaard, V., 2000. Forming limit diagrams for anisotropic metal sheets with different yield criteria. *International Journal of Solids and Structures*, 37(37), pp.5037-5059.

Larour, P., Hackl, B. and Leomann, F., 2013. Sensitivity analysis on the calculated bending angle in the instrumented bending test. In *Proc. Int. Conf. IDDRG* (pp. 02-05).

Larour, P., Hackl, B., Leomann, F. and Benedyk, K., 2012. Bending angle calculation in the instrumented three-point bending test. In *Proceedings of the IDDRG* (pp. 25-29).

Leu, D.K., 1997. A simplified approach for evaluating bendability and springback in plastic bending of anisotropic sheet metals. *Journal of Materials Processing Technology*, 66(1-3), pp.9-17.

Link, T.M. and Chen, G., 2013. Anisotropy Effects in the Axial Crash Behavior of Advanced High-Strength Steels. Assoc. *Iron Steel Technol*, pp.63-70.

Link, T.M., 2008. Effects of Paint Baking on the Axial Crash Performance of Advanced High Strength Steels. *Materials Science & Technology*.

Marciniak, Z. and Kuczyński, K., 1967. Limit strains in the processes of stretch-forming sheet metal. *International journal of mechanical sciences*, 9(9), pp.609-620.

Marciniak, Z., Kuczyński, K. and Pokora, T., 1973. Influence of the plastic properties of a material on the forming limit diagram for sheet metal in tension. *International Journal of Mechanical Sciences*, 15(10), pp.789-800.

Martínez-Donaire, A.J., García-Lomas, F.J. and Vallellano, C., 2014. New approaches to detect the onset of localised necking in sheets under through-thickness strain gradients. *Materials & Design*, 57, pp.135-145.

Merklein, M., Kuppert, A. and Geiger, M., 2010. Time dependent determination of forming limit diagrams. *CIRP annals*, 59(1), pp.295-298.

Min, J., Stoughton, T.B., Carsley, J.E. and Lin, J., 2016. Compensation for process-dependent effects in the determination of localized necking limits. *International Journal of Mechanical Sciences*, 117, pp.115-134.

Min, J., Stoughton, T.B., Carsley, J.E. and Lin, J., 2017. A method of detecting the onset of localized necking based on surface geometry measurements. *Experimental Mechanics*, *57*(4), pp.521-535.

Min, J., Stoughton, T.B., Carsley, J.E. and Lin, J., 2017. An improved curvature method of detecting the onset of localized necking in Marciniak tests and its extension to Nakazima tests. *International Journal of Mechanical Sciences*, 123, pp.238-252.

Morales-Palma, D., Vallellano, C. and García-Lomas, F.J., 2013. Assessment of the effect of the through-thickness strain/stress gradient on the formability of stretch-bend metal sheets. *Materials & Design*, 50, pp.798-809.

Muschenborn, W. and Sonne, H.M., 1975. Effect of strain path on the forming limits of sheet metal. *Arch. Eisenhuttenwes*., 46(9), pp.597-602.

Nakazima, K., Kikuma, T. and Hasuka, K., 1968. Study on the formability of steel sheets. *YAWATA TECH REP*, SEPT. 1968,--264--, 8517-8530.

Neuhaus, R. and Borsutzki, M., 2013. Plättchen-Biegeversuch nach VDA 238-100. *Materials Testing*, 55(9), pp.654-659.

Neuhäuser, H., Klose, F.B., Hagemann, F., Weidenmüller, J., Dierke, H. and Hähner, P., 2004. On the PLC effect in strain-rate and stress-rate controlled tests–studies by laser scanning extensometry. *Journal of alloys and compounds*, 378(1-2), pp.13-18.

Olsen, T.Y., 1920. Machines for ductility testing. Proc. *Am. Soc. Mater*, 20(1920), pp.398-403.

Omer, K., 2015. Development and Testing of a Hot Stamped Axial Crush Member with Tailored Properties. *UWSpace*. http://hdl.handle.net/10012/9024

Pathak, N., 2018. Characterization and Modeling of Sheared Edge Failure in Advanced High Strength Steel. *UWSpace*. http://hdl.handle.net/10012/13033

Pathak, N., Butcher, C., Worswick, M.J., Bellhouse, E. and Gao, J., 2017. Damage evolution in complex-phase and dual-phase steels during edge stretching. *Materials*, 10(4), p.346.

Stoughton, T.B. and Yoon, J.W., 2011. A new approach for failure criterion for sheet metals. *International Journal of Plasticity*, 27(3), pp.440-459.

Stoughton, T.B. and Yoon, J.W., 2012. Path independent forming limits in strain and stress spaces. *International Journal of Solids and Structures*, 49(25), pp.3616-3625.

Stoughton, T.B. and Zhu, X., 2004. Review of theoretical models of the strain-based FLD and their relevance to the stress-based FLD. *International Journal of Plasticity*, 20(8-9), pp.1463-1486.

Stoughton, T.B., 2000. A general forming limit criterion for sheet metal forming. International *Journal of Mechanical Sciences*, 42(1), pp.1-27.

Tharrett, M.R. and Stoughton, T.B., 2003. Stretch-bend forming limits of 1008 AK steel (No. 2003-01-1157). *SAE Technical Paper*.

VDA 238-100, 2017. Plate bending test for metallic materials

Volk, W. and Hora, P., 2011. New algorithm for a robust user-independent evaluation of beginning instability for the experimental FLC determination. *International journal of material forming*, 4(3), pp.339-346.

Walp, M.S., 2007. Impact Dependent Properties of Advanced and Ultra High Strength Steels (No. 2007-01-0342). *SAE Technical Paper*.

Wang, C., Kinzel, G. and Altan, T., 1993. Mathematical modeling of plane-strain bending of sheet and plate. *Journal of Materials Processing Technology*, 39(3-4), pp.279-304.

Wu, P.D., Jain, M., Savoie, J., MacEwen, S.R., Tuğcu, P. and Neale, K.W., 2003. Evaluation of anisotropic yield functions for aluminum sheets. *International Journal of Plasticity*, 19(1), pp.121-138.

Yoshida, M., Yoshida, F., Konishi, H. and Fukumoto, K., 2005. Fracture limits of sheet metals under stretch bending. *International Journal of Mechanical Sciences*, 47(12), pp.1885-1896.

Zhao, L., Sowerby, R. and Sklad, M.P., 1996. A theoretical and experimental investigation of limit strains in sheet metal forming. *International Journal of Mechanical Sciences*, 38(12), pp.1307-1317.

Zhumagulov, A., Abedini, A., Rahmaann, T., Imbert, J., Butcher, C., Worswick, M., Malcolm, S., Dykeman, J. and Ezzat, H., 2018. High Rate Characterization of Three DP980 Steels. *In EPJ Web of Conferences (Vol. 183, p. 02060)*. EDP Sciences.